

UC Berkeley

Envelope Systems

Title

Calculation of the Solar Load onto Occupants in a Room using Bidirectional Scattering Distribution Functions and a View Factor Approach

Permalink

<https://escholarship.org/uc/item/9j11b4z9>

Author

Jedek, Christoph

Publication Date

2012-01-30

Peer reviewed

*Calculation of the Solar Load onto Occupants in a
Room using Bidirectional Scattering Distribution
Functions and a View Factor Approach*

by

Christoph Jedek, B.Sc.

A thesis submitted to the faculty of the Bochum University of Applied Sciences, developed at the University of California at Berkeley, in partial fulfillment of the requirements for the degree of Master of Science in the Institute of Building Physics, Materials Science and Construction.

Bochum
2011

Approved by:

Prof. Dr. Gerrit Höfker

Dr. Sabine Hoffmann

Abstract

Christoph Jedek: Calculation of the Solar Load onto Occupants in a Room using Bidirectional Scattering Distribution Functions and a View Factor Approach.

(Under the direction of Prof. Dr. Gerrit Höfker and Dr. Sabine Hoffmann)

As environmental simulations in the building industry become more and more important, a precise calculation of the solar load onto occupants within buildings, for an infinite variety of fenestration devices, would represent a valuable tool for understanding and predicting the functionality of buildings.

In this thesis, a new tool is created to calculate the direct and diffuse solar radiant gain onto a detailed model of an occupant, as well as on every simulated surface inboard of the fenestration. The tool takes into account any possible fenestration properties and geometric room conditions. To realize it, a new theory was developed for calculating solar load with bidirectional scattering distribution functions (BSDF) and view factors. The tool uses several pre-existing programs to obtain the necessary input information.

Two simulations for different buildings in the United States of America serve as examples of the practical applicability of the tool. The simulation results demonstrate the effects of external shading devices and glazing properties on the solar load on an occupant, both overall and for the occupant's individual body segments, through different times of day and year.

These results can be used directly for analysis, or can be used as input values for subsequent thermal comfort calculation. Similarly, the detailed distribution of transmitted direct and diffuse radiation onto the surfaces of the room provide input for detailed simulations of indoor environments near windows.

Acknowledgements

Although a scientific work like a master's thesis may appear to be solitary work, it requires a network of support and I'm indebted to many people. I am most especially grateful to my family, without whose support I never would have been able to complete this thesis at the University of California at Berkeley.

I also want to thank Professor Höfker, Dr. Hoffmann, and Professor Arens for making possible the opportunity to do this thesis at the University of California at Berkeley, and their valuable guidance and support throughout my work. Special thanks here to Professor Arens, who was always there for me when I needed an advice or a problem occurred. In addition, I want to thank the members of the Center for Environmental Design Research who were always there when problems or question occurred and were ready to help me and of course Phyllis Brooks Schaefer for her guidance with the American language.

Last but not least I want to give special thanks to my fiancée, Jennifer, who waited for me during the time we were separated and always gave me the strength I needed to focus on this research.

Table of Contents

List of Tables.....	v
List of Figures.....	vi
1. Introduction.....	1
2. Background for the calculation approach.....	2
2.1. Relevance of radiation and view factors for calculating solar load	2
2.2. Determination of the incidence angle of the solar beam as base of solar load calculation.....	10
2.3. Calculation of radiation transmission through glazing and shading devices.....	14
2.4. Bidirectional scattering distribution function (BSDF) and their relevance for complex fenestration systems.....	21
3. Development of an advanced calculation tool for the simulation of solar load onto occupants	25
3.1. Definition of the solar beam on the façade by using the outer hemisphere.....	26
3.2. Definition of the façade properties and the inner hemisphere	31
3.3. Development of the virtual testing room and the human manikin.....	34
3.4. Connecting the manikin to the inner hemisphere.....	41
3.5. Development of the solar load calculation under use of calculated view factors.....	46
3.6. Obtaining the solar load values for the body parts of the Manikin from the simulation results.....	50
3.7. Parameter study with an advanced discretization.....	53
4. Case study of the solar load onto occupants for two buildings with shading devices.....	74
4.1. Case study for the simulation of the Helios building in Berkeley, California	74
4.2. Case study for the simulation of a Hospital in Denver, Colorado	82
5. Conclusion.....	94
References.....	97
Annex	101

List of Tables

Table 1	View factors for several area combinations.....	8
Table 2	Example of the solar load on each of the 16 body segments for a diffusing shade and a given solar radiation.....	52
Table 3	Solar load comparison onto W3 for the rough discretization mesh.....	61
Table 4	Solar load comparison onto W3 for the refined discretization mesh.....	62
Table 5	Hourly direct and diffuse solar radiation for a design day, used for the examination of the Helios shading device.....	77
Table 6	Hourly direct and diffuse solar radiation for a design day, used for the examination of the south-façade of the Hospital in Denver.....	84
Table 7	Hourly direct and diffuse solar radiation for a design day, used for the examination of the west-façade of the Hospital in Denver.....	85
Table A.1	7-point thermal sensation scale.....	103
Table A.2	Overall data of the human body for the passive system....	115

List of Figures

Figure 1	Enclosure geometry for derivation of properties of a blackbody.....	3
Figure 2	Relation between the blackbody intensity and the hemispherical emissive power.....	4
Figure 3	Spectral emission intensity of a blackbody.....	5
Figure 4	Explanation for the view factor F_{12} between the two areas A_1 and A_2 and distance r	6
Figure 5	View factors for partially or completely obstructed surfaces.....	9
Figure 6	Earth's orbit with the corresponding angle of the polar axis.....	12
Figure 7	The varying declination angle over the year.....	13
Figure 8	Venetian blind representation.....	17
Figure 9	Light scattering properties of a material sample.....	22
Figure 10	BSDF hemispheres on both sides of a glazing layer.....	23
Figure 11	Bin determination of a quarter size BSDF by using lower and higher boundaries of theta and phi.....	24
Figure 12	Solar angle description for calculating incidence beam.....	27
Figure 13	Definition of a spherical coordinate system.....	28
Figure 14	Determination of the spherical angle Phi and Theta	29
Figure 15	Window 6.3 International Glazing Database.....	32
Figure 16	Window 6.3 Glazing System Library.....	33

Figure 17	Window 6.3 Shading Layer Library showing the different properties.....	34
Figure 18	Virtual testing room with a rectangular box inside.....	36
Figure 19	Rough discretized virtual manikin with sixteen body parts consisting of 220 triangular polygons.....	37
Figure 20	Difficulty of determining the right orientation for surfaces...	38
Figure 21	The virtual testing room with the chosen discretization used in the spreadsheet calculation program.....	39
Figure 22	The virtual testing room after implementing the 220 polygon manikin.....	39
Figure 23	Bin determination of a quarter size BSDF by using lower and higher boundaries of theta and phi.....	48
Figure 24	Ring determination of the BSDF	48
Figure 25	Solar load on the room walls for diffuse fenestration properties.....	54
Figure 26	Surface structure of the 1 st discretization mesh (dx = 75 cm, dz = 75 cm).....	55
Figure 27	Surface structure of the 2 nd discretization mesh (dx = 75 cm, dz = 37.5 cm).....	56
Figure 28	Centroid arrangement for the 1 st discretization mesh (75 cm × 75 cm).....	57
Figure 29	Centroid arrangement for the 2 nd discretization mesh (100 cm × 50 cm).....	57
Figure 30	Outer BSDF hemisphere with marked simulation Bins on the horizontal axis.....	59

Figure 31	Solar load calculation of the corresponding surface on the opposite wall W3 for the BSDF Bin = 2 ($5^\circ \leq \vartheta \leq 15^\circ$) on a 3 m × 3 m simulation room.....	60
Figure 32	Value comparison for the 1 st (50 cm × 50 cm) and 2 nd (75 cm × 37.5 cm) discretization mesh for a rough discretization at 3.0 m room depth.....	61
Figure 33	Value comparison for the 1 st (20 cm × 20 cm) and 2 nd (30 cm × 15 cm) discretization mesh for a refined discretization at 3.0 m room depth.....	62
Figure 34	Value comparison for three different fenestration discretization, and a 10 cm × 5 cm discretized W3 at a room depth of 1.5 m.....	64
Figure 35	Value comparison for three different fenestration discretization, and a 10 cm × 5 cm discretized W3 at a room depth of 3.0 m.....	64
Figure 36	Value comparison for three different fenestration discretization, and a 10 cm × 5 cm discretized W3 at a room depth of 6.0 m.....	65
Figure 37	Viewfactor theory for the solar radiation emitted by a surface F_1 towards a surface F_2 with a varying distance between.....	66
Figure 38	Values comparison for two different fenestration discretization, and a 10 cm × 5 cm discretized W3 at a room depth of 3.0 m.....	67
Figure 39	Value comparison for two different W3 discretization and a 75 cm × 37.5 cm discretized fenestration façade at a room depth of 3.0 m.....	68
Figure 40	Solar load calculation of the corresponding surface on the left wall W2 for varying spherical angle theta on a 3 m × 3 m simulation room.....	69

Figure 41	Value comparison for two different fenestration discretizations and a 10 cm × 5 cm discretized W2 at a room depth and width of 3.0 m.....	70
Figure 42	Value comparison for the 20 cm × 10 cm fenestration and W2 discretization with included as well as excluded edge subsurfaces at a room depth and width of 3.0 m.....	71
Figure 43	Solar load overlay for Bin 26 ($25^\circ \leq \vartheta \leq 35^\circ$) of the outer hemisphere and a 20 cm × 10 cm discretization for the façade and W2.....	72
Figure 44	Solar load overlay for Bin 118 ($65^\circ \leq \vartheta \leq 75^\circ$) of the outer hemisphere and a 20 cm × 10 cm discretization for the façade and W2.....	73
Figure 45	Location of the Helios building at 2151 Berkeley Way at Shattuck.....	74
Figure 46	Rhinoceros presentation of the virtual testing room for the Helios building examination.....	75
Figure 47	Structure of the façade of the Helios building in Berkeley with division into translucent and transparent (vision) glass areas.....	76
Figure 48	Bin calculation for the Helios building using the developed calculation tool.....	77
Figure 49	Comparison of the solar load onto the Manikin for clear sky conditions, south-façade Helios building, Berkeley.....	79
Figure 50	Comparison of the direct solar load onto the Manikin for clear sky conditions, south-façade Helios building, Berkeley.....	80
Figure 51	Comparison of the diffuse solar load onto the Manikin for clear sky conditions, south-façade Helios building, Berkeley.....	80

Figure 52	Comparison of the diffuse solar load onto the Manikin for cloudy sky conditions, south-façade Helios building, Berkeley.....	81
Figure 53	Rhinoceros presentation of the virtual testing room for the Hospital in Denver.....	83
Figure 54	Strucutre of the façade of the Hospital in Denver with division into opaque and transparent (vision) glass areas.....	83
Figure 55	Determination of the solar load for the shaded area of the window, south-façade at 2:30 PM.....	85
Figure 56	Determination of the solar load for the shaded area of the window, west-façade at 5:30 PM.....	86
Figure 57	Comparison of the solar load onto the Manikin for clear sky conditions, south-façade Hospital, Denver.....	87
Figure 58	Comparison of the solar load onto the Manikin for clear sky conditions, west-façade Hospital, Denver.....	87
Figure 59	Comparison of the direct solar load onto the Manikin for clear sky conditions, south-façade Hospital, Denver.....	89
Figure 60	Comparison of the direct solar load onto the Manikin for clear sky conditions, west-façade Hospital, Denver.....	89
Figure 61	Comparison of the diffuse solar load onto the Manikin for clear sky conditions, south-façade Hospital, Denver.....	90
Figure 62	Comparison of the diffuse solar load onto the Manikin for clear sky conditions, west-façade Hospital, Denver.....	91

Figure 63	Comparison of the diffuse solar load onto the Manikin for cloudy sky conditions, south-façade Hospital, Denver.....	92
Figure 64	Comparison of the diffuse solar load onto the Manikin for cloudy sky conditions, west-façade Hospital, Denver.....	92
Figure A.1	PPD/PMV distribution function.....	106
Figure A.2	Acceptable operative indoor temperatures after the adaptive model	109
Figure A.3	Typical segmentation of the human body used in the Berkeley Comfort Model.....	111
Figure A.4	Blood flow model of the Berkeley Human Thermal Comfort Model.....	113
Figure A.5	Simplified node model of Stolwijk.....	113
Figure A.6	Advanced node model of the Berkeley Comfort Model showing four parallel heat paths.....	114
Figure A.7	Schematic presentation of the subdivided average human body.....	116
Figure A.8	Schematic presentation of the multi-node structure of a body part.....	117

1. Introduction

Innovation and improvement of buildings is a continuous process. During the last century, the building structure received the most attention. Innovation in form, structure, and size was the main focus in design. The development of new building materials as concrete and steel frames provided new opportunities in design of buildings. Since the 1970's, the focus shifted to energy efficiency and the well-being of occupants than on the, still important, building structure. There is a recognized need to design buildings to accomplish a minimal energy consumption related with a maximum of comfort.

In order to accomplish these thematic priorities, the design process of buildings has become more detailed. The simulation of buildings energy performance and indoor temperatures is already applied more frequently (for instance by using EnergyPlus, Daemmwerk, and others), but there is still insufficient analysis of the effects of today's highly transparent facades and the amount of solar load into the building's interior and onto its occupants. Near windows, the energy from short- and long-wave radiation represents one of the main input parameter for the thermal comfort calculation. Accurate predictions of solar load on a human are needed for a more precise comfort calculation.

The main emphasis of this research lies on the development of an advanced tool for a precise calculation of the solar load onto occupants, for any possible fenestration properties and geometric conditions of the building or room. The approach for this calculation is the use of the bidirectional scattering distribution function (BSDF) for window devices, in combination with a view factor calculation for the simulation geometry.

The new tool permits a precise calculation of solar load into a building or onto occupants, and allows the effectiveness of projected shading devices to be examined during the design process. The awareness of the behavior of different façade properties and designs will improve the design process and increase designers' ability to create technically more advanced and effective buildings.

2. Background for the calculation approach

In order to develop such a calculation tool, several different mathematical approaches have to be involved. This chapter describes the mathematical background for a better understanding of the development process. As the main emphasis of this thesis lies on the calculation of the solar load, the possible subsequent implementation into a thermal comfort calculation is not further described here. However, a short explanation of different thermal comfort calculation models can be found in Annex 1.

2.1. Relevance of radiation and view factors for calculating solar load

For the calculation of the solar load towards an occupant in an environment, radiation and view factors are two important parameters. Chapter 2.1 is concerned with an explanation of these both parameters. Besides the view factor thematic, focus lies on the emitting behavior of radiant surfaces, since this becomes important for the developed calculating tool.

The solar radiation has a wide spectrum of wave length. Only a small part of the solar transmittance therein is visible for the human eye, but the whole spectrum from infrared to ultraviolet becomes important for calculating the solar load on surfaces or environments.

Every surface emits radiation when its temperature is above the absolute zero temperature of zero Kelvin or $-273.15\text{ }^{\circ}\text{C}$. Unlike the emittance of a black body, the emittance of a real body however is difficult to determine, because it depends on many different factors. Those are for example the composition of the real body, the surface finish, the wavelength of the radiation, as well as the temperature and the spectral distribution of the radiation incidence on the surface. Hence the radiative behavior of a real material is described relative to the behavior of a blackbody by using averaged as well as unaveraged material properties like emissivity, absorptivity and reflectivity. Usually the radiative properties of a real body is measured rather than calculated.

The blackbody is a perfect emittance source, which is defined, after Siegel and Howell (1972, p. 10), as an ideal body that lets in and absorbs all incoming radiation, while the emissivity is $\epsilon = 1.0$. Hence the blackbody is a perfect absorber and perfect emitter as well. Indeed observation of different absorbers shows, that good absorbers of visible light are black for the human eye. However, the emittance depends not only on the visible spectrum as for an example of a white coated surface. This surface has a good absorption of long wave radiation like infrared, but only a minor one of short wave radiation like the visible light.

A short example describes the perfect emittance properties of a blackbody. If a blackbody at a given temperature is placed in a perfectly isolated enclosure, whose surfaces are blackbodies as well at a different initiation temperature as shown in figure 1, both attain the same equilibrium temperature. Under these conditions, the blackbody has to emit the exact same amount of radiation he absorbs. Otherwise the temperature of the enclosure would either increase or decrease, which has the effect of a heat transfer from cooler to warmer. This, however, would imply a violation of the second law of thermodynamics, which determines, after Fermi (1956, pp. 29ff), that energy never could flow from lower to higher without the input of external work.

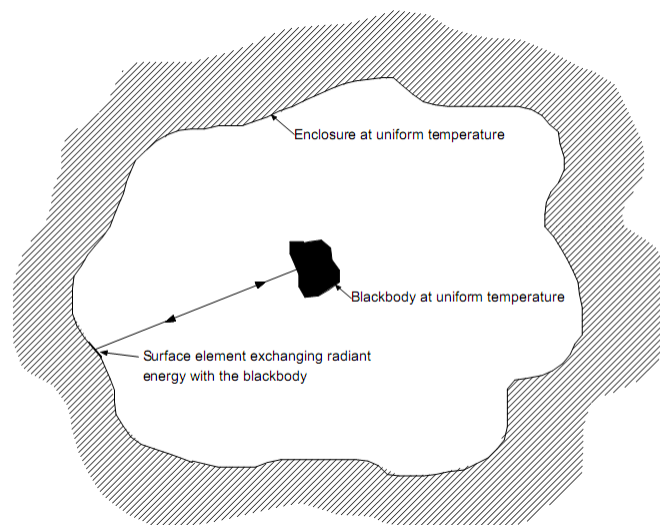


Figure 1: Enclosure geometry for derivation of properties of a blackbody, according to Siegel and Howell (1972, p. 11)

So a blackbody is defined, Siegel and Howell (1972, p. 10), as a 100 percent uniform diffusing emitter and is also named as “*Lambertian radiator*”. Behind this Lambertian radiator is the “*Lambert’s cosine law*” which describes, after Siegel and Howell (1972, p. 17), a quantity for the emitted energy in a given direction per unit of the actual surface area. This quantity is defined as $e'_{\lambda b}(\lambda, \beta, \theta)$ which depends on the wavelength λ , the surface area and the solid angle as shown in figure 2.

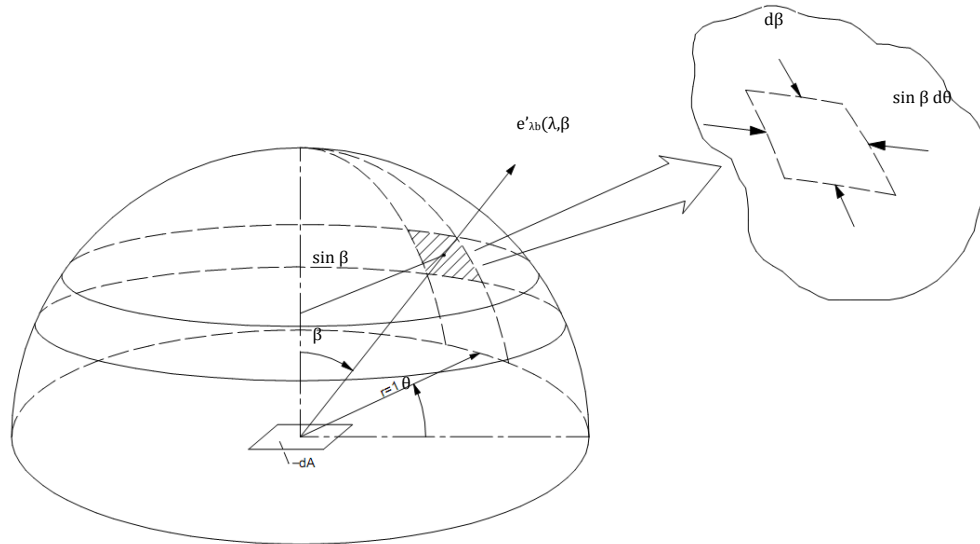


Figure 2: Relation between the blackbody intensity and the hemispherical emissive power, according to Siegel and Howell (1972, p. 17)

Siegel and Howell (1972, p. 17) write that “the energy in the wavelength interval $d\lambda$ centered about λ emitted per unit time in any direction $d^3Q'_{\lambda b}(\lambda, \beta, \theta)$ can then be expressed in the two forms”, which is shown in equation 1.

$$d^3Q'_{\lambda b}(\lambda, \beta, \theta) = e'_{\lambda b}(\lambda, \beta, \theta) dA d\omega d\lambda = i'_{\lambda b}(\lambda) dA \cos(\beta) d\omega d\lambda \quad (1)$$

The index $i'_{\lambda b}(\lambda)$ here stands for the spectral intensity of a blackbody as in figure 3 shown.

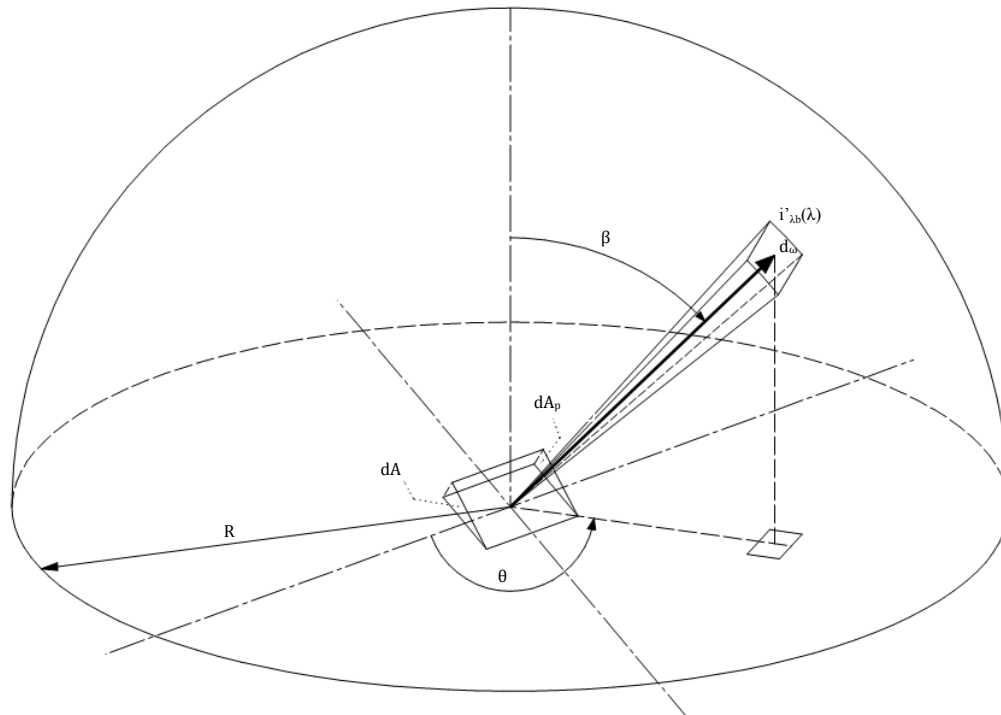


Figure 3: Spectral emission intensity of a blackbody, according to Siegel and Howell (1972, p. 14)

Outgoing from the equation 1, there exist the relation of equation 2, which is known as Lambert's cosine law.

$$e'_{\lambda b}(\lambda, \beta, \theta) = i'_{\lambda b}(\lambda) \cos(\beta) = e_{\lambda b}(\lambda, \beta) \quad (2)$$

The Lambert's cosine law here depends on the wave length. The total emittance for the whole solar spectrum will be obtained by adding up the emittances for different wave lengths.

As every surface with a temperature above the absolute zero point emits radiation, it follows, that adjacent bodies exchange energy in form of heat transfer. According to the second law of thermodynamics, the net energy flow will go from the body with the higher temperature towards the one with a lower temperature.

Determining of this net energy flow is quite complicated, caused by the fact, that not only these both bodies interact with each other, but other bodies in the near have radiant influence too. As there is for every non-black body a reflection part beneath the absorption part, all the other bodies, or surfaces have to be considered. Those bodies are the ones, which generally can see each other.

So for the calculation of the energy flow from one body towards another, it is necessary to know how much both bodies see from each other, independent from the radiation properties of the bodies, like those of a black body or grey body (Lambertian radiator). This non dimensional value determines how many of the emitted radiation of the first body will arrive at the second body. Such a view factor is defined, after Herwig and Moschallski (2006, p. 164), through equation 3 for two surface areas dA_1 and dA_2 . The relation between the two surfaces is graphically described in figure 4.

$$F_{12} = \frac{1}{\pi \cdot A_1} \cdot \int_{A_1} \int_{A_2} \frac{\cos\vartheta_1 \cdot \cos\vartheta_2}{r^2} dA_2 dA_1 \quad (3)$$

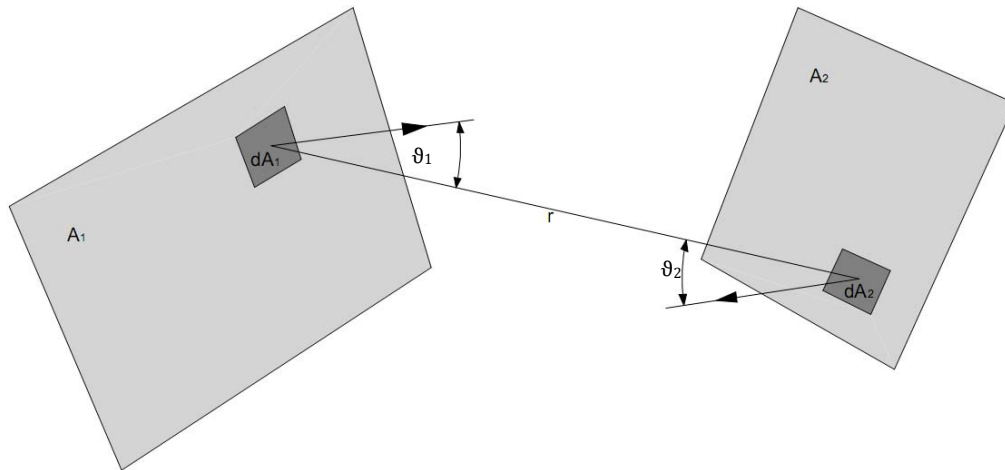


Figure 4: Explanation for the view factor F_{12} between the two areas A_1 and A_2 and distance r , according to Herwig and Moschallski (2006, p. 165)

This non-dimensional coherence between surfaces has after Herwig and Moschallski (2006, p. 165) several relationships concerning the view factors. The change of the indices i and j therein means that the emitting and absorbing surfaces change. So the first relationship is the reciprocity requirement as shown in equation 4.

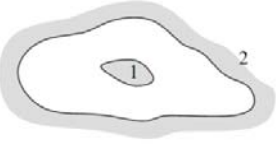

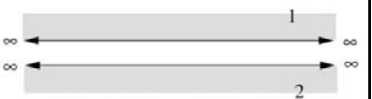
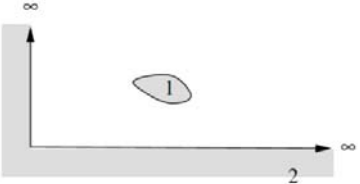

$$A_1 \cdot F_{12} = A_2 \cdot F_{21} \quad (4)$$

The second is, after Herwig and Moschallski (2006, p. 165), the summation rule, which is shown in equation 5, and describes the fact, that the sum of all surfaces, a body sees must be 100%.

$$\sum_{j=1}^n F_{ij} = 1 \quad , i = 1,2,3, \dots, n \quad (5)$$

Furthermore, the view factor for one flat and convex surface to its self is zero, but > 0 for concave surfaces. These coherences are graphically described in table 1.

Table 1: View factors for several area combinations, according to Herwig and Moschallski (2006, p. 166)

Surface arrangement	View factor F_{12}	View factor F_{21}
	1	A_1/A_2
	0.5	0
	1	1
	0.75	0.5
	$F_{11} = 1$	

Even if the mathematical background is already known, the calculation of view factors can be very time intensive. The main problem therein is less the complexity of the calculation equations, as that the calculation time increases exponential with the number of involved surfaces.

This becomes clearer in the example of a room with N surfaces. As long as every surface interacts with the other, N^2 interactions, or view factors, exist. The fact, that a flat surface cannot view itself reduces this amount of view factors to $N(N-1)/2$, which is still a function of the order N^2 . Furthermore, if there is an assumption, that some surface may shade other, the amount of view factors is reduced again. Therefore it is necessary to check $N-2$ surfaces as possible obstructing surfaces, what result in $N(N-1)(N-2)/2$ request for shading objects, what now is a function of the order N^3 . So this short example shows that the calculation effort of view factors rises rapidly, if obstructed surfaces exist in the room.

As described above, in general the calculation of view factors will be distinguished into calculation of unobstructed and obstructed view factors. For unobstructed view factors the above described method can be used, but for obstructed view factors a different method has to be used.

When a third surface will be added to the previous condition, as figure 5 shows, it may block the view between the other both surfaces partially or completely. Under these conditions, the above equation for the view factor calculation is not further applicable.

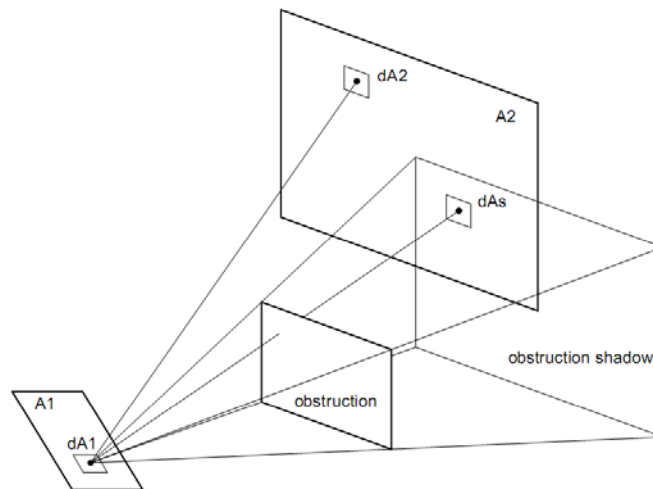


Figure 5: View factors for partially or completely obstructed surfaces, according to Walton (2002, p. 8)

For this situation, after Walton (2002, p. 8), an additional factor has to be implemented into the equation, which is defined as b_{ij} . This factor is zero, if the third surface blocks the radiation connection between surface area A_i and A_j , and its one if the radiation connection is not blocked. So this value gives a percentage effect of the obstructing surface on the radiation exchange between the other two surfaces.

2.2. Determination of the incidence angle of the solar beam as base of solar load calculation

As the solar radiation stands for the main influence factor corresponding to the solar load, besides long wave radiation from surrounding surfaces, this part has to be handled precisely to get correct simulation results. So determining the sun's position at an appropriate time, including the corresponding incidence angle of the solar radiation beam, as well as the determination of the transmission coefficients of the shading device and the glazing device, are necessary input parameters for calculating the solar load. The following chapter will describe more precisely, what values for a given, or chosen simulation situation have to be known, and how they be used to determine the necessary information about the solar radiation.

The determination of the solar beam requires several input parameters like the longitude and latitude, which define a unique location on the earth. Furthermore the time in hours and minutes has to be known, to determine the position of the sun and therefore the solar beam.

The latitude ϕ thus stands, after Duffie and Beckman (1991, p. 13), for the angular location north or south of the equator. So ϕ varies between -90 degree and +90 degree, where the north is determined positive and the south negative. Thus, the south-pole has a latitude of -90 degree, also written as 90°S, and the north pole +90 degree, also written as 90°N, while the equator itself has a latitude of zero degrees.

While the latitude defines the north-south orientation of a location, the longitude λ defines its east-west orientation. The longitudes, which are also known as meridians, are halves of great ellipses, which all have the same radii at any given latitude. The main meridian is called the Prime Meridian, which goes through the Royal Observatory in Greenwich, England and, represents the zero degrees longitude.

Moving out from the Prime Meridian, the longitude defines the deviation eastwards or westwards. So λ varies between -180 degree and +180 degree, where the east is determined positive and the west negative. As a day has 24 hours, and the longitude represents a full circle of 360 degree, it follows that

the sun apparently moves at 15 degree per hour over the day, which makes it possible to determine the longitude on any location on the earth.

For example the west coast of the United States of America is about nine hours behind Coordinated Universal Time (UTC), which is the time on the Prime Meridian. In accordance with the coherences explained above, using the equation $\theta = 15 \cdot (-9)$, the west coast lies on the meridian -135° , also written as 135°W . For a more precise determination of a location, every degree of longitude is subdivided into sixty minutes, and every minute into sixty seconds, but given its minor influence on the incidence angle, this last subdivision is not used here.

The other input parameters are the month, day, hour and minute of the wished simulation, which represents the exact position of the sun at that moment. Also the surface azimuth angle γ has to be determined, which represents, after Duffie and Beckman (1991, p. 13), the deviation of the surface normal from the local meridian. So γ varies between -180 degree and $+180$ degree, where the west is determined positive, the east negative and the south is set to zero. The surface azimuth has to be set into relation to the calculated azimuth, to get the appropriate azimuth angle onto the façade. Once this has been done, the incidence angles theta and phi can be calculated.

To get the solar angles altitude and azimuth, there are several values to calculate before. First of all is the declination angle. After Duffie and Beckman (1991, p. 13), the declination describes the angle of the suns position at solar noon. Depending on the corresponding time of the year, the declination angle varies between -23.45 degree and $+23.45$ degree. This causes through the tilt of the rotation axis of the earth, which lies by 23.45° . This tilt of the earth rotation axis is fixed, while orbiting the sun, what is the cause for seasons and the varying declination angle, as shown in Figure 6.

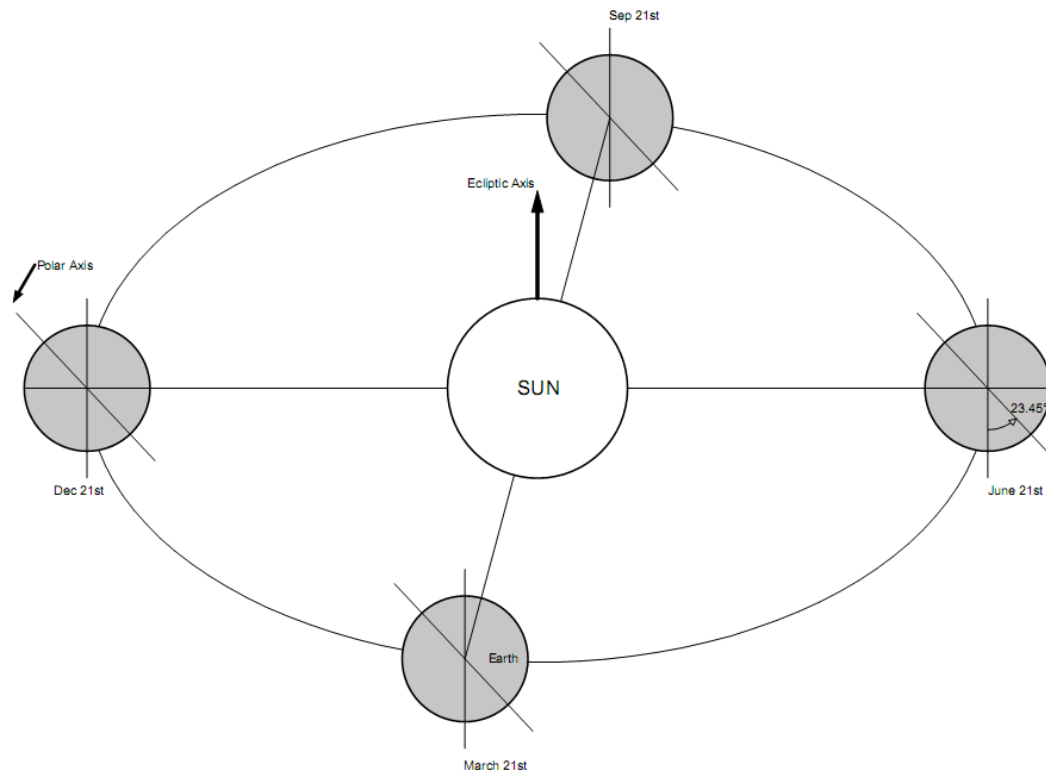


Figure 6: Earth's orbit with the corresponding angle of the polar axis, according to Newton (2007, p. 7)

After Duffie and Beckman (1991, p. 13), the declination angle can be calculated, using the equation from Cooper (1969), which can be found under equation 6 on this page.

$$\delta = 23.45 \cdot \sin(360 \cdot 284 + n/365) \quad (6)$$

Where n represents the day number of the year starting with the first of January as $n = 1$. So calculating the declination angle over a whole year shows the variation of the declination as a function of date, which is shown in Figure 7.

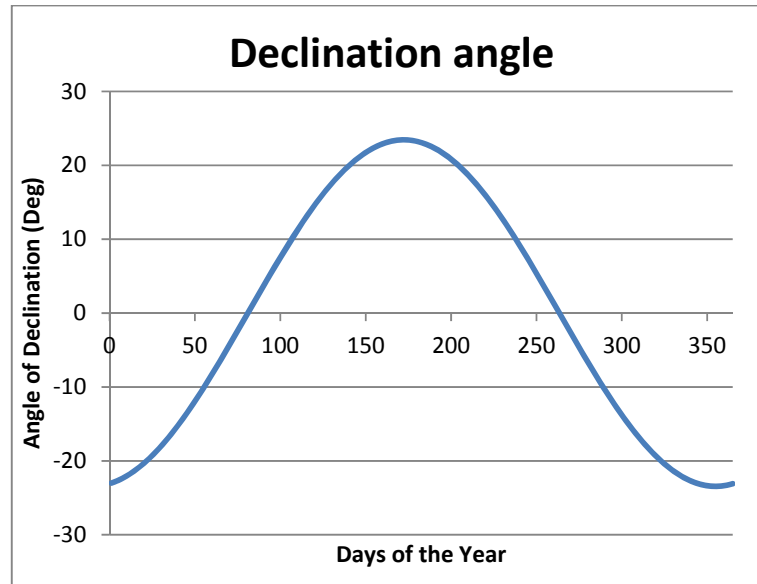


Figure 7: The varying declination angle over the year, according to Newton (2007, p. 8)

Before the calculation of the solar altitude and azimuth can be made, one more value has to be calculated. This last value is the hour angle. After Duffie and Beckman (1991, p. 13), the hour angle is described as the angular deviation of the sun to the east or west of the local meridian due to the earth's rotation, which is, as described before, about 15 degrees per hour. The hour angle is given in degrees and will be calculated in accordance with equation 7.

$$\omega = h + \text{min}/60 - (15 - \Delta\text{long})/15 - 12 + t_{\text{eq}}/60 \quad (7)$$

The index h in this equation stands for the hours of the real time, min stands for the minutes of the real time, Δlong for the difference of the local standard meridian and the longitude of the location and t_{eq} for the time equation in minutes.

With these values the calculation of the solar altitude and azimuth angle now can be made. After Newton (2007, p. 11), the solar altitude is defined as shown in equation 8.

$$\sin \alpha = \sin(\text{lat}) \cdot \sin(\delta) + \cos(\text{lat}) \cdot \cos(\delta) \cdot \cos(\omega) \quad (8)$$

Once the solar altitude is known, the solar azimuth can be calculated by using equation 9.

$$\sin \gamma = \cos(\delta) \cdot (\sin(\omega) / \cos(\alpha)) \quad (9)$$

These both values are used in chapter 3.1, to determine how the individual solar beam incidences on the façade, or on the outer hemisphere.

2.3. Calculation of radiation transmission through glazing and shading devices

Usually the solar transmittance will be calculated for the transmission properties of the glazing device without taking into account the effects of a shading device. Normative methods for these calculations are given for example through the ISO 9050 or DIN EN 410.

The DIN EN 410 for example, similar to the ISO 9050, provides methods for determining light and radiant properties of windows, to get basic information for calculating light, heating, or cooling in buildings. These calculation methods also provide an opportunity to compare different types of windows and their effects on light and energy consumption as well as thermal comfort. However, for calculating the transmission properties for such a glazing device, the DIN EN 410 assumes some simplifications. So, after DIN EN 410 (1998, p. 4), it will be assumed that the window is positioned either horizontally or in the perpendicular and that the incident solar beam is almost perpendicular to the window surface.

The radiation distribution of the incoming solar beam furthermore is defined as the norm light classification D_{65} . This specific norm light classification is defined, after ISO 11664-2 (2011, p. 8), as a spectral power distribution (SPD), tabulated in 5 nm increments from 300nm to 830nm. The index 65 stands for the temperature at which a blackbody radiates at the same color temperature as daylight, in this case 6504 Kelvin. So the norm light classification D_{65} is defined as the normal day light illuminant.

The two properties – light transmission degree τ_v , and energy emittance g – provide the main information about the light transmission and the thermal energy emissivity of the individual window. As the solar transmittance through the glazing for the purpose of this calculating tool is the more important, the g -value will not be further explained here.

After DIN EN 410 (1998, p. 4), the light transmission degree will be calculated using equation 10 for the solar wavelengths from 380nm to 780nm.

$$\tau_v = \frac{\sum_{\lambda=380\text{nm}}^{780\text{nm}} D_{\lambda} \cdot \tau(\lambda) \cdot V(\lambda) \cdot \Delta\lambda}{\sum_{\lambda=380\text{nm}}^{780\text{nm}} D_{\lambda} \cdot V(\lambda) \cdot \Delta\lambda} \quad (10)$$

The index D_{λ} in this equation stand for the spectral distribution of the norm light D_{65} , while $\tau(\lambda)$ describes the spectral luminous efficiency for photopic vision defining the standard observer for photometry and $V(\lambda)$ the spectral sensitive degree for daylight seeing by a normal observer. The index $\Delta\lambda$ stands for the wavelength interval. The term $D_{\lambda} \cdot V(\lambda) \cdot \Delta\lambda$ is to be found in the ISO 9050.

For calculating of windows with more than one glazing layer, the DIN EN 410 provides calculation methods to determine the transmission coefficient for those. In general, the DIN distinguishes here between double and triple glazing devices, but windows with more layers have to be substituted into the both described above. For example, a window with five glazing layer would be calculated as following. The first three layers will be calculated, after DIN EN 410 (1998, p. 4), through equation 12 and both the following layers through equation 11. The calculation results would then be treated as a window with only two layers and calculated appropriate.

$$\tau(\lambda) = \frac{(\tau_1(\lambda) \cdot \tau_2(\lambda))}{(1 - \rho'_1(\tau_1(\lambda) \cdot \rho_2(\lambda)))} \quad (11)$$

$$\tau(\lambda) = \frac{(\tau_1(\lambda) \cdot \tau_2(\lambda) \cdot \tau_3(\lambda))}{((1 - \rho'_1(\lambda) \cdot \rho_2(\lambda)) \cdot (1 - \rho'_2(\lambda) \cdot \rho_3(\lambda)) - (\tau_2^2(\lambda) \cdot \rho'_1(\lambda) \cdot \rho_3(\lambda)))} \quad (12)$$

The index $\tau_i(\lambda)$ thus stands for the spectral transmission coefficient for the i -th glazing layer and $\rho'_i(\lambda)$ describes the spectral reflection coefficient of the i -th glazing layer, measured against the direction of the incoming radiation. The index $\rho_i(\lambda)$ describes the spectral reflection coefficient of the i -th glazing layer, measured into the direction of the incoming radiation.

So the solar transmittance of a window with a changing number of glazing layers can be obtained by using the equations given by the ISO 9050 or the DIN EN 410, respectively. However, these equations do not take into account the effects of a light scattering shading device, like a venetian blind or a frit. The possible calculation methods for windows with such a shading device are described hereafter.

Most calculation algorithms provide only the solar transmittance of the glazing device without taking into account the effects of a shading device, as in the ISO 9050 or DIN EN 410. Calculation algorithms do exist, however, that include glazing and shading devices in the calculation of solar transmittance, like the DIN EN 13363-2 or ISO 15099.

For example, DIN EN 13363-2 (2005) splits the whole calculation into two parts. It calculates the solar transmittance of the glazing device in accordance with the algorithm of DIN EN 410, and the transmittance of the shading device after annex A of the DIN EN 13363-2 (2005), where the shading device is serving as the first layer of the fenestration.

The transmittance of the shading device in DIN EN 13363-2 (2005, pp. 17ff) is divided into the two parts direct and diffuse transmittance. The direct transmittance, after DIN EN 13363-2 (2005, p. 18), will be calculated by using equation 12, while the diffuse transmittance will be calculated using equation 13. These equations are valid just for shading devices like venetian blinds, and they can't be used for calculation of frits, woven shades or similar.

$$\tau_{S,D} = \phi_{51} \cdot \rho + \phi_{61} \cdot \tau + \frac{(Z \cdot \phi_{54} \cdot \rho' + \phi_{63} \cdot \tau) \cdot (\phi_{31} \cdot \rho + \phi_{41} \cdot \tau) + (Z \cdot \phi_{63} \cdot \rho' + \phi_{54} \cdot \tau) \cdot (\phi_{41} \cdot \rho + \phi_{31} \cdot \tau)}{\phi_{34} \cdot \rho \cdot (1 - Z \cdot Z')} \cdot Z \quad (12)$$

$$\tau_{S,d} = \phi_{21} + \frac{(\phi_{23} \cdot \rho + \phi_{24} \cdot \tau) \cdot (\phi_{31} + Z' \cdot \phi_{41}) + (\phi_{24} \cdot \rho' + \phi_{23} \cdot \tau) \cdot (\phi_{41} + Z \cdot \phi_{31})}{\phi_{34} \cdot \rho \cdot (1 - Z \cdot Z')} \cdot Z \quad (13)$$

The index $\phi_{i,j}$ thus stands for angle factor between zone1 and zone2, as determined in figure 8, while the index τ describes the transmission coefficient of the shading device material. The index ρ delivers the reflection coefficient of the shading device panel surface, which is orientated towards the incidence radiation. The opposing side of the shading device panel is described through the index ρ' , and the index Z is defined as in equation 14 shown, and the index Z' as in equation 15 shown.

$$Z = (\phi_{34} \cdot \rho) / (1 - (\phi_{34} \cdot \tau)) \quad (14)$$

$$Z' = (\phi_{34} \cdot \rho') / (1 - (\phi_{34} \cdot \tau)) \quad (15)$$

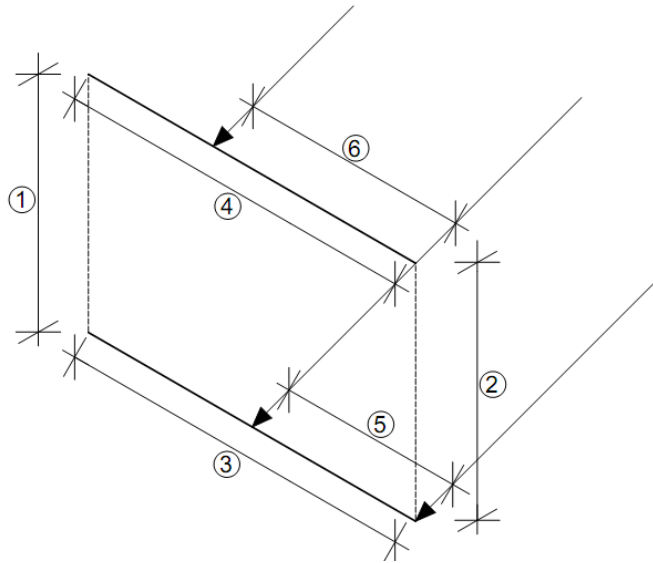


Figure 8: Venetian blind representation, according to DIN EN 13363-2 (2005, p. 17)

The global radiation will be calculated after DIN EN 13363-2 (2005, p. 18) with a combination of the direct and diffuse radiation as shown in equation 16.

$$\tau = \tau_D \cdot 0.85 + \tau_d \cdot 0.15 \quad (16)$$

Window6 uses after Carli (2006, p. 27ff) a bi-directional method for calculating the solar transmittance through shading devices, which was originated by Nicodemus in 1977. This transmittance could be specular and diffuse at the same time for optical layer, as, for example, venetian blind devices. These transmitting properties are defined for each combination of incidence and outgoing radiation, what result in an array of a square matrix with equal number of columns and rows, generally described as BTDF, or BSDF. The number of the columns and rows therein depends on the total number of different angular coordinates (θ, φ) . The bi-directional distribution function is described more precisely in chapter 2.4.

So the forward going incidence radiation as well as the backward going reflectance radiation of an optical layer will be calculated after Carli (2006, p. 28) by using the equation 17 and 18.

$$I(\theta, \varphi) = \tau^f(\theta_j, \varphi_j; \theta_i, \varphi_i) \cdot E(\theta_i, \varphi_i) \quad (17)$$

$$I^r(\theta^r, \varphi^r) = \rho^f(\theta_j^r, \varphi_j^r; \theta_i, \varphi_i) \cdot E(\theta_i, \varphi_i) \quad (18)$$

The index $\tau^f(j, i)$ thus describes the forward going bi-directional transmittance through the optical layer, while $\rho^f(j, i)$ describes the bi-directional reflectance. The radiation comes from direction i and will be transmitted, or reflected into direction j . After the above described structure of the BSDF matrix, the equations 17 and 18 can be calculated as shown in equation 19 and 20.

$$\begin{bmatrix} I_1 \\ I_2 \\ I_3 \\ \dots \\ I_N \end{bmatrix} = \begin{bmatrix} \tau_{1,1}^f & \tau_{1,2}^f & \tau_{1,3}^f & \dots & \tau_{1,N}^f \\ \tau_{2,1}^f & \tau_{2,2}^f & \tau_{2,3}^f & \dots & \tau_{2,N}^f \\ \tau_{1,1}^f & \tau_{1,2}^f & \tau_{1,3}^f & \dots & \tau_{1,N}^f \\ \dots & \dots & \dots & \dots & \dots \\ \tau_{N,1}^f & \tau_{N,2}^f & \tau_{N,3}^f & \dots & \tau_{N,N}^f \end{bmatrix} \cdot \begin{bmatrix} E_1 \\ E_2 \\ E_3 \\ \dots \\ E_N \end{bmatrix} \quad (19)$$

$$\begin{bmatrix} I_1^r \\ I_2^r \\ I_3^r \\ \dots \\ I_N^r \end{bmatrix} = \begin{bmatrix} \rho_{1,1}^f & \rho_{1,2}^f & \rho_{1,3}^f & \dots & \rho_{1,N}^f \\ \rho_{2,1}^f & \rho_{2,2}^f & \rho_{2,3}^f & \dots & \rho_{2,N}^f \\ \rho_{1,1}^f & \rho_{1,2}^f & \rho_{1,3}^f & \dots & \rho_{1,N}^f \\ \dots & \dots & \dots & \dots & \dots \\ \rho_{N,1}^f & \rho_{N,2}^f & \rho_{N,3}^f & \dots & \rho_{N,N}^f \end{bmatrix} \cdot \begin{bmatrix} E_1 \\ E_2 \\ E_3 \\ \dots \\ E_N \end{bmatrix} \quad (20)$$

It is important to know, that the values of the BSDF matrix represent a sum of two different transfer mechanism, which are one for the undisturbed, directly transmission, in the following shortened as *dir*, and the other one for the Lambertian diffuse reflections, in the following shortened as *diff*. So the bi-directional matrix is defined after Carli (2006, p. 29) as shown in equation 21.

$$\text{Tau}_F = \text{Tau}_F\text{-dir} + \text{Tau}_F\text{-diff} \quad (21)$$

The undisturbed or direct transmitted part of the incident radiation travels through the shading device, without any interaction with the slat material. This means, that the direct transmission has to be calculated for each different slat angle by following the Dir-Dir-Method described in chapter 3.6.1 of Carli (2006, p. 15). This value is only dependent on the geometric of the slats. The properties of the slat material have no influence on this value. The calculated direct transmission part has to be divided through the value Lambda Λ , as shown in equation 22, before it will be placed into the BSDF matrix.

$$\tau_{i,dir}^f = \tau_{dir-dir,i}^f / \Lambda_i \quad , i = 1, \dots, N \quad (22)$$

The Lambda values thus describe geometrical quantities, which are associated with the partitioning of solid angle, as described in Carli (2006, p. 29). This means, that the Lambda value integrates the transmission coefficients over the hemisphere. An example for a Lambda calculation is given in chapter 3.5.

The diffuse part of the incidence radiation through the shading device is the part that travels through the shading device and interacts with the slat material, leaving at one of the two slat sides, after a series of Lambertian reflections. Window6 uses two different methods for determining the diffuse part of the incidence radiation, the Uniform-Diffuse Method and the Directional-Diffuse Method.

The Uniform-Diffuse Method calculates the $\tau_{dir-diff,i}^f$ for each incidence angle of the solar radiation, as described more precisely in chapter 3.6.2 of Carli (2006, p. 16). The calculation results are hemispherical values, which are averaged over the whole hemisphere. This is the reason for the necessary division through π , before placing it into the BSDF diffuse matrix. Caused by the averaged values, every different column has the same values.

When the direct and diffuse part the will be summed, the bi-directional matrix $\mathbf{Tau_F}$ is obtained, after Carli (2006, p. 33), as shown in equation 23.

$$\mathbf{Tau_F} = \begin{bmatrix} \frac{\tau_{dir-dir,1}^f}{\Lambda_1} + \frac{\tau_{dir-diff,1}^f}{\pi} & \frac{\tau_{dir-diff,2}^f}{\pi} & \dots & \frac{\tau_{dir-diff,N}^f}{\pi} \\ \frac{\tau_{dir-diff,1}^f}{\pi} & \frac{\tau_{dir-dir,2}^f}{\Lambda_2} + \frac{\tau_{dir-diff,2}^f}{\pi} & \dots & \frac{\tau_{dir-diff,N}^f}{\pi} \\ \frac{\tau_{dir-diff,1}^f}{\pi} & \frac{\tau_{dir-diff,2}^f}{\pi} & \dots & \frac{\tau_{dir-dir,N}^f}{\Lambda_N} + \frac{\tau_{dir-diff,N}^f}{\pi} \end{bmatrix} \quad (23)$$

The Directional-Diffuse Method against the Uniform-Diffuse Method does not give uniform distributions of diffuse radiation. It calculates a diffuse component for each outgoing angle and calculates which segments are visible or non-visible, or obstructed by other slats. This means, after Carli (2006, p. 34f), that this method considers cut-off angle and adjusts the diffuse radiation intensity on this cut-off angle. So this method results in more realistic values for diffuse transmission through shading devices.

2.4. Bidirectional scattering distribution function (BSDF) and their relevance for complex fenestration systems

The use of the bidirectional scattering distribution function (BSDF) provides a tool, for calculating transmittance through different complex fenestration systems called CFS. After Jonsson et al. (2008, p. 3), the first bidirectional distribution function, called BTDF was defined by Nicodemus in 1977.

There are existing three different bidirectional distribution functions. The bidirectional transmission distribution function (BTDF) and the bidirectional reflectance distribution function (BRDF) were both defined by Nicodemus after Jonsson and Branden (2006, p. 3). The third one is named the bidirectional scattering distribution function. The BSDF is used usually for more general description of samples, which have transmitted as well as reflected scattering properties. This BSDF describes a surface's or bulk sample's scattering properties in any incoming and outgoing direction. So the BSDF is able to deliver the solar transmission coefficients for any direction in an environment, corresponding to any possible incidence angle of the solar beam.

After Jonsson and Branden (2006, p. 3), Stover redefined the originally definition of Nicodemus as a non-differential, as shown in equation 24, but the differential form is very similar, as shown in equation 25. Figure 9 visualizes these two equations for a better understanding.

$$BSDF = (P_s/\Omega_s)/P_i \cdot \cos\theta_s \quad (24)$$

Where P_s is the scattered light flux in Watts, and Ω_s is the solid angle into which the scattered light is redirected. P_i stands for the incidence light flux in Watts, and θ_s describes the scattering angle.

$$BSDF = (dP_s/d\Omega_s)/P_i \cdot \cos\theta_s \quad (25)$$

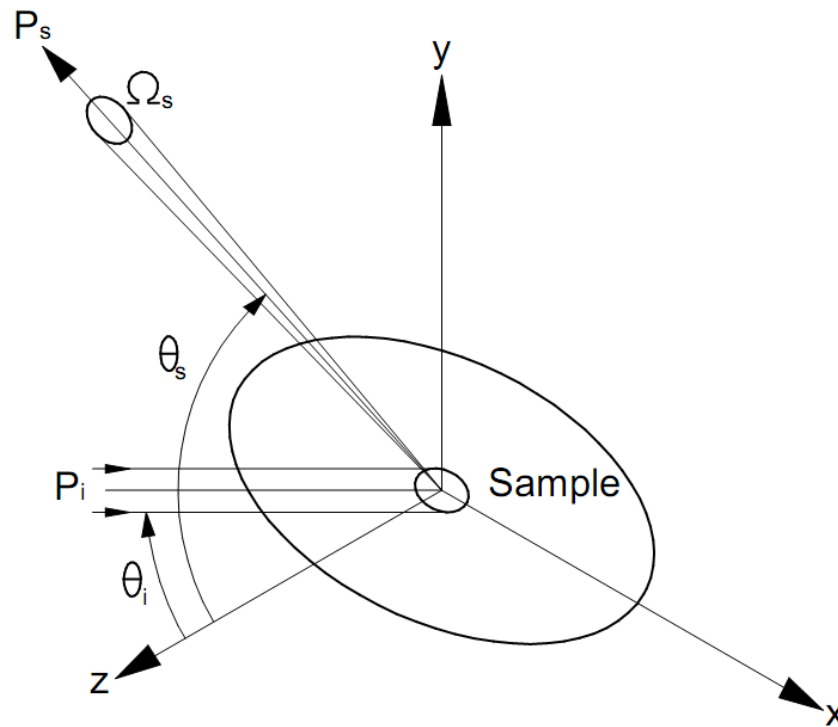


Figure 9: Light scattering properties of a material sample, according to Jonsson and Branden (2006, p. 4)

Figure 9 shows a light beam P_i with an incidence angle θ_i which is scattered from the sample as an outgoing beam P_s at an angle θ_s with an outgoing solid angle Ω_s .

As the bi-directional scattering distribution function describes incidence radiation angles as well as the outgoing radiation angle, the BSDF usually is written as dependent of four different parameters. These are the spherical angle theta (θ) and phi (ϕ). So every single transmission coefficient depends on $(\theta_i; \phi_i)$ for the incidence radiation beam, and $(\theta_s; \phi_s)$ for the outgoing, transmitted radiation beam. In reality, the BSDF values depend also on the wavelength and the polarization state of the incidence radiation beam.

With this definition of the depending parameter, the total transmitted radiation for a given incidence angle can be obtained, after Ward et al. (2011, p. 2f), by multiplying the luminous coefficients by the incidence radiance and summing up these for all patches of the hemisphere as shown in equation 26.

$$\tau(\theta_1; \phi_1) = \int_0^{2\pi} \int_0^{\pi/2} \text{BTDF}(\theta_1; \phi_1; \theta_2; \phi_2) \cdot \cos\theta_2 \cdot \sin\theta_2 \, d\theta_2 d\phi_2 \quad (26)$$

As described before, the BSDF imagines a hemisphere over both sides of the transparently device, as shown in figure 10. To define the solar transmission coefficient for any incoming and outgoing direction, these both hemispheres have to be discretized.

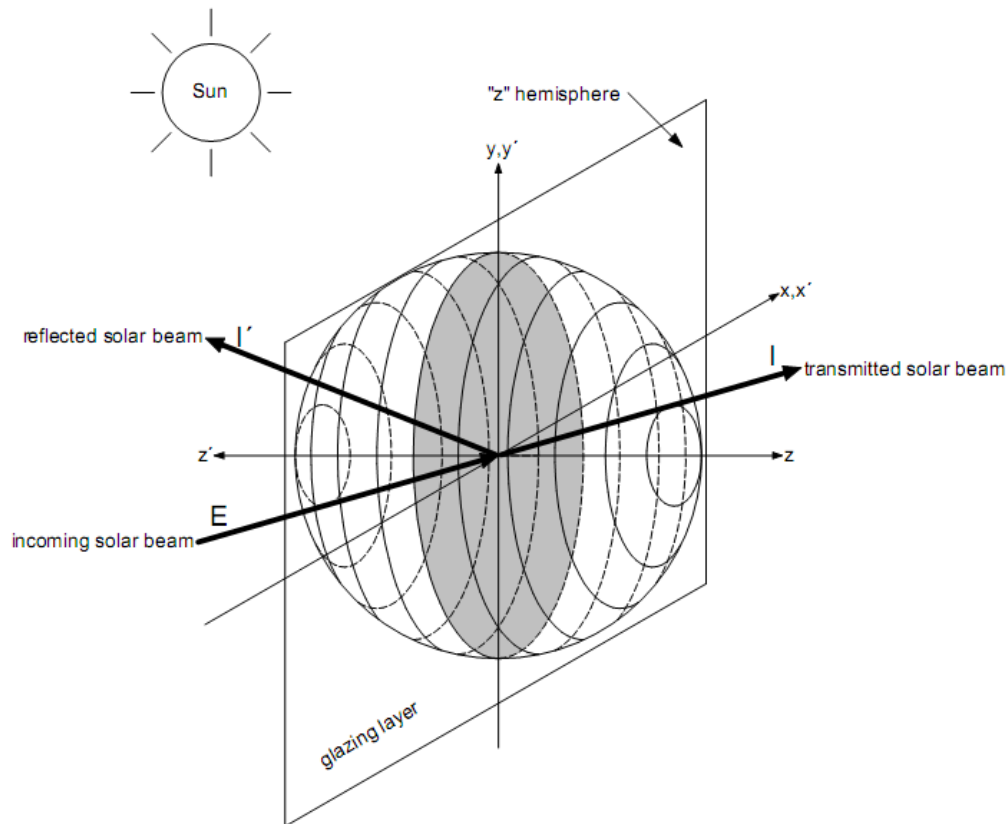


Figure 10: BSDF hemispheres on both sides of a glazing layer, according to Carli (2006, p. 6)

Window6 therefore has, after Mitchell et al. (2008, p. 6-3) three different discretizations of the hemisphere. They are denoted as Full Size or Standard Basis, Half Size and Quarter Size. The virtual hemisphere is thus discretized into a fixed number of different fields, called Bins.

These Bins represent a fixed surface area, bounded through the spherical angle theta and phi. Theta thus defines, through an upper and lower value, in which ring of the hemisphere the Bin lies. The spherical angle phi instead defines where on this ring the corresponding Bin lies exactly. Figure 11 describes these coherences graphically.

So the quarter size hemisphere, after Mitchell et al. (2008, p. 6-12f), has the roughest discretization, with five rings and 41 Bins on each of both hemispheres. The half size hemisphere is discretized more precisely into seven rings and 73 Bins on each hemisphere. So the full size hemisphere is the one, used by Window6, with the highest level of discretization. It has 9 rings with 145 Bins on each hemisphere. Such a discretization of the outer and inner hemisphere with the corresponding Bin numbers for a full size hemisphere is shown in Annex 2 and 3.

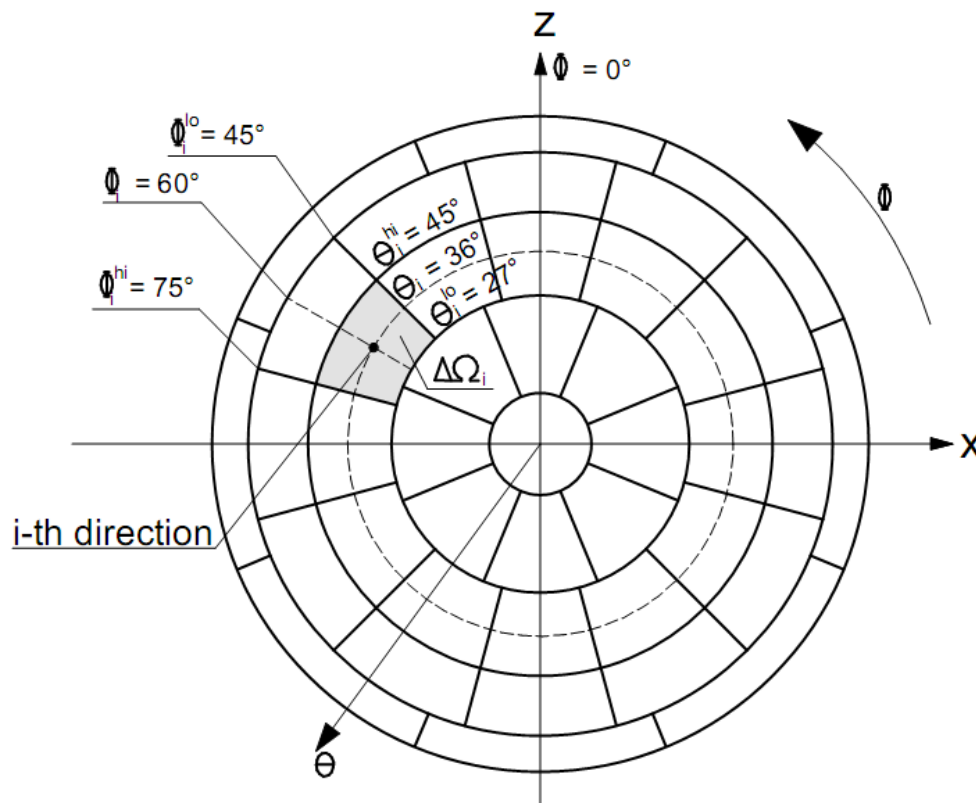


Figure 11: Bin determination of a quarter size BSDF by using lower and higher boundaries of theta and phi, according to Carli (2006, p. 31)

By using this definition, Window6 produces a BSDF matrix with analogue numbers of columns and rows. This could be for example a 145 x 145 matrix for a full size BSDF. The respective number of the column, starting by one, stands for the corresponding Bin on the outer hemisphere, where the incidence radiation beam impinges. So for this special incidence Bin on the outer hemisphere, the respective row, starting by one as well, provides the value for the solar transmission coefficient into the one direction, which radiates through this Bin of the inner hemisphere.

The BSDF file provides several information about the calculate CFS. These are for example the glazing system, glazing system name, the number of layers and optional comments. Also, it provides the values for the transmission coefficients for solar transmission and reflection, forward and backward as well. These are defined, after Mitchell et al. (2008, p. 6-6), as SolarTf, SolarTb, SolarRf and SolarRb.

3. Development of an advanced calculation tool for the simulation of solar load onto occupants

The main topic of this thesis is to find a way, to take into account the diffusing properties of fenestrations and different shading systems during the solar load calculation. To automatize these diffusing effects beneath the solar load through direct solar radiation, a calculation tool has to be developed. This tool should calculate the combination of direct and diffuse solar load on the environment and occupants, corresponding to the individual fenestration and shading device. This means the implementation of different input data, delivered by several external programs, as well as using the equations described during the following chapter.

Furthermore the necessary results of the calculation have to be converted into an output file, which can be used in possible following step as an input file of a thermal calculation tool, as for example the Berkeley Human Thermal Comfort Model, developed at the University of California at Berkeley. This combination of different programs with the new developed calculation tool, will allow a more precisely representation of real solar load onto an environment, or onto occupants. The following chapters describe what

parameters are used, what input data are delivered by external software and what equations are used to calculate diffuse radiation as well as direct radiation.

3.1. Definition of the solar beam on the façade by using the outer hemisphere

To obtain the values of the solar load on the manikin and the environment, it is necessary to precisely define several boundary conditions. While some of these boundary conditions, like solar transmission coefficients or view factors, are provided by external programs like Window6 or View3D, others have to be defined manually, depending on the given or chosen conditions of the simulation. Some of these manual boundary conditions become significant for calculation of the amount and the orientation of the incoming solar radiation beam on the fenestration facade.

As in chapter 2.4 more precisely described, this calculation tool uses the Bidirectional Scattering Distribution Function, to take into account the diffusing properties of shading devices like venetian blinds, frits, diffusing shades or several others. This means that a hemisphere exists on both sides of the fenestration facade with a given amount of Bins from 41 to 145, depending on the discretization, chosen in Window6. For example the quarter size matrix, which stands for a rough discretization with only 41 Bins on each hemisphere, or the full size matrix, which stands for a more precise discretization with 145 Bins on each hemisphere.

For a precise calculation of the solar load onto the manikin and the environment, the exact angle of incidence and the amount of the solar radiation have to be described. The value for the amount of the solar radiation has to be chosen for the requested kind of weather, which shall be simulated.

The angle of incidence, however, requires the exact information of the solar azimuth and altitude, which will be calculated after Duffie and Beckman (1991, p. 11ff). The solar altitude α_s thus describes the angle between the horizontal and the solar beam on a surface. Therefore the solar altitude also is known as the solar elevation angle. The solar azimuth γ_s , thus describes

the angular deviation of the radiation beam, projected on the horizontal plane, from the south. This is shown in Figure 12. After Duffie and Beckman (1991, p. 13), the deviation to the east is determined as negative, while the deviation to the west is determined as positive.

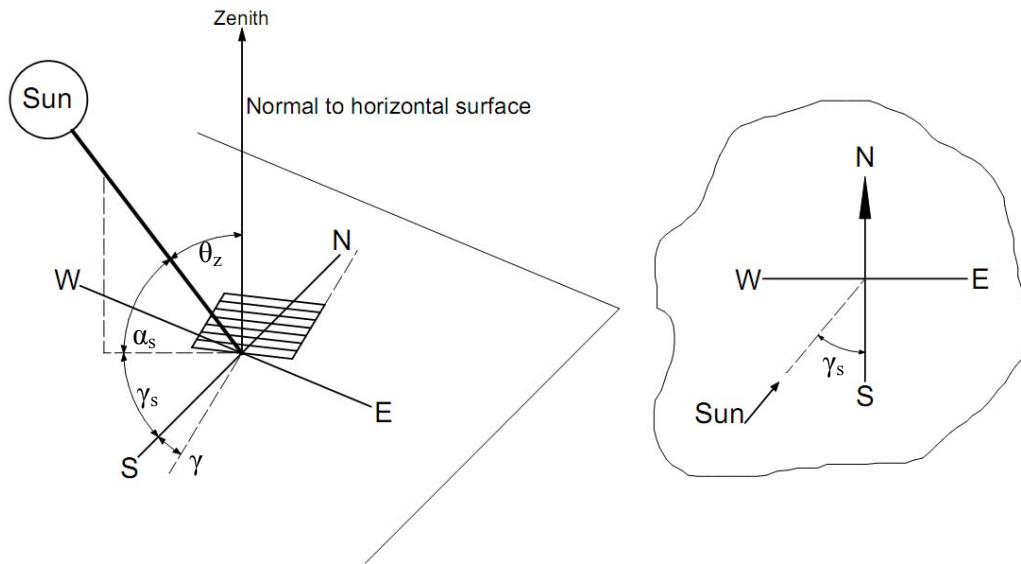


Figure 12: Solar angle description for calculating incidence beam, according to Duffie and Beckman (1991, p. 14)

To calculate the solar angles, it is necessary to determine some input parameter. Two of these input parameters are the longitude and latitude angle, which describe a unique point on the earth that represents the location of the simulated building, as is described more precisely in chapter 2.2.

With these two solar angles, it is possible to calculate the spherical angles phi and theta, which are necessary to determine which Bin of the outer hemisphere corresponds to the given solar radiation beam. To obtain the azimuth angle on a given façade, the calculated solar azimuth angle, which is orientated to the north, has to be modified. Therefore the surface azimuth of the given façade will be subtracted from the calculated solar azimuth. The resulting azimuth angle is orientated onto the given façade. With this new orientated azimuth, the horizontal and vertical deviation angle between the incident solar beam and the surface normal, which corresponds to the spherical angle phi and theta, can be calculated.

A coordinate system is applied to the façade with the façade being the x- / y-plane and the normal vector being the z- coordinate. The positive y-coordinate is pointing to the top of the building and the positive x-coordinate is pointing toward the right side while standing in front of the façade.

So the horizontal deviation angle alpha, which stands for the solar azimuth angle, would be between -90 deg (parallel incidence from the right $< \alpha < 90$ deg (parallel incidence from the left). This means, that the value for the façade orientated azimuth angle has to be between -90 and +90 degree for solar incidence. Otherwise the façade lies in shadow. The calculation tool delivers an individual surface orientation as well as the four main orientations north, east, south and west.

The vertical deviation angle corresponds to the altitude for a vertical façade with $0 \text{ deg} < \beta < 90 \text{ deg}$. For a tilted façade the lower part of the hemisphere comes into play with $-90 \text{ deg} < \beta < 90 \text{ deg}$.

The outer hemisphere lies on the fenestration façade, which corresponds to the X and Z layer, and expands towards the negative Y axis. The structures of such spherical coordinates is shown in Figure 13, remembering that the here shown graphic is a hemisphere lying on the X and Y layer, expanding towards the positive Z axis.

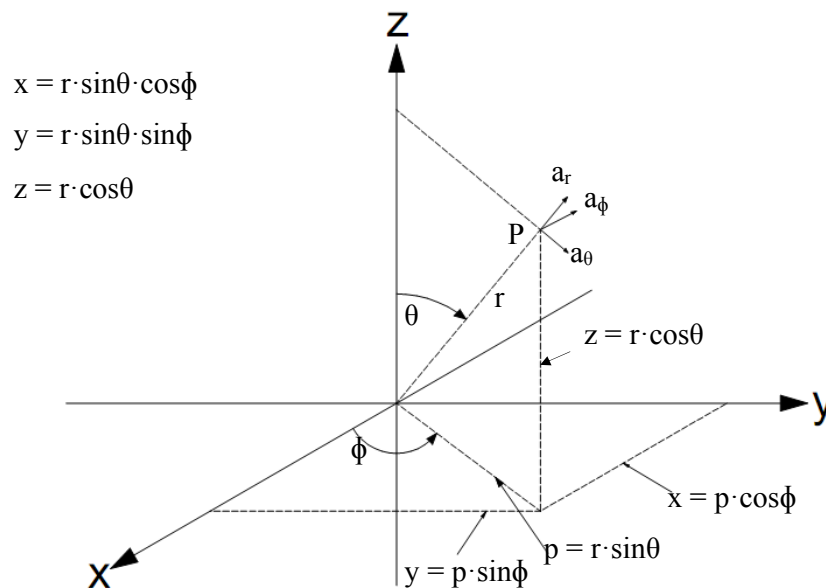


Figure 13: Definition of a spherical coordinate system

The given coordinate system for the two spherical angles are graphical described as shown in Figure 14.

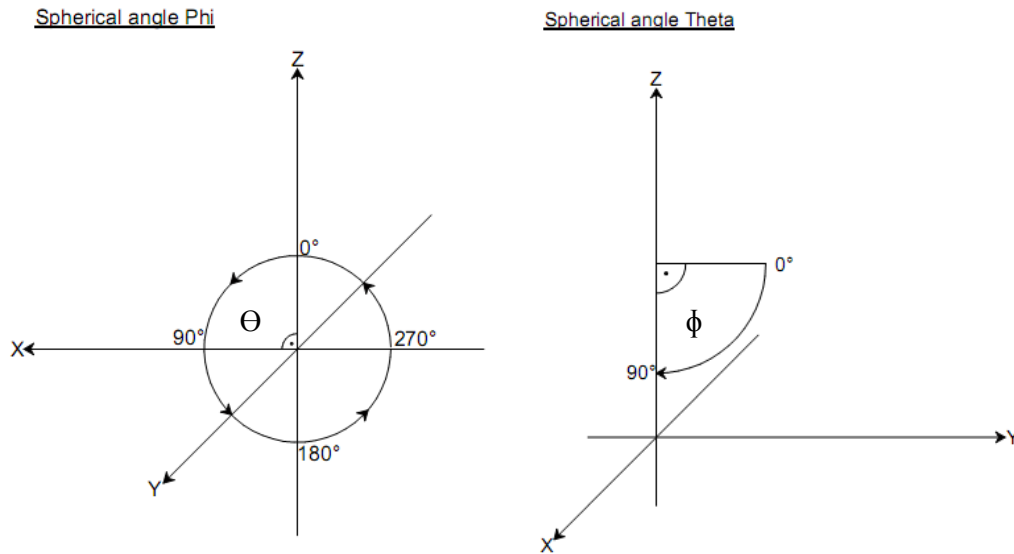


Figure 14: Determination of the spherical angle Phi and Theta

Under these conditions, the incidence vector of the solar beam on the façade can be calculated using equation 27 and the normalized incidence vector using equation 28.

$$\vec{v} = \begin{pmatrix} x \\ y \\ z \end{pmatrix} = \begin{pmatrix} \sin(\alpha) \\ \cos(\alpha) \\ \sin(-\beta) \end{pmatrix} \quad (27)$$

$$\vec{v}_n = \frac{\begin{pmatrix} x \\ y \\ z \end{pmatrix}}{\sqrt{x^2+y^2+z^2}} \quad (28)$$

With this Cartesian coordinate system and the obtained incidence vector of the solar beam, the equations for calculating the spherical angles could be solved. The calculation for the azimuth angle will be used using equation 29 as shown below.

$$\varphi = \left\{ \begin{array}{l} \arctan\left(\frac{x}{z}\right) + \pi, \text{ if } z < 0 \cap x \geq 0 \\ \arctan\left(\frac{x}{z}\right) - \pi, \text{ if } z < 0 \cap x < 0 \\ \arctan\left(\frac{x}{z}\right), \text{ if } z > 0 \\ \operatorname{sgn}(x)\left(\frac{\pi}{2}\right), \text{ if } z = 0 \end{array} \right\} \quad (29)$$

Here it is obviously, that the kind of transformation equation depends on the values from the x and z component. This distinction of the four equations is thus very important for getting the correct range of angles from $-\pi$ to $+\pi$ in rad, respectively -180° to $+180^\circ$ in degree. Otherwise there will be quickly occurring mistakes.

For example by only using the third determination without taking into account the requirements, which may be often found in reference literature, the results of the angles range from $-\pi/2$ to $+\pi/2$, respectively -90° to $+90^\circ$. This is because of the definition of the arctan, also often written as \tan^{-1} , which ranges only between these two angles. So to get the full 360° circle, the four determinations were necessary.

The equation 30 for the polar angle on the other hand is less complex:

$$\theta = \arctan\left(\frac{\sqrt{z^2+x^2}}{y}\right) \quad (30)$$

With the two obtained spherical angles Theta and Phi, an assignment for incidence solar radiation beam to its corresponding Bin on the outer hemisphere can be made.

This assignment requires several requests of the both spherical angles theta and phi. The first request figures out what ring of the outer hemisphere matches to the corresponding spherical angle Theta. As shown in the calculation spreadsheet of Annex 4, every ring has its own range of angle Theta. The hemisphere thus consists of nine rings, first beginning at zero degree and last ending at 90 degree.

After determining what ring corresponds to the angle Theta, the second request figures out what Bin on this ring matches to the corresponding spherical angle Phi. Annex 4 also shows the range of angle Phi for every Bin on each ring of the outer hemisphere.

For example, is the spherical angle Theta of the corresponding distance vector between 15 and 25 degree, the result of the first request is, that the Bin lies in the third ring of the inner hemisphere. Further, is the spherical angle Phi between 33.75 and 56.25 degree, the second request gives the result, that the corresponding Bin is the number 20 on the outer hemisphere. The discretization of the outer hemisphere is shown in Annex 5.

This determination of the corresponding Bin on the outer hemisphere provides the information which column of the BSDF matrix belongs to the given solar incidence angle.

3.2. Definition of the façade properties and the inner hemisphere

As the corresponding Bin on the outer hemisphere for the given incidence angle of the solar radiation beam is known, it is necessary to figure out how the radiation beam transmits through the shading device and the fenestration, as well as where, and with what amount it is transmit into the environment. Most calculation algorithms, however, provide only the solar transmittance of the glazing without taking into account the effects of a shading device, as in the ISO 9050. Some calculation algorithms do exist, however, that take into account glazing and shading devices for the calculation of the solar transmittance, like the DIN EN 13363-2 or ISO 15099. These calculation algorithms reduce the difficulty of a 3-dimensional transmittance to a one-dimensional one.

The use of the BSDF allows calculating the solar transmittance for several types of fenestration with or without a shading device, and with a free eligible number of glazing layer. Furthermore the BSDF provides transmission coefficients for any incidence angle into any outgoing direction. To calculate a BSDF for a specific fenestration, the glazing device and the shading device as well have to be determined under Window6.

To define the properties of the glazing device, Window6 uses a virtual glass library. This glass library contains different glass layers, which have been approved by the National Fenestration Rating Council (NFRC). The NFRC is an independent organization, which administers the rating and labeling for the energy performance of windows. To implement new glass technology, the NFRC update this glass library, called “International Glazing Database” (IGDB) in regular intervals. The data in the IGDB, after Mitchell et al. (2011, p. 5.2ff), is thus determined according to the NFRC 300 (2002) procedure. So the IGDB provides a continuously growing amount of different glass layer with several necessary properties, as shown in figure 15.

ID	Name	ProductName	Manufacturer	Source	Mode	Color	Thickness	Tsol
100	BRONZE_3.DAT	Generic Bronze Glass	Generic	IGDB v11.4	#	#	3.124	0.646
101	BRONZE_6.DAT	Generic Bronze Glass	Generic	IGDB v11.4	#	#	5.740	0.486
102	CLEAR_3.DAT	Generic Clear Glass	Generic	IGDB v11.4	#	#	3.048	0.834
103	CLEAR_6.DAT	Generic Clear Glass	Generic	IGDB v11.4	#	#	5.715	0.771
104	GRAY_3.DAT	Generic Grey Glass	Generic	IGDB v11.4	#	#	3.124	0.609
200	Ag25LE.bsf	Solar Gard® Silver Ag 25 Low-E on 3mm W/W	Bekaert Specialty Films, LLC	IGDB v12.6			3.023	0.156
201	Aut_br30.bsf	Panorama® Autumn Bronze 30 on 3mm W/W	Bekaert Specialty Films, LLC	IGDB v12.6			3.023	0.244
202	Gold55.bsf	Solar Gard® Gold 55 on 3mm W/W	Bekaert Specialty Films, LLC	IGDB v12.6			3.023	0.301
203	Gold65.bsf	Solar Gard® Gold 65 on 3mm W/W	Bekaert Specialty Films, LLC	IGDB v12.6			3.023	0.469
204	Gold75.bsf	Solar Gard® Gold 75 on 3mm W/W	Bekaert Specialty Films, LLC	IGDB v12.6			3.023	0.584
205	Rosered.bsf	Solar Gard® Rose Red on 3mm W/W	Bekaert Specialty Films, LLC	IGDB v12.6			2.997	0.639
206	Royalblu.bsf	Solar Gard® Royal Blue on 3mm W/W	Bekaert Specialty Films, LLC	IGDB v12.6			2.997	0.602
207	Sb20.bsf	Solar Gard® Solar Bronze 20 on 3mm W/W	Bekaert Specialty Films, LLC	IGDB v12.6			3.023	0.130
208	Sb20_4.bsf	Amorcoat® 4 Mil Solar Bronze 20 on 3mm W/W	Bekaert Specialty Films, LLC	IGDB v12.6			3.073	0.102
209	Sb35.bsf	Solar Gard® Solar Bronze 35 on 3mm W/W	Bekaert Specialty Films, LLC	IGDB v12.6			3.023	0.224
210	Sb35_4.bsf	Amorcoat® 4 Mil Solar Bronze 35 on 3mm W/W	Bekaert Specialty Films, LLC	IGDB v12.6			3.073	0.207
211	Sb50.bsf	Solar Gard® Solar Bronze 50 on 3mm W/W	Bekaert Specialty Films, LLC	IGDB v12.6			3.023	0.317
212	Sb50_4.bsf	Amorcoat® 4 Mil Solar Bronze 50 on 3mm W/W	Bekaert Specialty Films, LLC	IGDB v12.6			3.073	0.318
213	Si20.bsf	Solar Gard® Silver 20 on 3mm W/W	Bekaert Specialty Films, LLC	IGDB v12.6			3.023	0.125
214	Si20_10.bsf	Amorcoat® 10 Mil Silver 20 on 3mm W/W	Bekaert Specialty Films, LLC	IGDB v12.6			3.226	0.130
215	Si20_4.bsf	Amorcoat® 4 Mil Silver 20 on 3mm W/W	Bekaert Specialty Films, LLC	IGDB v12.6			3.073	0.115

Figure 15: Window 6.3 International Glazing Database

The glass properties, which the IGDB provides, are for example the glass color, the thickness of a layer and of course the physical properties like the solar transmittance T_{sol} , the solar reflectance R_{sol} from the exterior and interior surface, the visible transmittance T_{vis} , as well as the visible reflectance R_{vis} . Furthermore properties like the infrared transmittance T_{ir} and the infrared or longwave emittance from the exterior and interior surface are provided.

To obtain a BSDF for the wished fenestration system, beneath the properties of each glass layer, some additional information has to be determined. As figure 16 shows, the number of layers, with their corresponding properties

from the IGDB, as well as the tilt of the fenestration and its dimensions. A further parameter is the environmental condition, which is default, as defined through the NFRC 100 (2010). So, after the NFRC 100 (2010, p. 20ff), the environmental conditions are defined for the winter as -18°C (0°F) outside temperature, and 21°C (70°F) inside temperature, with an outside convection coefficient of $26.0\text{ W/m}^2\text{K}$, a wind speed of 5.50 m/s (12.3 mph) and a solar radiation of 783 W/m^2 (248.2 Btu/hr-ft^2). The environmental conditions for the summer are different. Here the outside temperature is defined as 32°C (89°F) with a wind speed of 2.75 m/s (6.15 mph) and an outside convection coefficient of $15.0\text{ W/m}^2\text{K}$, as well as an inside temperature of 24°C (75°F) and a solar radiation of 0 W/m^2 .

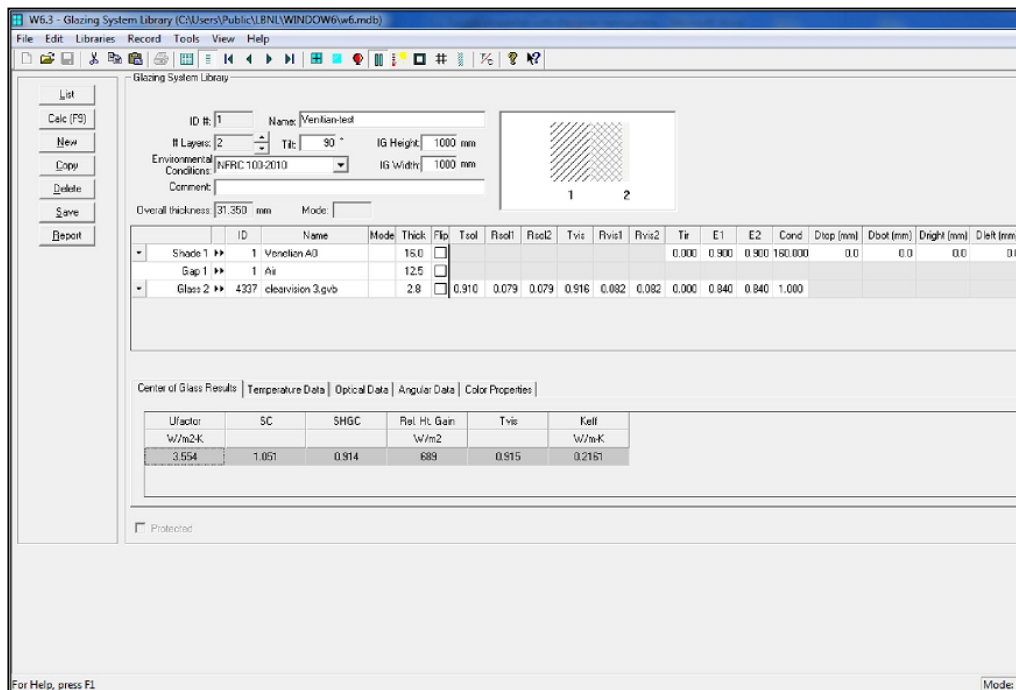


Figure 16: Window 6.3 Glazing System Library

Beneath the properties of the glazing layers and the environmental conditions, a shading device can also be added, especially for the purpose of this calculating tool. Window6 provides, therefore, for different shading devices, such as venetian blinds, woven shades or frits. Here it is possible to define the exact conditions of such a shading device. If, for example, a venetian blind is chosen, it is possible to vary the predefined settings until the desired shading device is adjusted, as shown in figure 17. These settings include slat width, spacing between the slats, and tilt angle of the slats, blind thickness, and rise.

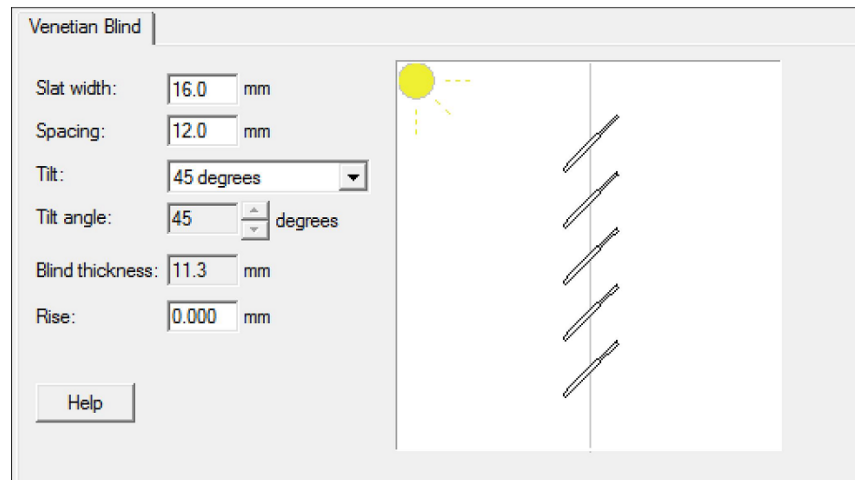


Figure 17: Window 6.3 Shading Layer Library showing the different properties

With the defined parameter, glazing, and shading layer, as well as the environmental conditions, Window6 is able to calculate the BSDF matrix for the chosen fenestration as described more precisely in chapter 2.4. The obtained BSDF matrix then provides the opportunity to connect the transmitted solar radiation with the surfaces of the indoor environment, as described in chapter 3.4 and 3.5.

3.3. Development of the virtual testing room and the human manikin

At the beginning of this research it was necessary to define precisely the environmental dimensions of the testing room. After evaluating several possibilities, the decision was made to use a room with a 3.0 m × 3.0 m square base and a height of 3.0 m. These properties match well to a room in a home or to a typical office, which allows for the transfer of the testing results to as many different environments as possible.

Furthermore, the testing room has three solid walls with opaque properties and one transparent wall, which allows the radiant transfer of the sun's rays. The window surface represented here simulates a 100 percent glazing facade like those often chosen by architects today. The floor and the ceiling have the same properties as the three solid walls.

After the environmental dimensions were settled on, the virtual room had to be realized in an input file, which would be used by different programs like Rhinoceros, and especially View3d. The Rhinoceros software was important in this process, to get a first visual output of the virtual room, so that errors in the input file may be remedied as soon as possible. In this first visual result, errors affecting different vertices can be detected very quickly and easily, which saves research time and reduces the danger of false results.

Concerning the numerical background of the simulation software which will be developed here, it was necessary to discretize the surfaces of the virtual room into triangular polygons. The software View3d, which calculates the necessary view factors for this tool, can handle only such triangular polygons. So each polygon consists of three, three-dimensional vertices with their associated x-, y- and z-coordinates.

In discretizing the surfaces into polygons, it was important to take their shape into account. This need arises from the possibility that trigonometrical equations, like those for calculation of solid angles, may diverge against infinity if shapes become too slight. This could lead to termination of the simulation, or to false results.

So the first virtual testing room was discretized into two polygons for each surface except the fenestration surface, which was discretized into four polygons because this surface would be the interesting one for calculating the solar load in later steps.

The View3d software will be used for calculating the view factors from each polygon of the occupant representing Manikin towards the polygons of the fenestration panel. The view factors are described more precisely in chapter 2.1.

This manikin thus represents a typical human body with sixteen separate body segments. To obtain some first simulation results and also get familiar with the topic, it was necessary to model the simulation as simply as possible, in order to keep the overview above the equations and their results. Otherwise it would be difficult to validate the out coming results and furthermore to verify the correct functionality of the equations.

The first simulation environment consists of the above described virtual test room with just a simple rectangular box with a one square meter base and a height of 1.5 m, standing in the middle of the room right on the floor, as shown in figure 18 on this page. This box thus represents a response surface to the solar beam, transmitted through the fenestration surface.

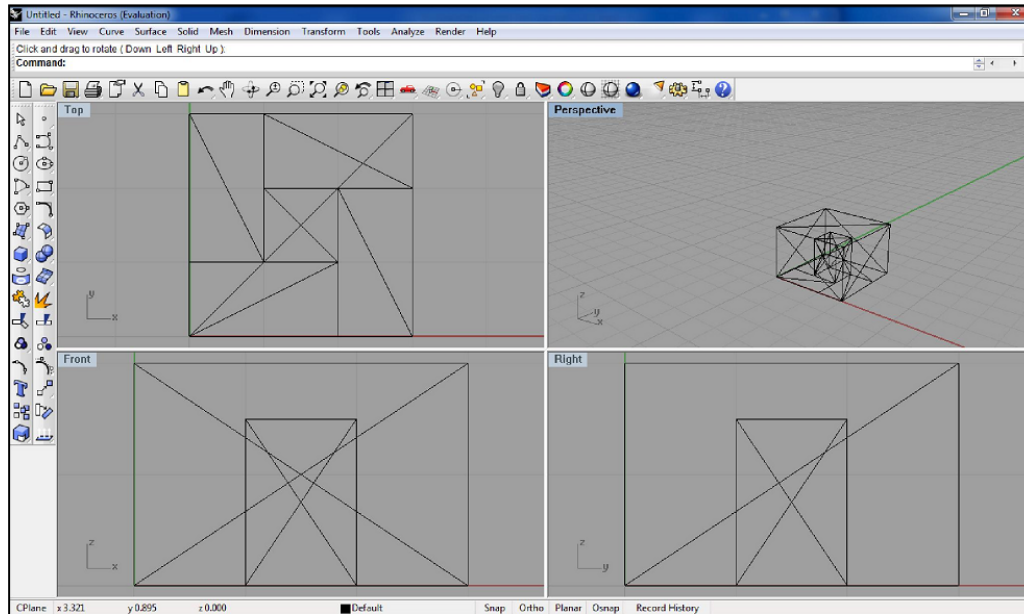


Figure 18: Virtual testing room with a rectangular box inside

Correct evaluation and validation of the obtained simulation results, follows in a replacement of the designed box through a human-like manikin, which is more precisely described in the following.

To replace the rough rectangular box with the manikin representing an occupant, an input file with the numerical discretization of the manikin has to be created. Therefore an already existing input file of an almost finished manikin had to be completed. This manikin should consist of the sixteen different body parts: head, chest, back, pelvis, left upper arm, right upper arm, left lower arm, right lower arm, left hand, right hand, left thigh, right thigh, left leg, right leg, left foot, and right foot. Each of these body parts is thus discretized into triangularly polygons, which finally results in a manikin of 220 polygons. The chosen manikin is shown in figure 19.

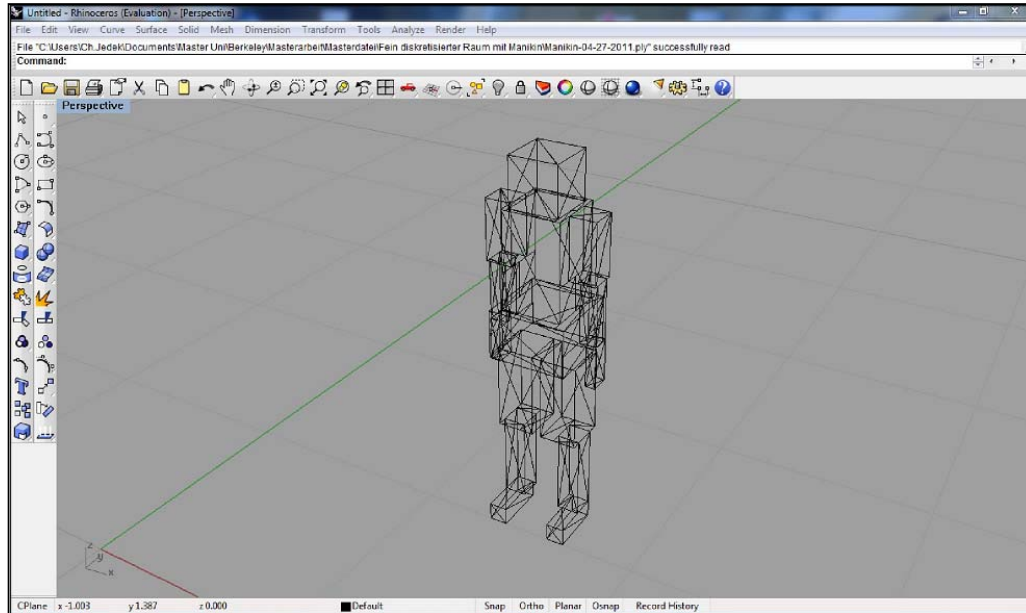


Figure 19: Rough discretized virtual manikin with sixteen body parts consisting of 220 triangular polygons.

As the manikin input file was only almost finished, the input file had to be examined exactly to detect existing errors. The focus thus lies on the exact position of every single vertex and, much more important, the kind of discretization of the different surfaces. This is so important because of the calculating of the view factors with the software View3d. By definition of the View3d protocols, every surface has to be determined counterclockwise by viewing on the surface, which looks towards the virtual room.

For example, looking at a surface of the manikin, that represents an area looking towards the ground, like the two polygons Pelvis 21 and Pelvis 22 of the discretized manikin input file. These two vertices have the following Cartesian coordinates:

"Pelvis 21"			
Vertex	X	Y	Z
63	1.667	1.014	0.818
64	1.333	1.014	0.818
65	1.333	1.092	0.818

"Pelvis 22"			
Vertex	X	Y	Z
63	1.667	1.014	0.818
67	1.667	1.092	0.818
65	1.333	1.092	0.818

Disregarding the orientation of the surface onto the virtual room follows in a determination as shown in figure 20. Although the two polygons are determined counterclockwise corresponding to figure 20, the determination is false, and will result in false view factors and a conversed surface normal.

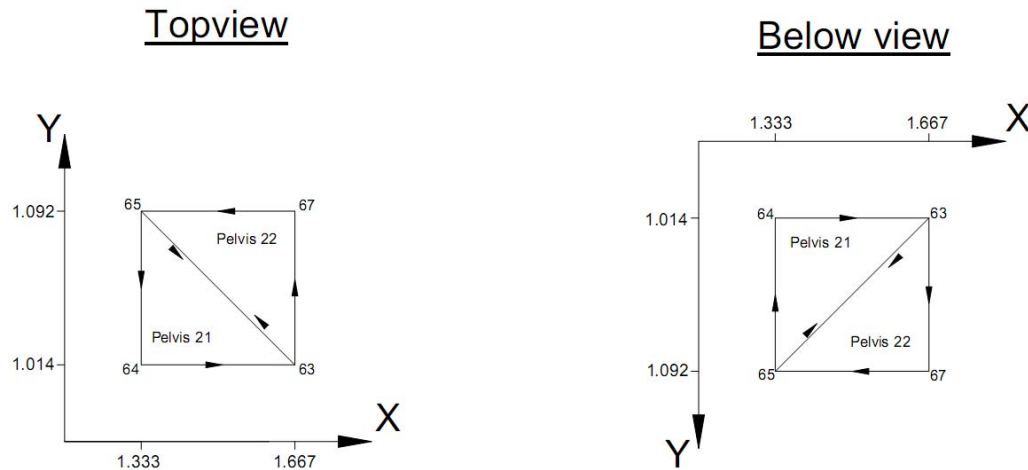


Figure 20: Difficulty of determining the right orientation for surfaces

As shown here, the determination of the two polygons under circumstance of the top view is counterclockwise and therefore right. But the view is on the one side of the surface, which looks into the pelvis instead to the outer environment. So to view the outer side of the surface, it has to be turn around the X-axis, as shown through the below view in figure 20. Now the chosen determination of the orientation has changed to clockwise, which is incorrect and results in various errors in subsequent calculations using the tool. This example shows how quickly such a mistake caused by an error in determination of surfaces could occur.

These mistakes don't show up when viewing the input file with the software Rhinoceros. Although the graphical presentation of the manikin here is looks right, there might occur errors caused by calculating the view factors with View3d, because Rhinoceros only pays attention to the vertices. The orientation of the surfaces is disregarded.

For developing an advanced calculating tool, this level of discretizing is sufficient for these calculations. The danger of involving errors would be relative slight. More polygons would result automatically in several more angles, which had to be validated as well, what fast comes to a point, where

an exactly validation from each polygon surface to the opponent becomes less and less comprehensible.

The finished calculation tool will use a more detailed manikin with about 2000 polygons for more precisely simulation results. Also important is, that the replacement of the simple box through the virtual manikin results in a new, and more precisely discretization of the fenestration facade. This is a necessary step to prevent mistakes by the Bin assignment. These coherences are described more precisely in chapter 3.4. However, as a result of this step, the fenestration façade will be discretized into 64 polygons.

For the completed manikin, an exact position in the testing room has to be determined. The most interesting areas for transmitted solar radiation are those close to the fenestration, as there is much less radiation in the deeper areas of the testing room. Furthermore, occupants usually remain close to the windows, as, for example, during work on a desk. So a standing manikin right in the middle of the fenestration façade, one meter from the fenestration surface, will be integrated. The finished calculation tool will be able to vary between a standing and sitting manikin, and to place or remove various pieces of furniture within the testing room.

Implementing the defined manikin into the testing room cannot be done by simply copying the manikin input file into the testing room input because every polygon surface has to be unique and clearly determined. This means no double surfaces as well as no undetermined spaces between the triangular polygons of the surfaces.

As the manikin stands on the floor, the discretized floor of the testing room has to be discretized new with the two missing surfaces covered by the manikin's feet, as shown in figure 21, so that the implemented manikin fills these voids and there is again a complete discretized environment. This means, that beneath the precisely discretized fenestration surface, the floor also had to be discretized into several polygons.

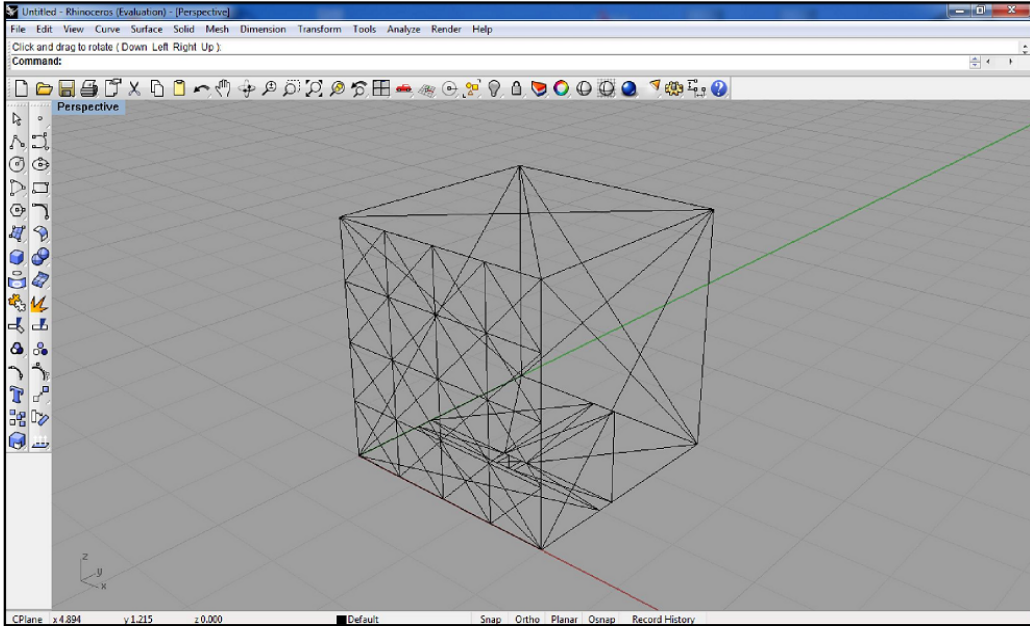


Figure 21: The virtual testing room with the chosen discretization used in the spreadsheet calculation program

Only the other surfaces – the other three walls and the ceiling – could be discretized more simply, as their influence on the calculation results for the thermal comfort of the manikin is slight. The complete environmental design, including the virtual room and the manikin is shown in figure 22.

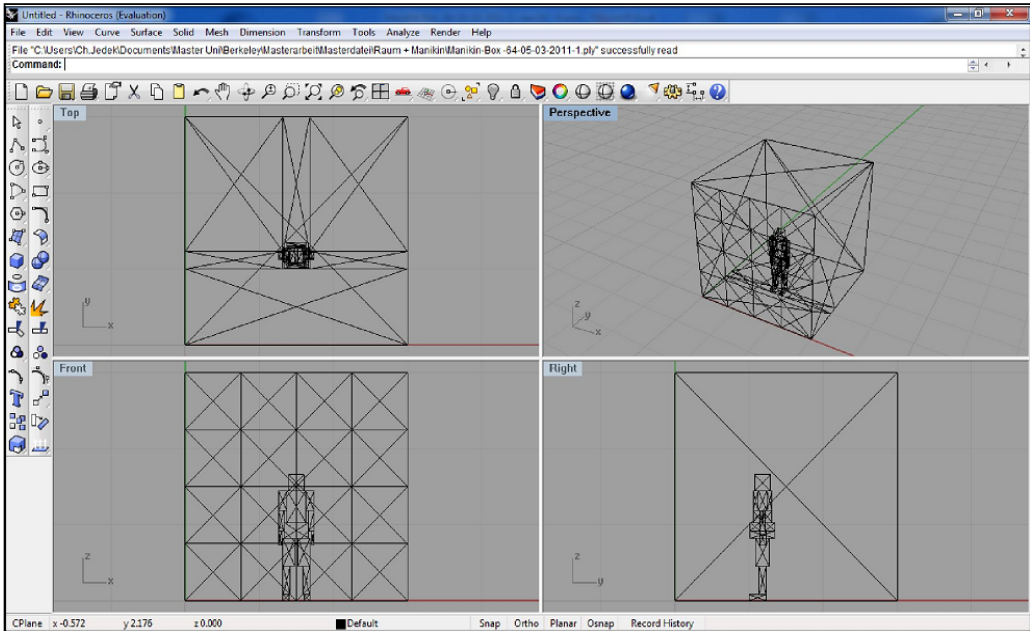


Figure 22: The virtual testing room after implementing the 220 polygon manikin

3.4. Connecting the manikin to the inner hemisphere

After completing the virtual environment with the chosen discretization of the fenestration facade and integrating the manikin into it, the connection between the manikin and the inner hemisphere of the fenestration surface has to be established. This relationship becomes necessary when the values of the distribution effects for the different types of fenestration, obtained from the BSDF-matrix of Window6, are integrated. The BSDF matrix is described above in chapter 2.4.

As described there, the BSDF-matrix involves a solar transmission coefficient for each Bin of the outer and inner hemisphere. So connecting the BSDF-matrix into the calculation of the solar load allows determining how much solar radiation, emitted from the fenestration surface, with the respective angle to one of the different manikin polygons, is directly intercepted by this manikin polygon.

Before the assignment of the different manikin polygons to their respective Bin on the inner hemisphere can be made, there is one important step to solve, before starting any calculations of the spherical angles. Based on the incident radiation and the scattering distribution function that will be obtained from Window6 for each transparent sub-surface, the specific solar intensity from each sub-surface radiating to each occupant polygon could be determined.

For an exact calculation of this radiation amount though it is necessary to know which Bin of the inner hemisphere belongs to which polygon surface of the manikin, so that these Bins could be referred to the appropriate index of the Window6-calculated BSDF-array. Using a BSDF full size Array with 145 polar angles θ allows the most exact level of detail for this calculation tool, but using a full size array also results in an average Bin angle of 0.02 degree. So if the solid angles from the centroid of a manikin polygon to the appropriate vertices of each fenestration polygon were notable greater as 0.02 degree, the assignment to one Bin of the inner hemisphere becomes imprecisely because of possible skipping Bins.

As the polygons of the manikin were fixed, the fenestration surface has to be adjusted, so that the solid angles match the Bin angles of the inner hemisphere. So the solid angles with the actually fenestration discretizing have to be examined. Thus, the shortest distance between the manikin polygon and the fenestration polygon was decisive, because of the largest solid angle existing there. Calculating the solid angle is carried out by using equation 31, after Kost (1994, p. 160).

$$\tan\left(\frac{\omega}{2}\right) = \frac{|\vec{j} \cdot (\vec{k} \times \vec{l})|}{1 + \vec{j} \cdot \vec{k} + \vec{k} \cdot \vec{l} + \vec{l} \cdot \vec{j}} \quad (31)$$

A fenestration facade with a discretization of four polygons will not be sufficient to achieve the above described solid angle of 0.02 degree. A fenestration, discretized into sixteen polygons, results in a solid angles of 0.395 degree for one pelvis polygon to the nearest fenestration polygon, which corresponds the shortest distance between both surfaces, as in annex 6 shown. This is about twenty times greater than the intended 0.02 degree. As a result the fenestration has to be discretized more precisely. A fenestration façade, consisting of 64 polygons, results in a solid angle of 0.026 degree, as in Annex 6 shown. The discrepancy between these both angles is sufficient to reckon that not too many Bins were bypassed in during calculations.

This discretizing only takes effect for this special position and this special discretizing of the manikin. Every single variation belonging to the manikin, results in different solid angles towards the fenestration façade, so that the fenestration has to be examined once again.

To determine which Bin of the respective fenestration polygon belongs to the respective manikin polygon, there were some additional geometrical calculations necessary. As in chapter 2.4 described, each Bin has its unique array of geometrical angles. So it is important to get the spherical angles Θ (Theta) and Φ (Phi) for this environmental design, which represents the polar and the azimuth angle. Through this assignment and the data of the BSDF produced by Window6, it is possible to calculate the amount of direct and diffuse solar radiation, transmitted through the fenestration onto the individual surfaces of the manikin.

To obtain these spherical angles, there were some working steps to do. At first it is necessary to calculate the centroid for every triangularly polygon as well from the manikin as from the fenestration surface. Using the equation 32 allows to calculate the centroid of a three dimensional triangularly polygon.

$$\vec{s}_i = \frac{1}{3} \cdot (\overrightarrow{OV_1} + \overrightarrow{OV_2} + \overrightarrow{OV_3}) \quad (32)$$

With these three-dimensional centroids and the equation 33, it is possible to calculate the distance vectors between each fenestration and manikin polygon. The distance vector thus is oriented from the fenestration surface to the manikin polygon, what becomes important at later following calculation steps.

$$\vec{s}_{j,i} = \vec{s}_j - \vec{s}_i = \begin{pmatrix} x_{s_i} \\ y_{s_i} \\ z_{s_i} \end{pmatrix} - \begin{pmatrix} x_{s_j} \\ y_{s_j} \\ z_{s_j} \end{pmatrix} \quad (33)$$

Using equation 34 allows normalizing the distance vectors obtained.

$$\vec{s}_{j,i} = \frac{\begin{pmatrix} x_{s_{j,i}} \\ y_{s_{j,i}} \\ z_{s_{j,i}} \end{pmatrix}}{\sqrt{x_{s_{j,i}}^2 + y_{s_{j,i}}^2 + z_{s_{j,i}}^2}} \quad (34)$$

With these normalized vectors, a transformation of the Cartesian coordinates into spherical coordinates can be done. The hemisphere lies on the fenestration façade, which corresponds to the X and Z layer and expands towards the positive Y axis. The structures of such spherical coordinates were shown previous in figure 13, remembering that the graphic shown there is a hemisphere lying on the X and Y layer, expanding towards the positive Z axis. The coordinate systems given for the two spherical angles are graphical described as shown previous in figure 14.

With this Cartesian coordinate system, the equations for calculating the spherical angles may be solved. The equations for these transformations are for the azimuth angle the equation 35 as shown below.

$$\varphi = \left\{ \begin{array}{l} \arctan\left(\frac{x}{z}\right) + \pi, \text{ if } z < 0 \cap x \geq 0 \\ \arctan\left(\frac{x}{z}\right) - \pi, \text{ if } z < 0 \cap x < 0 \\ \arctan\left(\frac{x}{z}\right), \text{ if } z > 0 \\ \operatorname{sgn}(x)\left(\frac{\pi}{2}\right), \text{ if } z = 0 \end{array} \right\} \quad (35)$$

Here it is obvious that the kind of transformation equation depends on the values from the x and z component. This distinction of the four equations is thus very important for getting the correct range of angles from $-\pi$ to $+\pi$ in rad, or -180° to $+180^\circ$ in degree. Otherwise mistakes will show up very quickly.

For example by using the third determination without taking into account the requirements, which may be often found in reference literature, the results of the angles range from $-\pi/2$ to $+\pi/2$, or 90° to $+90^\circ$. This is caused by the definition of the arctan, also often written as \tan^{-1} , which ranges only between these two angles. So to get the full 360° circle, the four determinations were necessary. Equation 36 for the polar angle on the other hand is less complex:

$$\theta = \left\{ \arctan\left(\frac{\sqrt{z^2+x^2}}{y}\right) \right\} \quad (36)$$

As may be seen in this equation, there is not so much to take into account as in the azimuth equation. After transforming the Cartesian vectors into spherical vectors, the azimuth and polar angle could be calculated.

With the normalized distance vectors and the surface normal of the fenestration polygons, the spherical angles Phi and Theta could be calculated by using equations 35 and 36. The validation of the calculation results is an important step after using every new equation in order to detect errors as soon as possible. Otherwise these undetected errors will result in false results in later calculations. Determining the reason for these wrong results might then be very time intensive.

Also the validation itself is very time intensive because of the sheer number of calculation results. Although the virtual room and the manikin are simply and roughly discretized, the calculation of the spherical angles result in 14,080 values (64 fenestration polygons multiplied with the 220 manikin polygons) for each of both angles. Altogether, about 28,160 individual angles should be validated. Indeed this validation cannot be done by exact mathematical calculation of each angle, so the results have to be estimated, corresponding to their truth. This means only some special relationships between manikin polygons and fenestration surfaces can be examined and proofed for their validity.

For example, if the polar angle Θ of one upper fenestration surface is examined for the moving results beginning at the head of the manikin to the foot, the values should begin at a small one and rise on the way down to the foot. If there are some values which stand out of the continuous rising, there might be an error occurring. On the other hand, examining the azimuth angle Φ of, for example, one polygon in the left upper corner to the manikin, starting at the left side and moving to the right side will start with a low value and rise continuously in line with the Θ angle until the right side of the manikin is reached.

With the obtained 28,160 spherical angles Θ and Φ , an assignment for each distance vector to their corresponding Bin on the inner hemisphere can be made. But to do this several requests are necessary. The first request figures out what ring of the inner hemisphere matches to the corresponding spherical angle Θ . As shown in Annex 4, every ring has its own range of angle Θ . After determining what ring corresponds to the angle Θ , the second request figures out what Bin on this ring matches to the corresponding spherical angle Φ . Annex 4 also shows the range of angle Φ for every Bin on each ring of the inner hemisphere.

For example, if the spherical angle Θ of the corresponding distance vector is between 5 and 15 degree, the result of the first request is that the Bin lies in the second ring of the inner hemisphere. Further, if the spherical angle Φ is between 112.5 and 157.5 degree, the second request gives the result, that the corresponding Bin is the number 5 on the inner hemisphere. The discretization of the outer hemisphere is shown in Annex 5.

As this short example shows, it is possible to determine the corresponding Bin for every single distance vector. How exact this determination is, depends on the discretization of the fenestration surface and the virtual manikin, as in chapter 3.3 more detailed described. The smaller the solid angle from the manikin polygon to the fenestration polygon is chosen, the more precisely is the Bin assignment in this step, because the danger to skip one Bin gets less.

3.5. Development of the solar load calculation under use of calculated view factors

Using the connection of the manikin to the inner hemisphere of the fenestration façade that has been obtained, the solar load can be calculated. The amount of solar load, especially on the virtual manikin, is the main result of this tool. These output data, together with the, from View3D calculated view factors, can be used in ongoing steps for example to calculate thermal comfort with the Human Thermal Comfort Model, developed by the University of California at Berkeley. The Human Thermal Comfort Model is described in more detail in Annex 1. To obtain these final calculation results, all the values calculated in steps before have to appear together.

As described during the previous chapter, the incidence angle of a given solar radiation beam was assigned to a specific Bin on the outer hemisphere of the fenestration façade. This specific value determines which column of the BSDF matrix has to be used. Together with the link of the manikin to the inner hemisphere of the façade, which results in a specific Bin for every distance vector from each fenestration polygon towards every manikin polygon, the transmission of the solar radiation through the fenestration façade can be calculated. Here the Bin of the inner hemisphere determines the row of the given column, and therefore the specific transmission coefficient delivered by the BSDF matrix. The BSDF matrix, calculated by Window6 cannot be used in this form.

The given values of the BSDF matrix thus produced deliver a different transmission coefficient for each individual Bin of the hemisphere. But as these Bins are not all of the same size, an integral over each Bin and its corresponding transmission coefficient has to be done to get the real amount of transmittance. So, after Carli (2006, p. 30), the various values of the BSDF matrix have to be multiplied with an index Λ , which represents this integrating operation. More precisely Lambda represents, after Carli (2006, p. 30), a geometrical quantity, which is associated with the partitioning of a solid angle. So each Bin has its own corresponding Lambda value, which will be calculated, after Carli (2006, p. 30), as in equation 37 shown.

$$\Lambda = 1/2 \cdot \left(\sin^2(\theta_i^{hi}) - \sin^2(\theta_i^{lo}) \right) \cdot \Delta\varphi_i \quad , i = 1, \dots, N_\theta \quad (37)$$

The index $\Delta\varphi_i$ in this equation defines the size of the spherical angle phi by subtracting the lower value from the higher. If the directions of the Bins in each ring are equal, what means, that the spherical angles phi are similar for each individual ring, the value $\Delta\varphi_i$ of equation 37 can be replaced through the value $2\pi/N_{\varphi i}$.

So if the Bins on each ring are equal, the size of each $\Delta\varphi_i$ can be replaced through the amount of Bins of that ring, written as $N_{\varphi i}$. The indices hi and lo stand for higher and lower, which describes the higher and lower boundaries of the spherical angle theta for each individual Bin on the hemisphere.

The following example explains this in more detail. As shown in figure 23, a spherical hemisphere projected onto the x-y plane is divided into N_θ rings. Each ring is defined through a high and a low angle theta, representing the two boundaries of the ring. Note that the first ring actually is more precisely described as a cap. So the boundaries vary from the first, starting with $\theta_1^{lo} = 0^\circ$ towards the last, and ending with $\theta_{N_\theta}^{hi} = 90^\circ$.

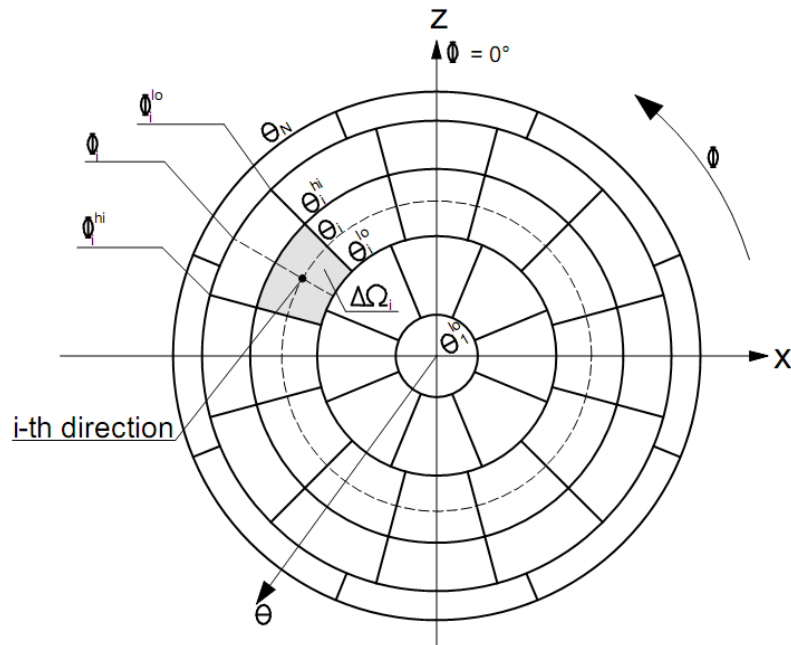


Figure 23: Bin determination of a quarter size BSDF by using lower and higher boundaries of theta and phi, according to Carli (2006, p. 31)

Figure 24 shows the kind of segmentation for the spherical hemisphere, projected onto the x-z plane. This figure explains more precisely how the different theta angles define the several rings of the hemisphere.

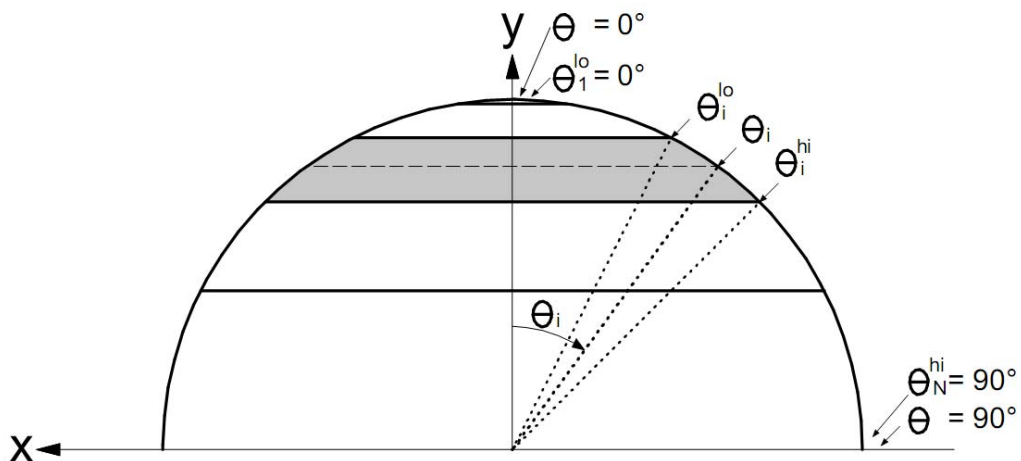


Figure 24: Ring determination of the BSDF, according to Carli (2006, p. 32)

As in this example, the ring on the hemisphere is defined through the lower angle $\theta^{lo} = 15^\circ$ and the higher angle $\theta^{hi} = 45^\circ$. So following equation 37, concerning the equal $\Delta\phi$, the value lambda for this ring is determined by using equation 38:

$$\Lambda = 1/2 \cdot (\sin^2(45 \cdot \pi/180) - \sin^2(15 \cdot \pi/180)) \cdot 2\pi/8 = 0.17 \quad (38)$$

Using the obtained values of the different lambda by multiplying with the BSDF matrix of Window6 as shown in equation 39, produces a new matrix with the exact amount of transmission for each Bin on the hemisphere. This can be validated by adding up all values of one column, which represents the integral value of the whole inner hemisphere for a given incidence angle on the outer hemisphere.

$$\tau_{BSDF} = \Lambda \cdot BSDF_{i,j} \quad (39)$$

The indices i and j therein stand for the row and the column of the BSDF matrix. The new modified BSDF matrix cannot yet be used this way for calculating the solar load. Before that, every transmission coefficient has to be multiplied by the amount of Bins for the whole hemisphere, as in equation 40 described.

$$\tau_{\tau_{sol}} = \sum_1^n BSDF_i \cdot \tau_{BSDF} \quad (40)$$

For example by using a full size matrix, n has to be 145. This has the reason, that for the calculation of the solar load of one specific Bin, it will be assumed that all other directions of radiant transmission, or the other Bins, have the identical amount of transmission. This is called a Lambertian radiator, which is described more precisely in chapter 2.1.

By treating the transmission coefficient of the individual Bins as a Lambertian radiator, the new matrix is obtained. To calculate the solar load for the manikin and the environment, first the solar load for every coherence between the different polygons of manikin and environment have to be calculated. To do this, the value for the solar transmission will be requested for each coherence between the different polygons, what result in 16,896 values, appropriate 264 values for the manikin and the environment

deducting the fenestration façade, multiplied with 64 values for the fenestration façade. The solar load for each coherence then will be calculated using equation 41.

$$W_{sol}[W] = F_{x \rightarrow y} [-] \cdot A_{fenestration}[m^2] \cdot E_{solar}[W/m^2] \cdot T_{T_{sol}}[-] \quad (41)$$

The index W_{sol} stands for the amount of solar load on one polygon of the manikin or the environment, while the index $F_{x \rightarrow y}$ stands for the view factor from the manikin polygon towards the fenestration surface, as described in chapter 2.1. The index $A_{fenestration}$ is a value for the surface area of the corresponding fenestration polygon. The amount of the chosen solar radiation is delivered by the index E_{solar} . The solar load for the sixteen body parts, for both the whole manikin and the environment finally will be obtained by adding their respective values.

3.6. Obtaining the solar load values for the body parts of the Manikin from the simulation results

The obtained the calculation results for the solar load, as described in the previous chapters, the calculation values for every subsurface have to be modified to get the solar load values for all sixteen body parts of the virtual Manikin.

The necessary calculating results of the solar load tool thus are the solar load on each of the sixteen body segments and the view factor from each body segment towards the surrounding surfaces. As described in chapter 3.5, the solar load will be calculated for each polygon of the manikin and the surrounding surfaces of the environment, except the fenestration façade. This results in 16,896 different values for the solar load (64 fenestration surfaces multiplied by 264 room and manikin polygons). To obtain the special solar load on each of the sixteen body segments, the values of each body segment polygon for all 64 fenestration surfaces have to be added up. This will be done, for example, for the head of the manikin, which includes 10 polygons, by using equation 42.

$$W_{sol}^{head} = \sum_{i=1}^{64} \sum_{j=1}^{10} W_{sol,i,j} \quad (42)$$

Applying this equation in a similar way to the other 15 body segments result in the solar load for the manikin as shown in table 2. The view factors have to be summed, too, for all body segments in relation to the surrounding surfaces. This summing up occurs, again taking the example of the head, by the use of equation 43. These calculation results for the solar load of every single body segment can then be used in a further step as input parameter for a thermal comfort calculation, as for example the Berkeley Human Thermal Comfort Model (described in more detail in Annex 1).

$$F_{i,k \rightarrow j,m} = \sum_{m=1}^{64} \frac{\sum_{l=1}^{10} F_{i,k,l \rightarrow j,m} \cdot A_{i,k,l}}{\sum_{l=1}^{10} A_{i,k,l}} \quad (43)$$

The indices therein are defined as follows:

- i = manikin
- k = body segment
- l = manikin polygon
- j = fenestration surface
- m = fenestration polygon
- F = View factor
- A = surface area

Table 2: Example of the solar load on each of the 16 body segments for a diffusing shade and a given solar radiation

Body part	Solar load [W]
head	17.92
chest	32.16
back	0.64
pelvis	24.36
rightupperarm	8.86
leftupperarm	8.86
rightlowerarm	4.78
leftlowerarm	4.78
lefthand	2.32
righthand	2.32
rightthigh	16.28
leftthigh	16.32
rightleg	8.7
leftleg	8.74
rightfoot	3.03
leftfoot	3.01

3.7. Parameter study with an advanced discretization

As no calculation tool is useful without the possibility of a practical application, this chapter describes the application of the developed calculation tool on two different buildings in the United States. To accomplish realistic simulation results, the simulation properties of the developed and simplified model have to be modified. These modifications consist of a more detailed virtual manikin as well as a more precise determined simulation room.

However the simulation properties of the developed tool were sufficient to validate the program itself, the simplified manikin is not representative for a realistic human body. Furthermore, as usual for numerical simulations, calculations are sensitive to varies of the grid and the discretization, which makes it necessary to examine the effects of changes of these parameters to understand and trust the simulation results.

As the two opposite sides of possible glass properties, the examination is made for a theoretical complete diffuse BSDF as well as a complete specular BSDF, both with a solar transmittance of 1.0. This kind of examination is caused by the practical application of the calculation tool, where the fenestration properties usually are lying between. The simulation with the fully diffuse BSDF is therefore focused on the overall solar load into the simulation room, while the one for the specular BSDF is focused on single surfaces.

Boundary conditions for the following examination of the fully diffuse properties are a virtual testing room of 3.0m width, 3.0m depth, and 3.0m height, as well as a solar radiation of 800W/m² and a fully diffuse BSDF with a solar transmission coefficient of 1.0. Based on these conditions, the overall solar load into the room should be 7200W. Furthermore, caused through the same emittance of the diffuse BSDF into every direction, this solar load should not change for varying Bins.

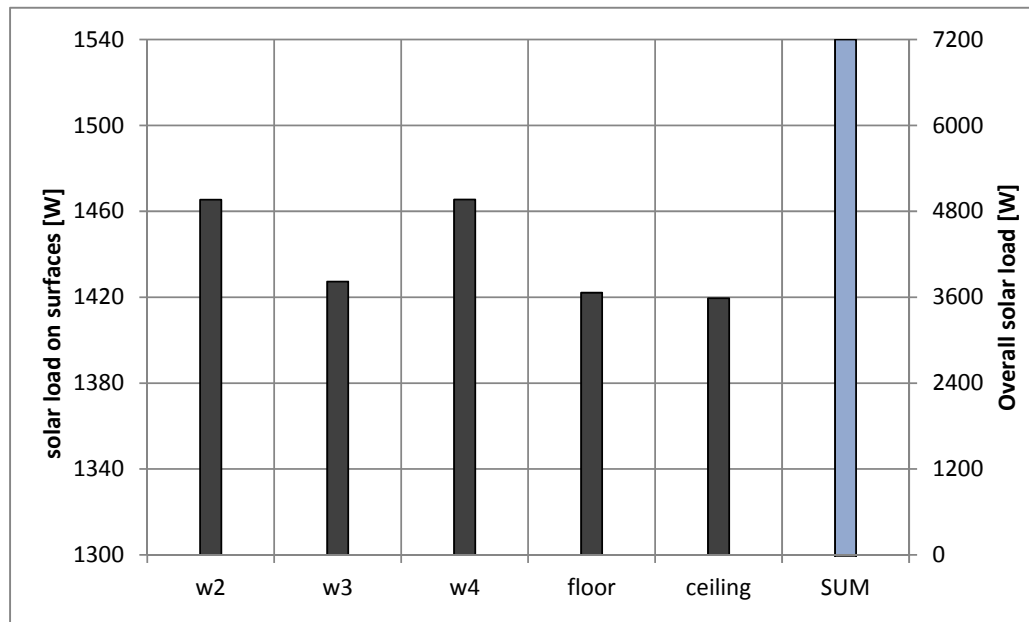


Figure 25: Solar load on the room walls for diffuse fenestration properties.

The simulation results, as shown in figure 25, confirm this assumption. So is the total amount of solar radiation for all five surrounding surfaces exact 7200W, and do not change for varying Bins on the outer hemisphere. Additionally, the solar load on the single surfaces is representative for the symmetric simulation room. Hence the opposite walls W2 and W4 as well as floor and ceiling, each get an equal amount of solar load.

So as this examination validates the calculation tool for fenestration devices with diffusing properties, the following pages consists of the examination of the calculation tool for fenestration devices with specular properties. Caused by the development of this calculation tool especially for scattering distribution properties of windows, this part has to be examined very intense to validate functionality of this tool even for a non-diffuse fenestration device, so that simulation results in practical application can be trusted.

Generally there are several different kinds of discretization meshes for numerical calculations. Existing calculation programs usually provide a given kind of mesh which has to be used. In the case of this simulation program the software view3d determine the use of a triangular discretization mesh to calculate the view factors, but is thereby capable of using varying forms of triangles. So examining possible effects of different grids is a necessary step to optimize the calculation progress.

In this case two different kinds of discretization grids are examined. The first one consists of rectangular triangles with the same height as width, while the second one consists of non-rectangular triangles with half height as width. The different structures of both grids are shown in figure 26 and 27.

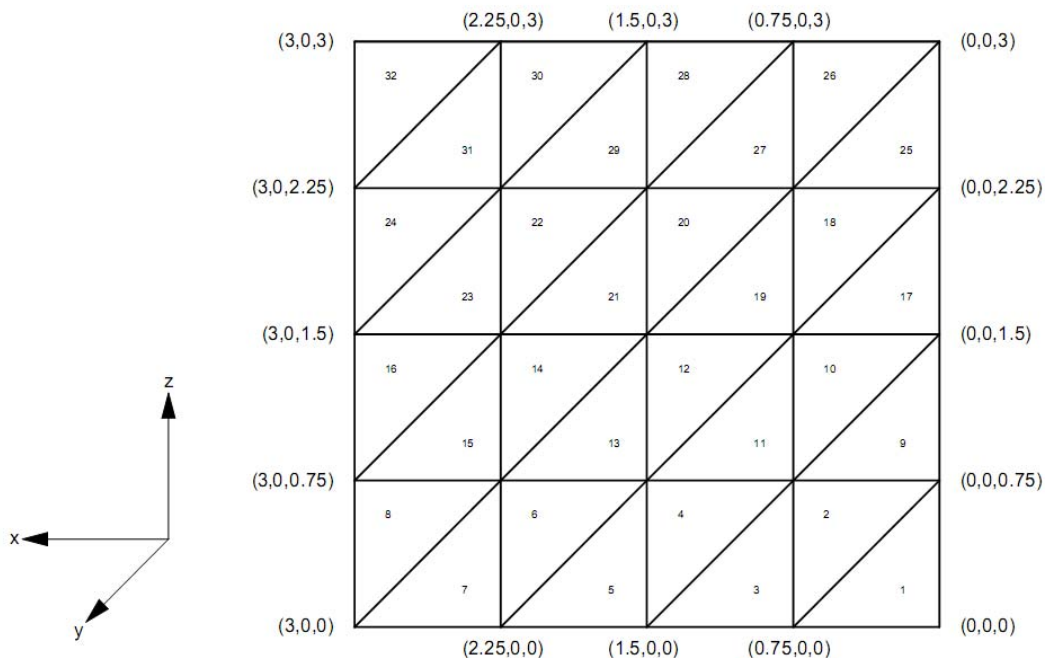


Figure 26: Surface structure of the 1st discretization mesh ($dx=75\text{cm}$, $dz=75\text{cm}$)

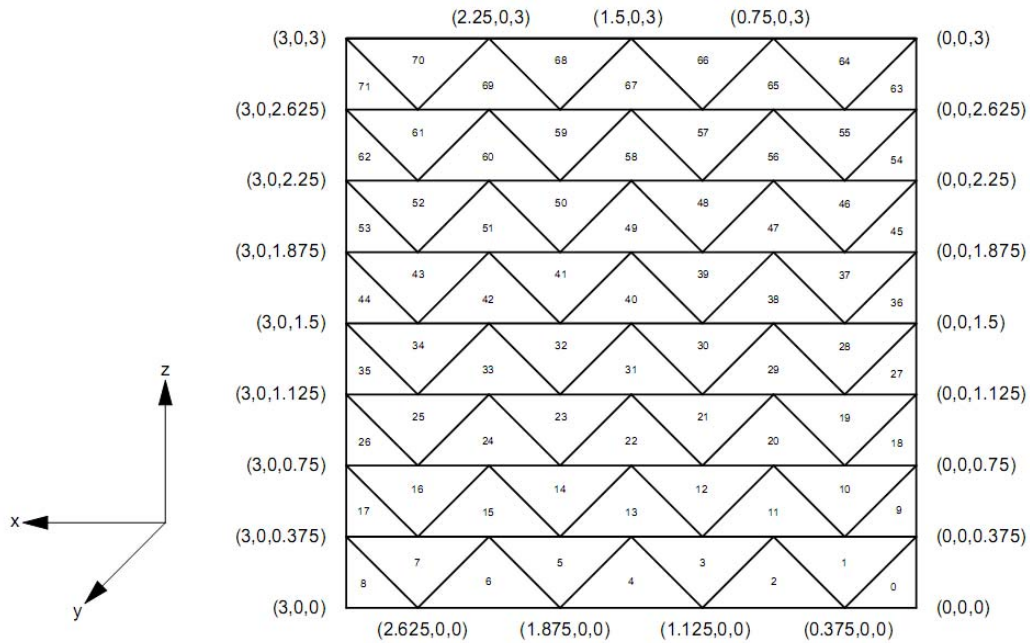
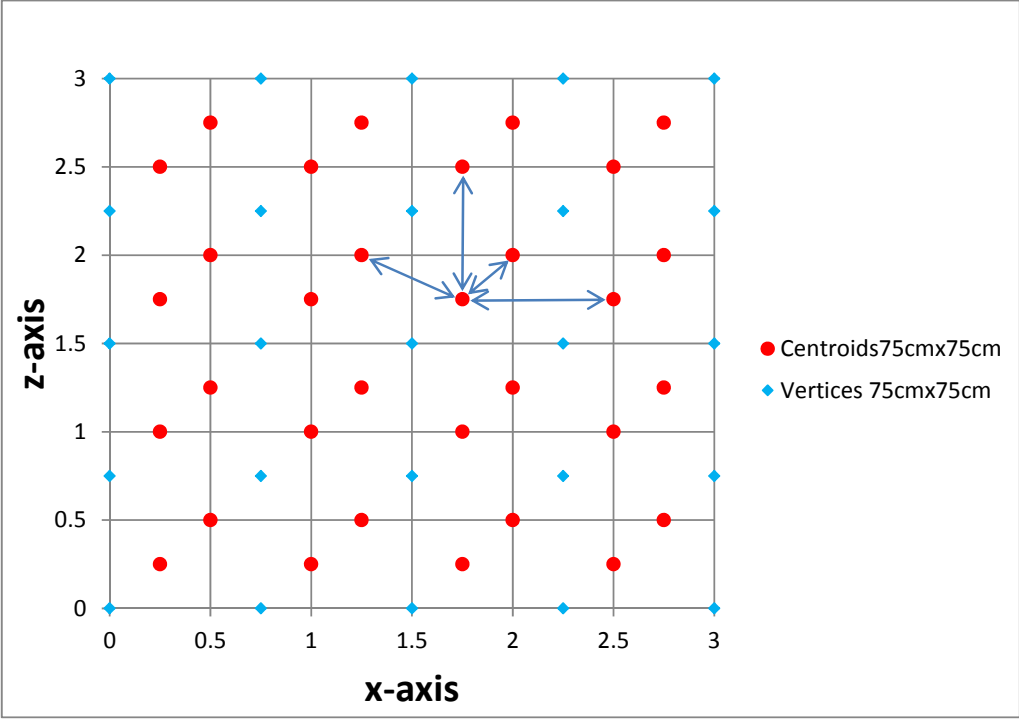


Figure 27: Surface structure of the 2nd discretization mesh ($dx=75\text{cm}$, $dz=37.5\text{cm}$)

The main difference of these both grids is especially the arrangement of the surface centroid positions. The idea behind is the assumption that a more similar arrangement, with nearly equal distances between the triangle centroids results in more precise calculation values. Hence the centroids of the first discretization are arranged quite unequally, and the second discretization exhibits much more equal distances between the triangles centroids, except the ones of the triangles on the left and right edge. An example of the arrangement of the triangle centroids for both discretization grids is shown in figure 28 and 29.



[Figure 28: Centroid arrangement for the 1st discretization mesh (75 cm × 75 cm)]

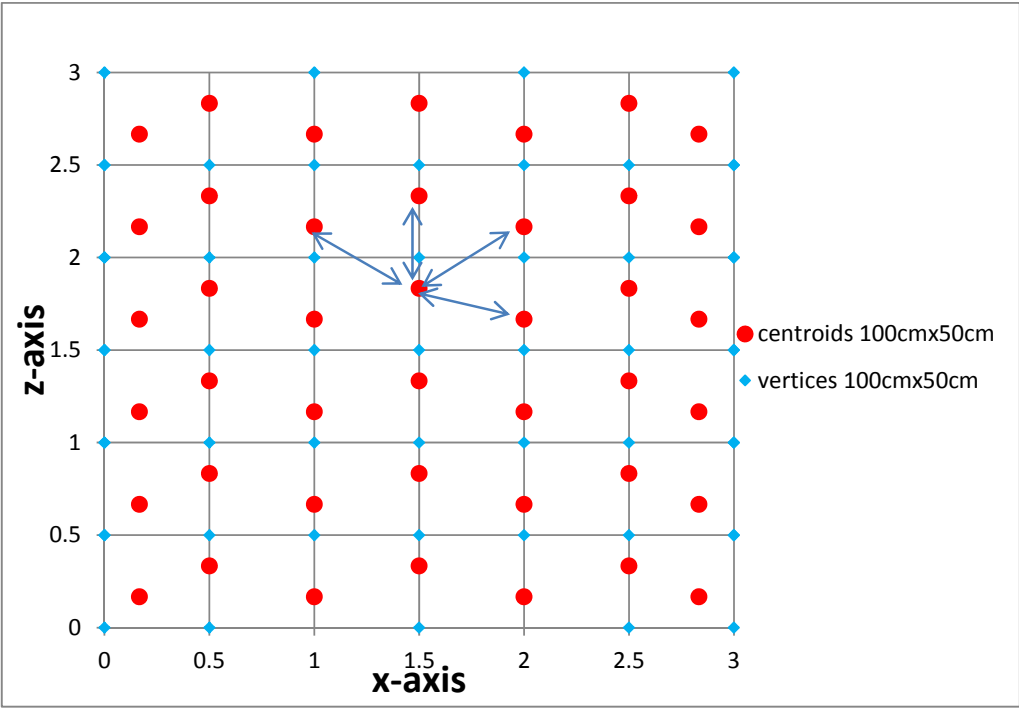


Figure 29: Centroid arrangement for the 2nd discretization mesh (100 cm × 50 cm)

As shown here, the centroids of the first discretization mesh in figure 28 do not have an equal arrangement. The distance between the two triangles of one square is around half as long as the distances towards the surrounding centroids. The second discretization mesh on the other side shows in figure 29 under a ratio of $dy = 0.5 \cdot dx$ a more equal arrangement of the centroids towards each other, with the exception of the centroids on both sides.

To analyze possible differences of the simulation results, both discretization meshes are examined under the same simulation conditions. These are clear sky conditions with a solar radiation of 800 W/m^2 and a fenestration device with a theoretical specular BSDF and a solar transmittance of 1.0 on a $3 \text{ m} \times 3 \text{ m} \times 3 \text{ m}$ cube. The theoretical specular BSDF is used, because it represents the most critical case. Simulations with diffuse BSDFs result in more precise calculation values as shown in the previous chapter. Point of interest for this examination is the solar radiation on the opposite wall of the fenestration surface. The fenestration surface thereby is assumed as 100% of the wall, which means for example that under a perpendicular incidence angle through Bin 1 the opposite wall should get an overall solar load of 7200 watts ($800 \text{ W/m}^2 \cdot 3 \text{ m} \cdot 3 \text{ m}$).

To examine the effects on the opposite wall, simplified, horizontal incidence angles on the right side of the outer hemisphere are used for the simulation, like shown in figure 30. Hence it is possible to predict the expected solar load through a simple 2-dimensional equation, like shown in equation 44 and figure 31. This equation allows determining under use of equation 45 an upper as well as lower boundary, representative for the range of angle theta like described in chapter 2.4 before.

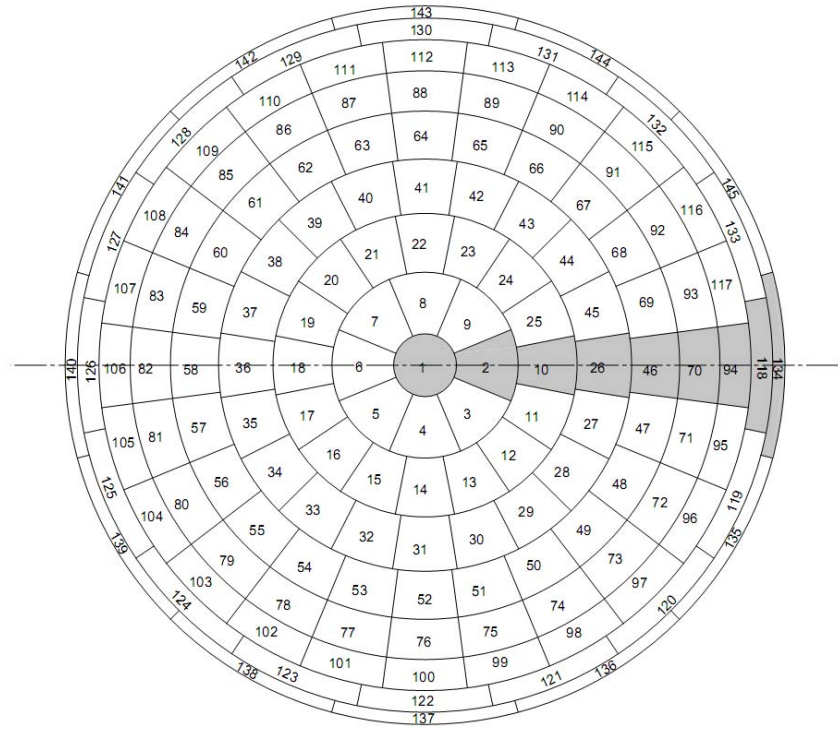


Figure 30: Outer BSRDF hemisphere with marked simulation Bins on the horizontal axis.

$$dx = x - y \cdot \tan(\theta) \quad [44]$$

$$\text{Solarload}(0 \leq \theta \leq 90^\circ) = 800W/m^2 \cdot 3.0m \cdot (d_x \cdot \cos(\theta)) \quad [45]$$

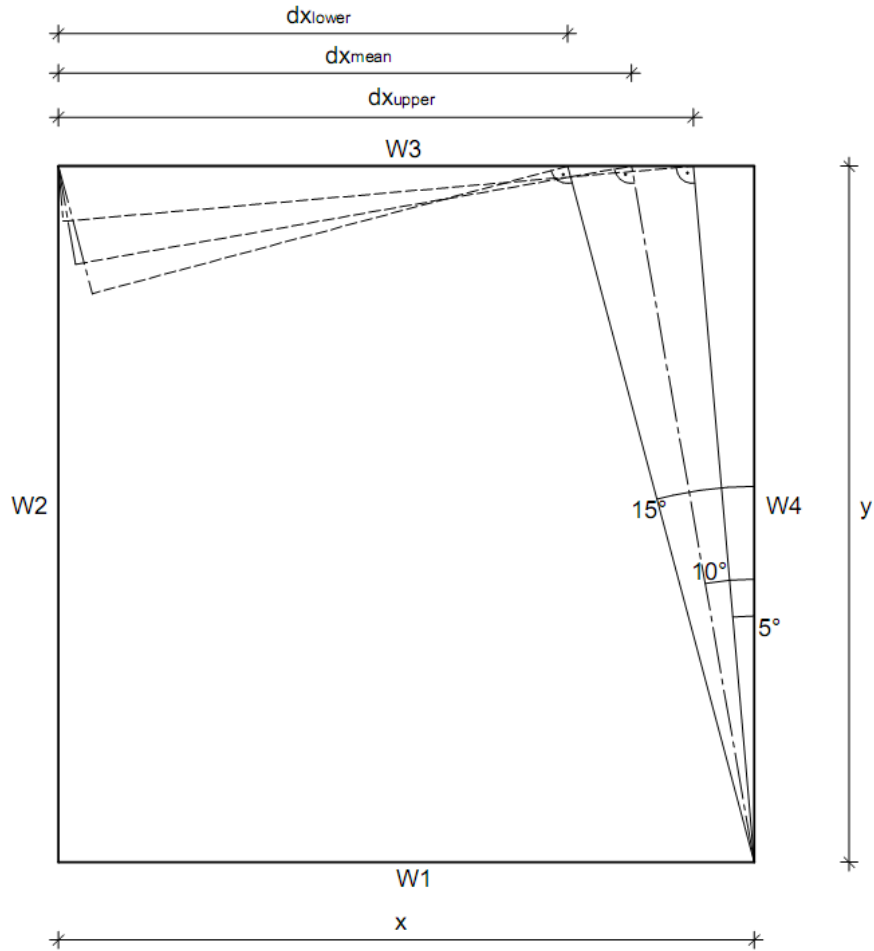


Figure 31: Solar load calculation of the corresponding surface on the opposite wall W3 for the BSDF Bin=2 ($5^\circ \leq \theta \leq 15^\circ$) on a $3\text{ m} \times 3\text{ m}$ simulation room

Under these conditions a simulation over the outer hemisphere Bins 1, 2, 10, 26 and 46 (see figure 30) shows the differences between both discretization grids. Further Bins are not simulated, since they do not match the opposite wall. The first simulation is based on a rough discretization with a fenestration wall consisting of 42 surfaces for each grid.

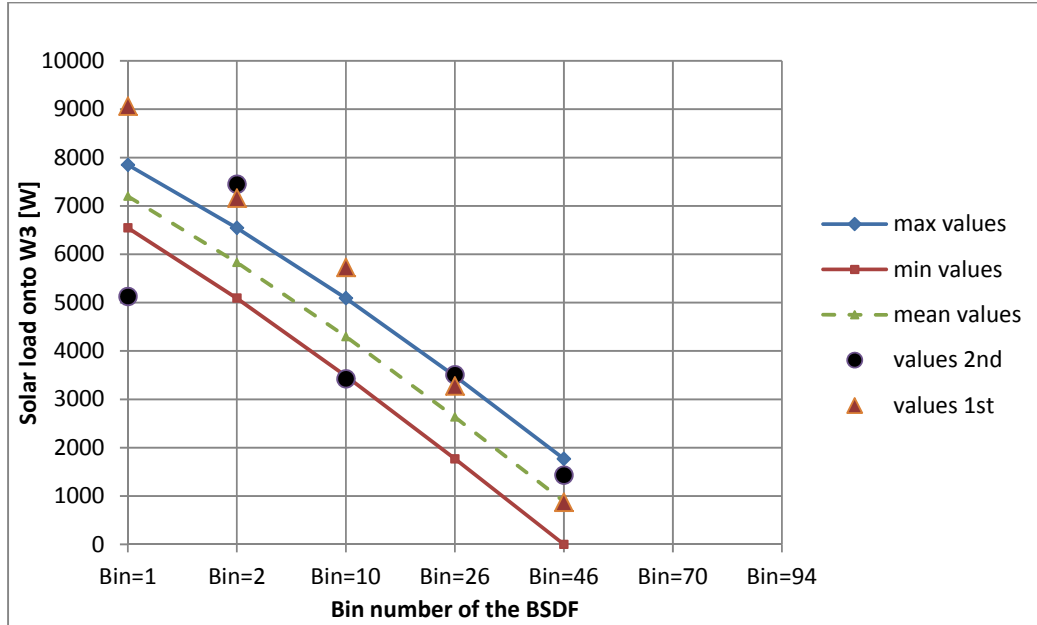


Figure 32: Value comparison for the 1st (50 cm × 50 cm) and 2nd (75 cm × 37.5 cm) discretization mesh for a rough discretization at 3.0 m room depth

The results of figure 32 show that the 1st grid has more precise results, even while both grids do not match the predicted solar radiation. By adding up the deviations of the calculated Bins corresponding to the sum of the predicted mean values, the 1st grid deviates 5082 W, while the 2nd grid deviates 5216 W, relating to an overall solar load of 21.535 W like shown in table 3.

Table 3: Solar load comparison onto W3 for the rough discretization mesh

coarse discretizations	Bin=1	Bin=2	Bin=10	Bin=26	Bin=46	SUM:	
predicted values:	6885	5926	4570	3026	1127	21535	[W]
values 1st grid:	9064	7164	5728	3277	870	26103	[W]
values 2nd grid:	5126	7449	3423	3509	1431	20938	[W]
dev. 1st grid:	2179	1238	1158	251	257	5082	[W]
dev. 2nd grid:	1759	1523	1147	483	304	5216	[W]

A second simulation with a more refined discretization mesh results different, like shown in figure 33. The new refined discretization is based on a fenestration wall consisting of 450 surfaces for the 1st grid and 420 surfaces for the 2nd grid.

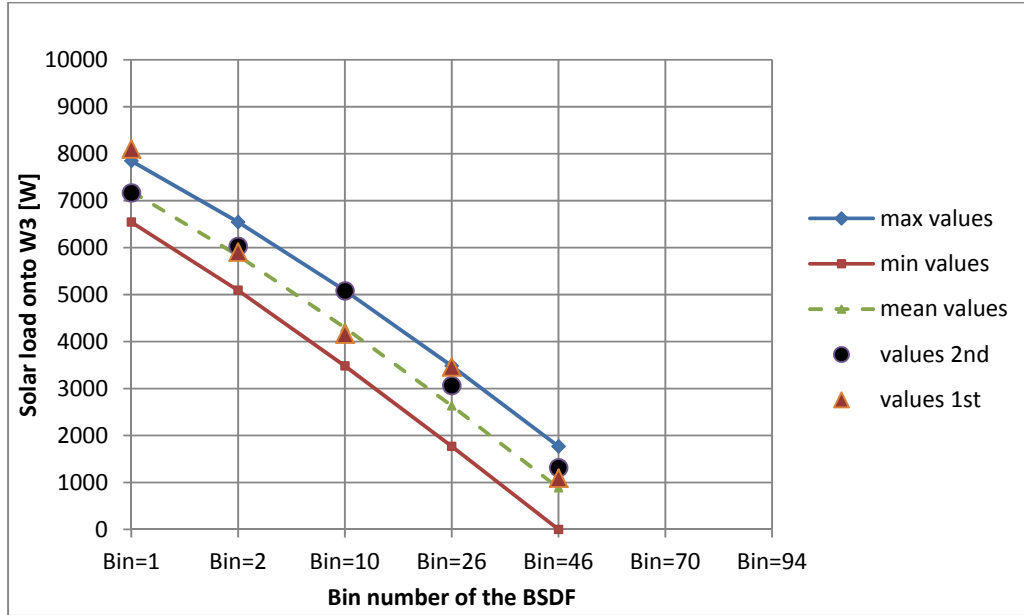


Figure 33: Value comparison for the 1st (20 cm × 20 cm) and 2nd (30 cm × 15 cm) discretization mesh for a refined discretization at 3.0 m room depth

As figure 33 shows, both grids are laying now mostly within the predicted solar load which is an indication for the positive effects of a refined discretization mesh in general. The change however is that the 2nd grid now is the more precise one. Adding up the deviations of the calculated values results for the 1st grid in a deviation of 2117 W, while the 2nd grid has a deviation of 1115 W, relating again to an overall solar load of 21.534 W like shown in table 4.

Table 4: Solar load comparison onto W3 for the refined discretization mesh

refined discretizations	Bin=1	Bin=2	Bin=10	Bin=26	Bin=46	SUM:	
predicted values:	6885	5926	4570	3026	1127	21535	[W]
values 1st grid:	8102	5907	4158	3461	1093	22721	[W]
values 2nd grid:	7167	6028	5078	3064	1312	22649	[W]
dev. 1st grid:	1217	19	412	435	34	2117	[W]
dev. 2nd grid:	282	102	508	38	185	1114	[W]

This means the 1st grid has a deviation percentage of 9.83% corresponding to the mean values, while the 2nd grid with the more equal distances between the surface centroids has a deviation percentage of 5.18%.

Hence this examination shows the attitudes of both different grids, the result is that especially for a more precise refined discretization the 2nd grid provides more accurate simulation values. Consequently the 2nd discretization mesh will be used for both parameter studies in the following chapters. Beneath the awareness of the effects of different kinds of grids, the examination of effects of a refined discretization is important too, to obtain a knowledge how calculation results can be affected through these.

Like usual for numerical simulations, the level of preciseness of the numerical grid has influence on the quality of the simulation results. Especially a coarse discretization often results in numerical instabilities and therefore wrong simulation results. So a refined discretization mostly results in more accurate simulation values, although a more refined discretization on the other side at one point do not improve the simulation results significant anymore, while needing much more simulation time and hardware recourses. Obtaining knowledge about the simulation reaction to varying level of discretization is important for specifying an adequate level of mesh detail during practical applications.

As an examination of these effects on the detailed virtual manikin, caused by the complexity of its structure, is quite difficult to analyze, this examination concentrates on the simulation room without the manikin. Here the effects of the solar radiation through the fenestration facade onto a parallel and rectangular surface can be predicted and analyze more precise. Hence focus lies on the opposite wall W3, representative for a parallel surface, as well as the adjacent wall W2, representative for a rectangular surface. Furthermore, and similar to the grid examination, the examined solar incidence is limited to a horizontal solar beam from Bin 1 till 134 on the outer hemisphere (see figure 30) with the same boundaries for the solar radiation and fenestration properties. Additional the influence of a varying room depth on the simulation results is part of the examination.

Similar to figure 31 the range of predicted solar load onto W3 is based to evaluate the simulation results for three different room depths as there are 1.5 m, 3.0 m, and 6.0 m and varying level of discretization detail from 150 cm × 75 cm for the coarsest discretization till 10 cm × 5 cm for the most detailed one. A comparison of the simulation results is presented in the following figures.

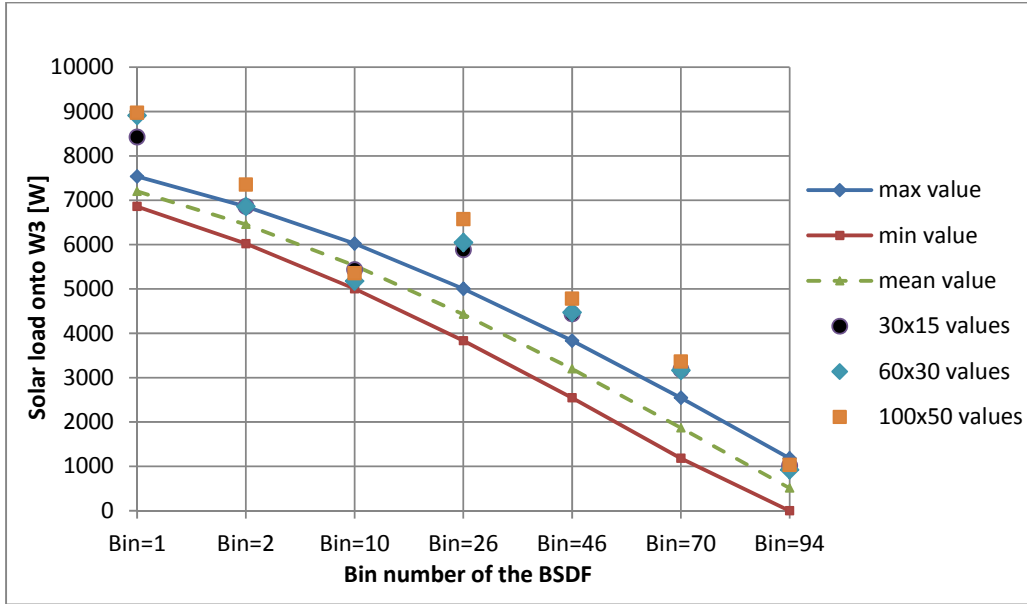


Figure 34: Value comparison for three different fenestration discretization, and a 10 cm × 5 cm discretized W3 at a room depth of 1.5 m

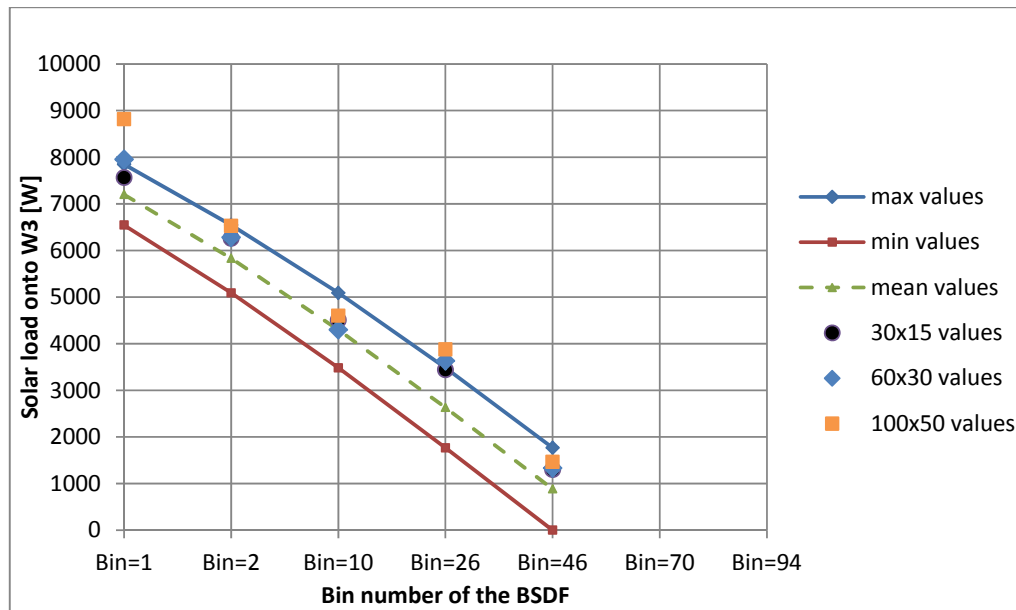


Figure 35: Value comparison for three different fenestration discretization, and a 10 cm × 5 cm discretized W3 at a room depth of 3.0 m

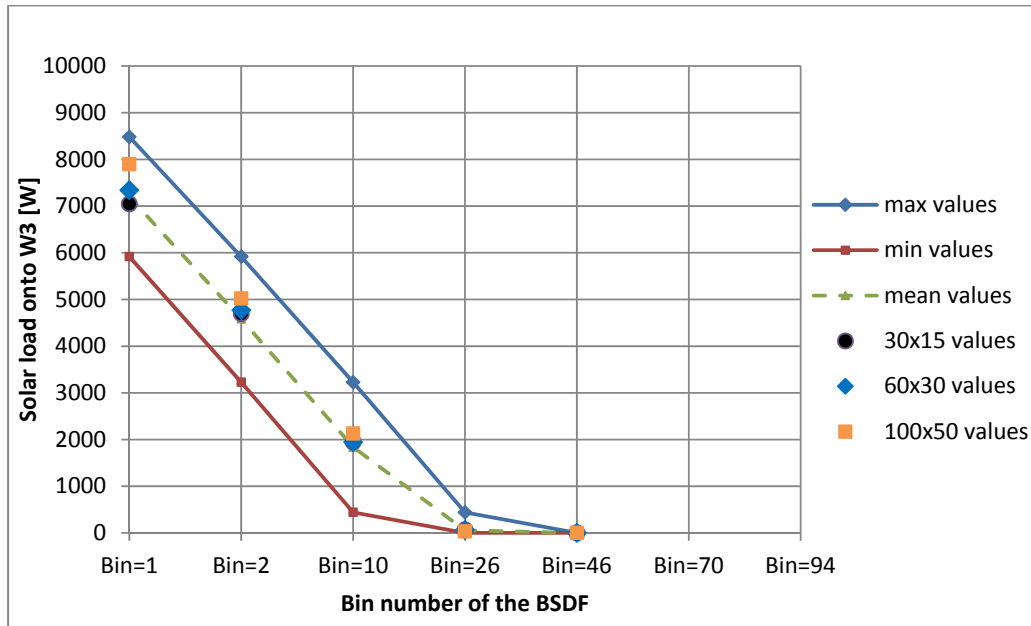


Figure 36: Value comparison for three different fenestration discretization, and a $10\text{ cm} \times 5\text{ cm}$ discretized W3 at a room depth of 6.0 m

As shown in figure 34, 35, and 36, the calculation results are getting more precise for a more refined discretization, independent of the room depth. However the overall results are dependent of the room depth. As shown in the graphs the simulation results are getting more precise with a growing room depth. The cause for the missing values for Bin 70 and 94 in figure 34 and 35 is to be found in the geometry of the simulation room. Depending on the depth of the room, these outer Bins do not match the W3 anymore. Only the 1.5 m deep room is close enough to the fenestration façade, so that these Bins match the wall.

The cause for this depth-dependent behavior is to be found in the viewfactor theory. This theory says that a surface emits into all directions, independent of the surface properties. As figure 37 shows, a rising distance of the corresponding surface F_2 towards the emitting surface F_1 results in less matches of the diffuse beam onto F_2 . As the simplified 2-dimensional calculation of the predicted solar load uses only the solar radiation into the direction of the distance vector between the two surface centroids, an overestimation of the solar load occurs for the simulation with viewfactor. Hence this overestimation becomes smaller for a rising room depth.

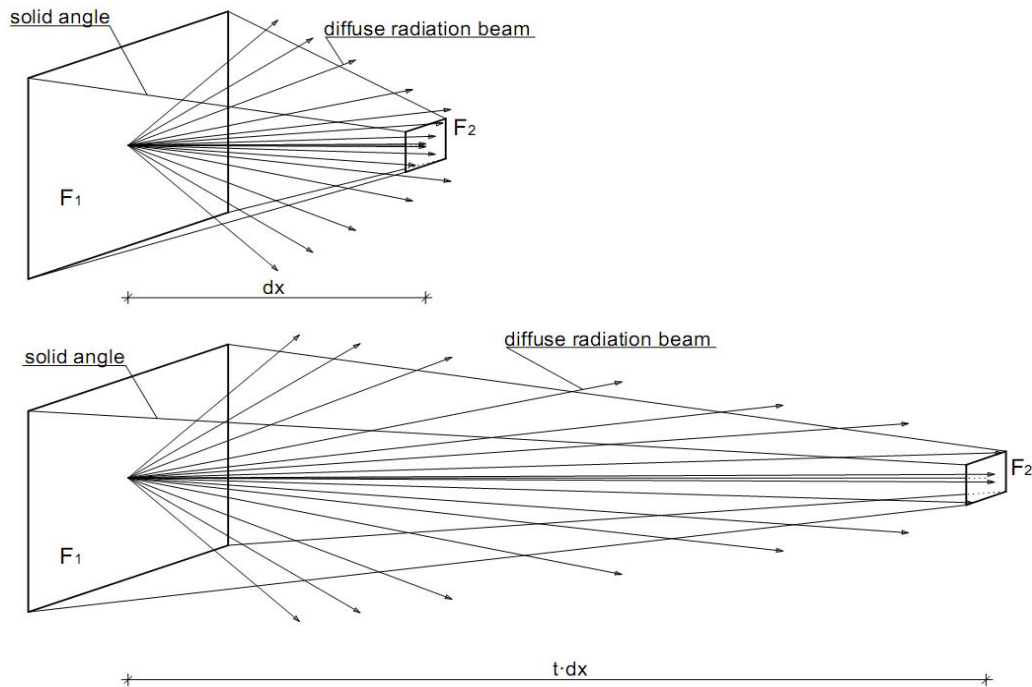


Figure 37: Viewfactor theory for the solar radiation emitted by a surface F_1 towards a surface F_2 with a varying distance between.

Additional this effect is dependent on the size of the surface area F_2 , which can be seen in figure 34 till 37 as well. This follows in the conclusion, that the simulated virtual manikin is, dependent on the level of discretization not that sensitive to the distance between its position and the fenestration façade. So in general it is to consider the distance of the manikin towards the fenestration façade as well as the level of discretization.

As a room depth around 3.0 m is the most representative of these three for a usual depth of an office or living room, this simulation condition is examined further up to a fenestration discretization of 10 cm × 5 cm. The results are compared with the most accurate results of the above described 30 cm × 15 cm discretization in figure 38.

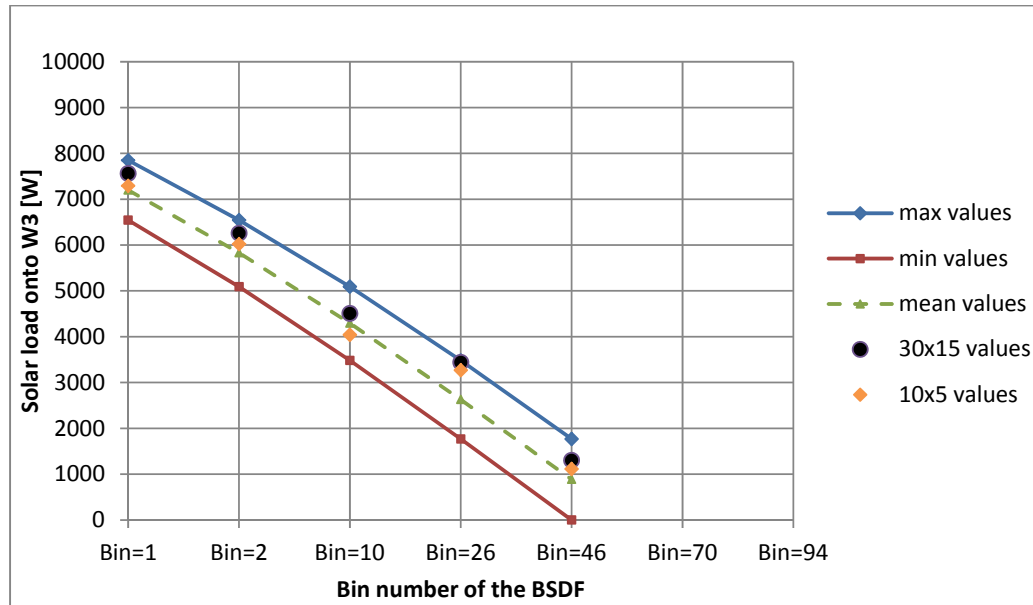


Figure 38: Value comparison for two different fenestration discretization, and a 10 cm × 5 cm discretized W3 at a room depth of 3.0 m

As shown here, an improvement for the refined discretization is indeed existent, but the additional simulation time and the needed hardware recourses become bigger as well. Here it is in a practical application important to estimate if a more refined discretization is still useful, or if the benefits of a shorter simulation time, respectively limited hardware recourses prevail.

Another aspect is the effect of a varying discretization of W3. After the awareness that a rising level of detail for the fenestration discretization results in more accurate simulation values, this aspect is simulated for a fenestration discretization of 75 cm × 37.5 cm, while the W3 discretization changes between 75 cm × 37.5 cm and 20 cm × 10 cm, like shown in figure 39.

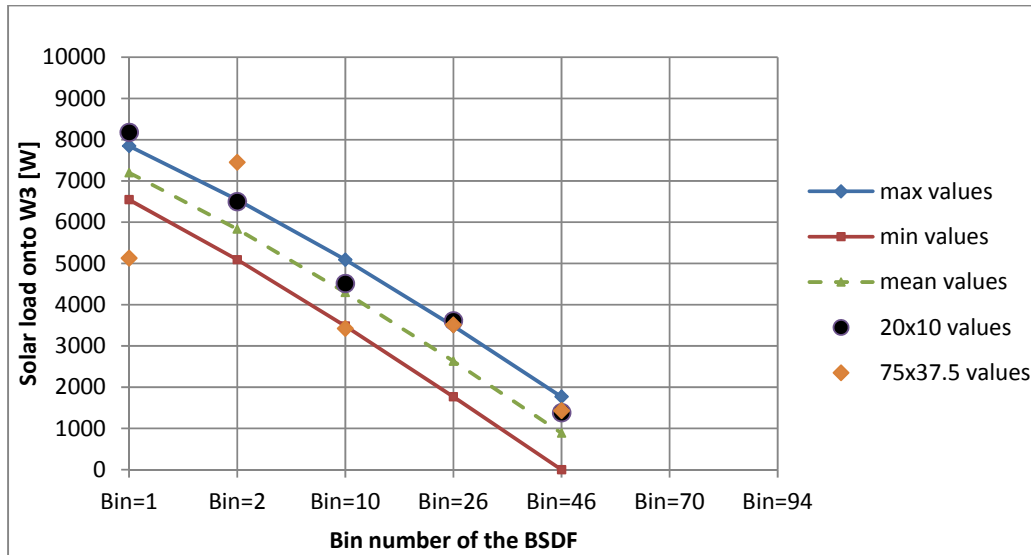


Figure 39: Value comparison for two different W3 discretization and a 75 cm × 37.5 cm discretized fenestration facade at a room depth of 3.0 m

As this examination shows, the level of discretization detail of the other walls has an influence on the simulation results as well. This shows, that a too coarse discretization of the simulation room affects the simulation results with a detailed discretized fenestration facade in a negative way. This whole examination thus stands representative for the virtual manikin, so that it is to assume that the same effects may occur for a coarse discretized manikin.

Beneath the effects of the simulation tool for solar radiation onto a parallel surface, the effects on a rectangular surface have to be examined as well to get a better understanding of the influence of varying simulation properties. Hence the solar radiation onto W2 will be examined as well. Important here is, that the predicted solar load will be calculated different as for W3 which is shown in figure 40.

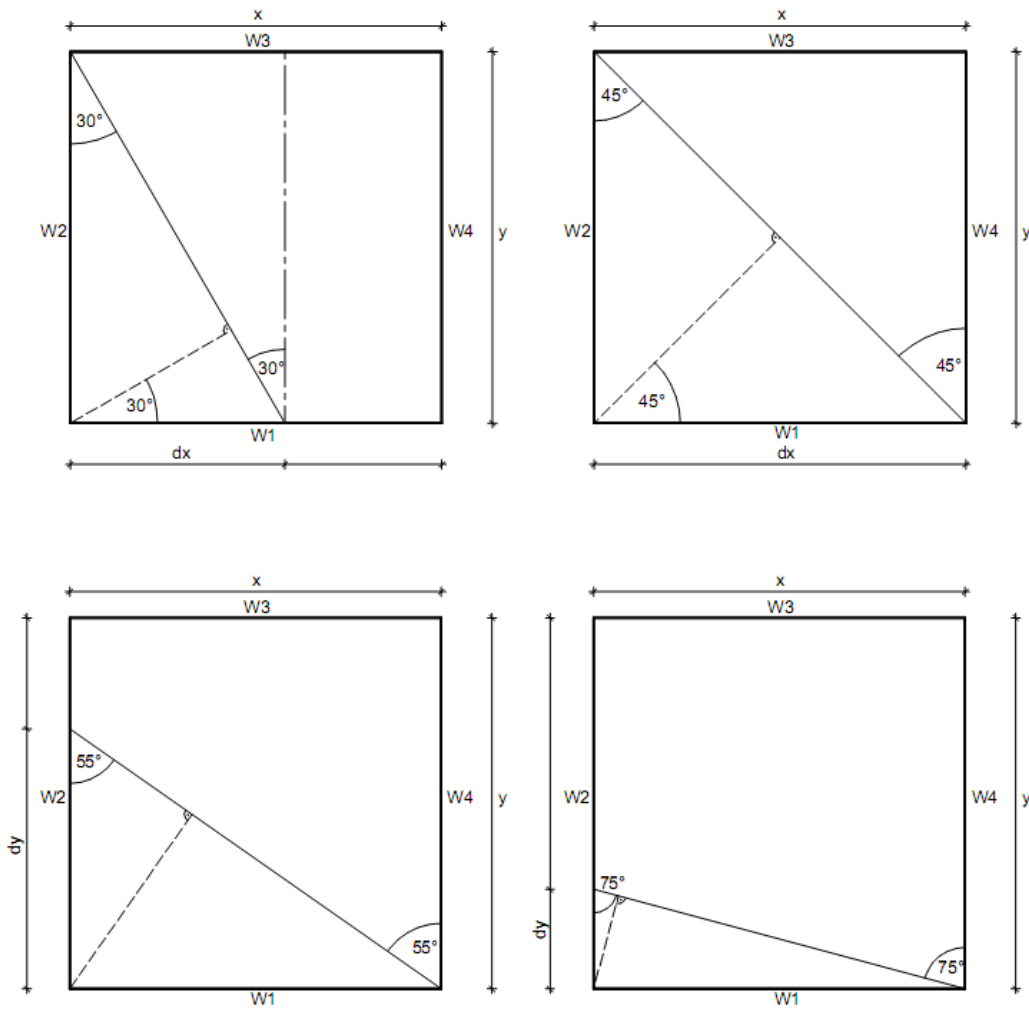


Figure 40: Solar load calculation of the corresponding surface on the left wall W2 for varying spherical angle theta on a 3 m × 3 m simulation room.

As shown here, the calculation of the predicted solar load onto W2 changes when the spherical angle theta rises above 45°. Up to 45° the predicted solar load will be calculated after equation 46, while the calculation for angles above 45° will be made after equation 47. The values dx and dy have to be calculated corresponding to equation 44.

$$\text{Solarload}(0 \leq \theta \leq 45^\circ) = 800W/m^2 \cdot 3m \cdot (d_x \cdot \cos(\theta)) \quad [46]$$

$$\text{Solarload}(45^\circ < \theta \leq 90^\circ) = 800W/m^2 \cdot 3m \cdot (d_y \cdot \cos(90^\circ - \theta)) \quad [47]$$

So after obtaining the predicted solar load onto W2, the examination follows after the same simulation conditions as for W3 before, with the exception, that the solar incidence beam will be simulated for more Bins of the outer hemisphere. Hence the left wall W2 gets solar radiation for a longer time period of the day, the simulated Bins are running from 1 till 134 on the horizontal axis of the hemisphere, as shown in figure 30. The simulation results for the examination of a 10 cm × 5 cm discretized wall W2 and varying discretization for the fenestration façade are shown in figure 41.

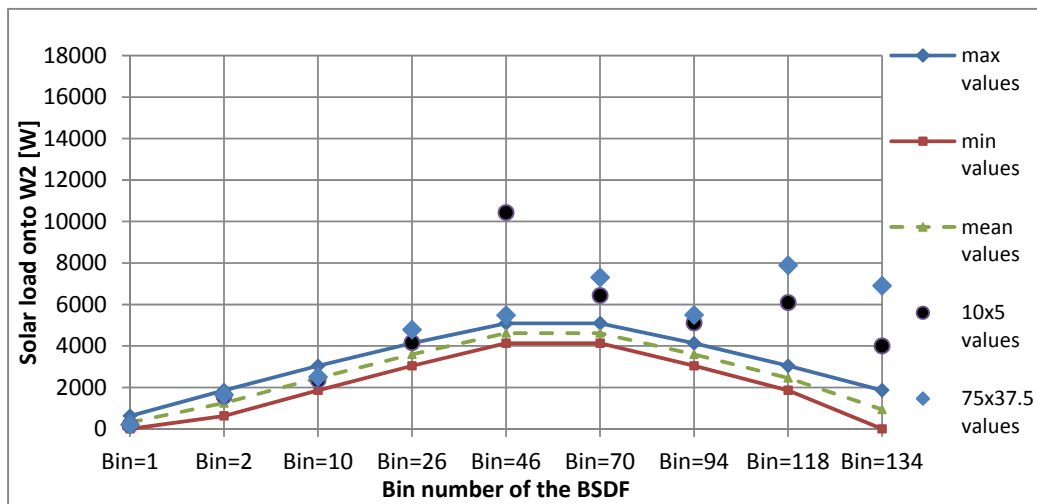


Figure 41: Value comparison for two different fenestration discretizations and a 10 cm × 5 cm discretized W2 at a room depth and width of 3.0 m

As the simulation results are showing, the level of discretization detail here has similar to the W3 examination a positive influence on the preciseness of the results. Outstanding however is the value for the Bin 46 for the 10 cm × 5 cm discretization of the fenestration façade. Detailed simulations provide the same results, especially for similar discretization levels for the fenestration façade and W2, where the deviation for Bin 46 becomes higher for a coarser discretization.

The cause for this high deviation at this particular Bin is to be found in the view factor calculation. Subsurface on the vertical edge at the corner of the fenestration façade and W2 lying so close to each other, that one subsurface of W2 for example sees only a part of the fenestration façade. Hence the adjoining subsurface of the fenestration façade represents the main visible

area for the subsurface of W2. This results in a high view factor for the relation of these two subsurfaces. Usually this particular viewfactor will not be matched during the simulation, caused by the different discretization of the two facades, but for a similar discretization the distance vector for these two subsurfaces lies around 45 degree, and thus will be matched through the Bin 46 and consequently the high viewfactor value comes into effect. By eliminating of these edge subsurfaces, the deviation at Bin 46 becomes notable less, like shown in figure 42.

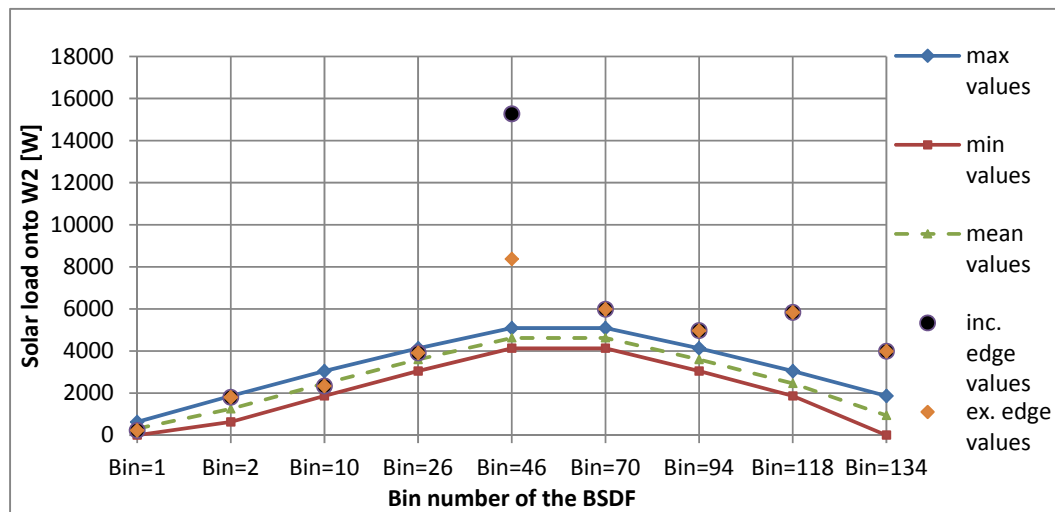


Figure 42: Value comparison for the 20 cm × 10 cm fenestration and W2 discretization with included as well as excluded edge subsurfaces at a room depth and width of 3.0 m

This effect of the view factors only occurs for this particular geometric condition and has no effect for the virtual manikin, which is not positioned that close to the fenestration façade. So the view factors for the subsurfaces of the virtual manikin are not rising to high and result in unrealistic simulation values.

Another point of interest is the overestimation of the following Bins starting with Bin 70, which is a result of an overlaying of the solar loads on the subsurfaces of W2. As figure 43 and 44 show, especially for the outer Bins of the hemisphere the incidence angle of the solar beam gets more tilted. This follows in an overlay of the Bins projection on the subsurfaces of W2 for moving subsurfaces on the fenestration façade, like simplified in figure 43 and 44 for the outer hemisphere Bins 26 and 118.

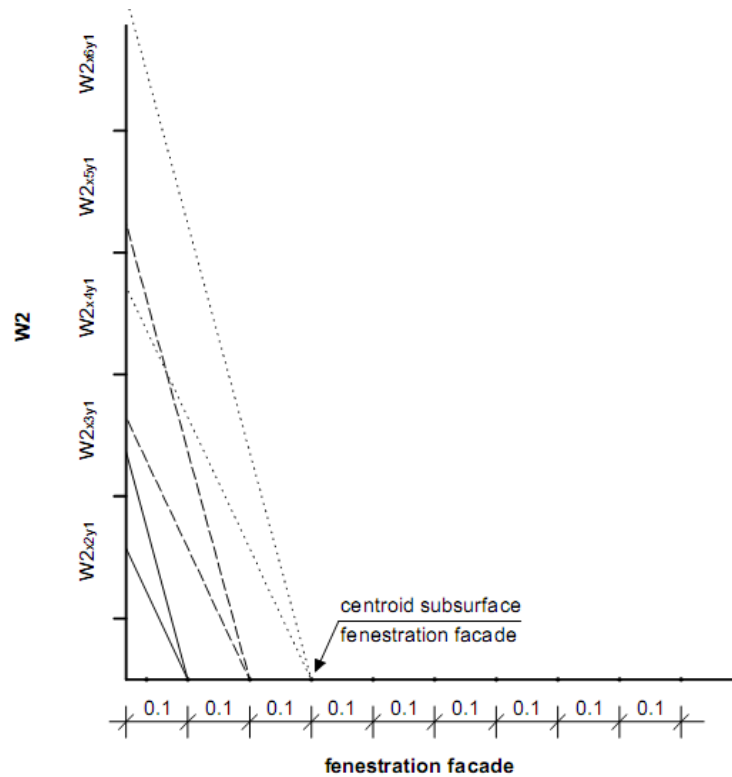


Figure 43: Solar load overlay for Bin 26 ($25^\circ \leq \theta \leq 35^\circ$) of the outer hemisphere and a $20 \text{ cm} \times 10 \text{ cm}$ discretization for the façade and W2.

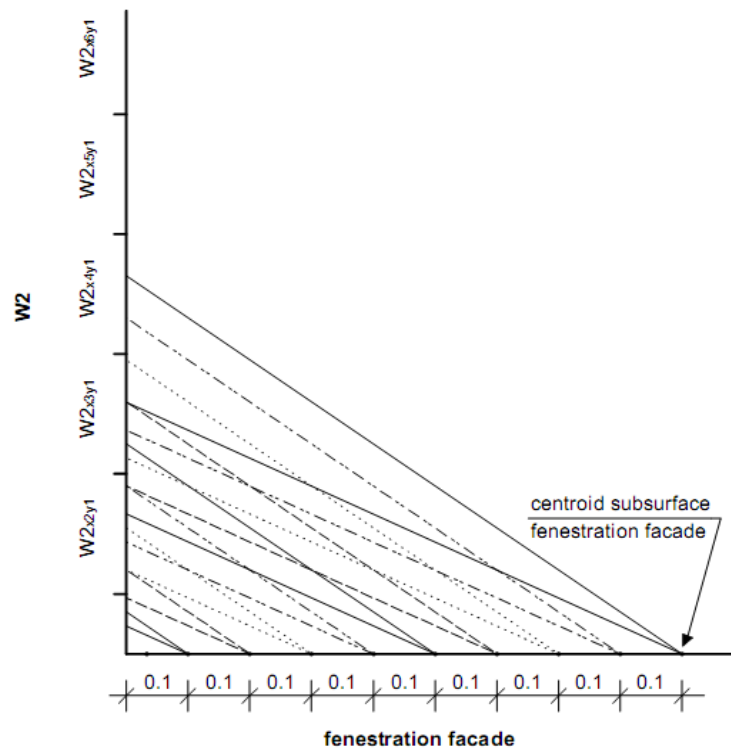


Figure 44: Solar load overlay for Bin 118 ($65^\circ \leq \theta \leq 75^\circ$) of the outer hemisphere and a $20 \text{ cm} \times 10 \text{ cm}$ discretization for the façade and W2.

As seen in these figures, the overlay of the solar beam on the subsurfaces of W2 are notable more for Bins in the outer rings of the hemisphere, which explain the higher deviation of the simulation results for the outer Bins. One subsurface on W2 gets solar radiation from several subsurfaces of the fenestration façade. Hence smaller subsurfaces on the fenestration façade as well as taller subsurfaces on W2 increase this deviation. With the obtained awareness of the effects of varying grids and levels of discretization an appropriate interpretation of practical simulation results is possible. The practical application of this calculation tool is described in more detail in chapter 4.

4. Case study of the solar load onto occupants for two buildings with shading devices

As a practical application of the developed tool, two buildings in the United States will be examined. The first is the Helios building in Berkeley, California and the second a Hospital in Denver, Colorado. The simulation results for both parameter studies are analyzed after several criteria. The main question for the two buildings is, whether the shading devices have an effect in general or not, and if, how these effects influence the solar load on occupants within the building. Hence the main focus lies on this point. In addition it is interesting to see, how the shading devices influence the solar load on a day with clear sky and how on a cloudy day.

4.1. Case study for the simulation of the Helios building in Berkeley, California

The Helios building in Berkeley is a new constructed research facility of the University of California Berkeley. It is located at the corner of Hearst and Oxford Street at the south end of the university campus like shown in figure 45. The about 120,000 sq ft comprising building shall be equipped with specialized analytical research laboratories and offices for research on basic scientific problems in the production of carbon-neutral fuels, as well as synthetic and computational biology, which is pursued in the bioengineering program of the University (University of California Berkeley (2009), p.1).

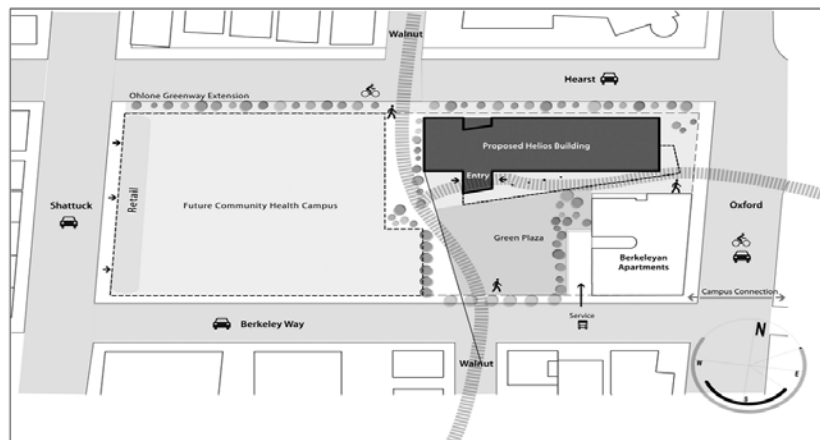


Figure 45: Location of the Helios building at 2151 Berkeley Way at Shattuck, University of California Berkeley (2009, p.2)

The office rooms of the Helios building are orientated south side to use the daylight, while a horizontal bladed sunshade is installed on the south façade to reduce glare and heat gain. The structure of the south façade is shown in more detail in Annex 7. Examining the effects of this shading device on the solar load onto occupants in the office rooms is content of this parameter study.

The simulated virtual room, as shown in figure 46 has the dimensions of 3.0 m width, 3.0 m depth, and 2.7 m height, as well as a shading device, consisting of two horizontal bladed sunshades, with 60 and 90cm depth and a solar transmission of 30%. The simulated manikin represents a seating occupant, positioned facing to west in the middle of the room, with a distance of 90 cm towards the fenestration façade. The glass façade, as shown in figure 47, is divided into a translucent part for the lower 80 cm and upper 30 cm, as well as a transparent part for the remaining 160 cm in the middle.

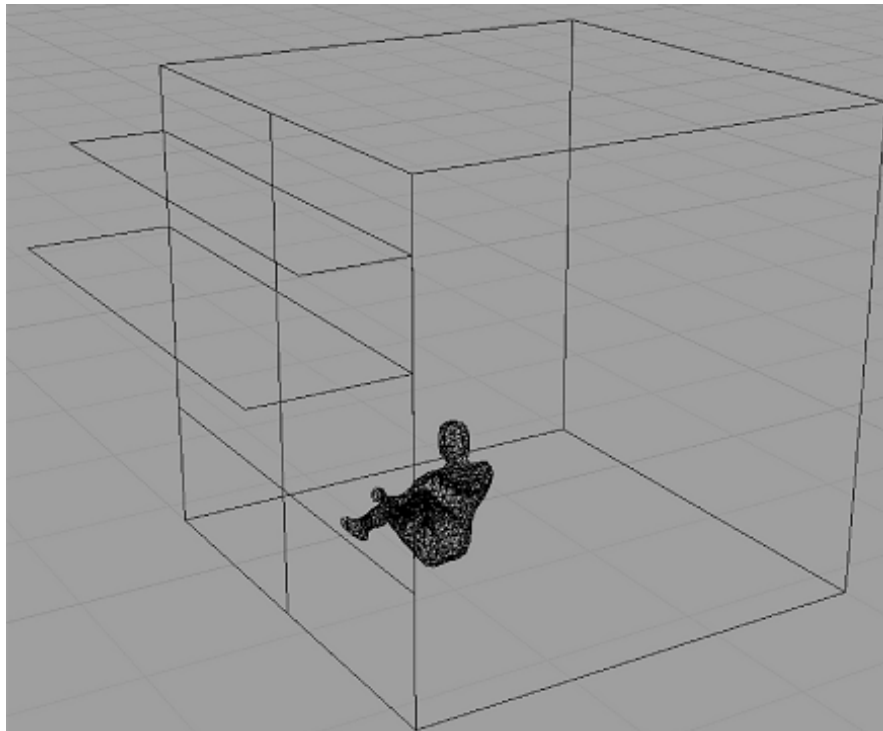


Figure 46: Rhinoceros presentation of the virtual testing room for the Helios building examination

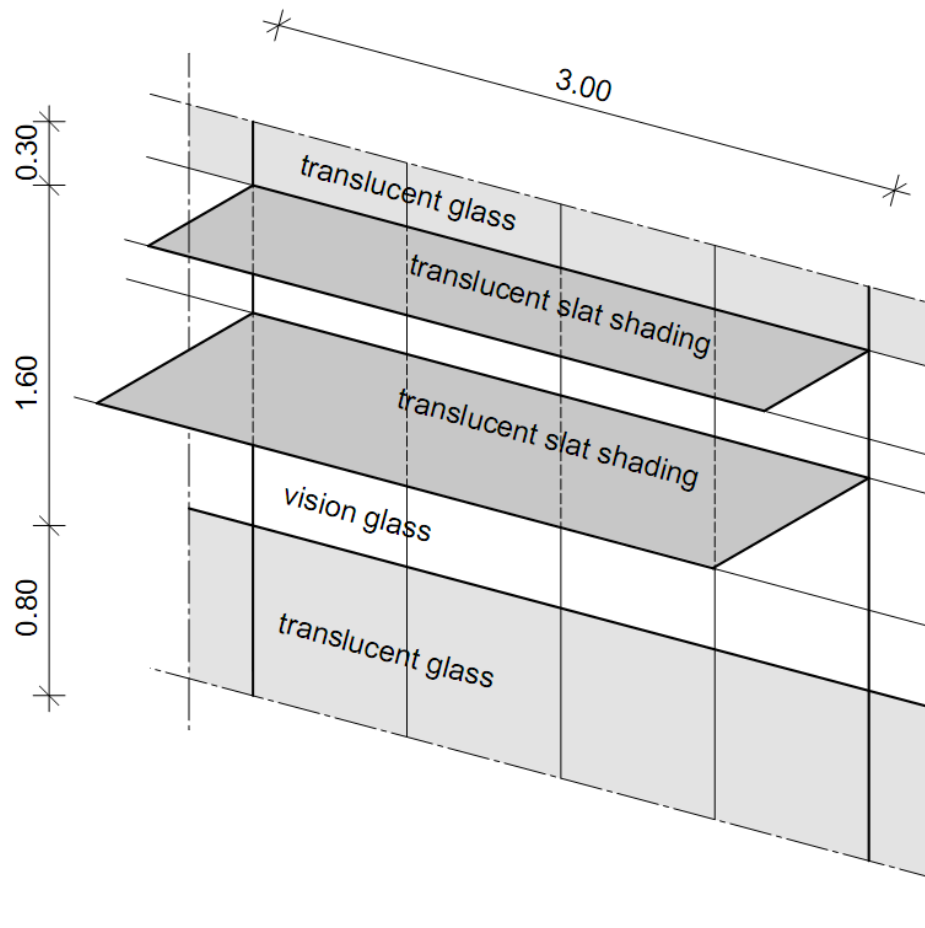


Figure 47: Structure of the façade of the Helios building in Berkeley with division into translucent and transparent (vision) glass areas.

The boundary conditions for the solar load simulation are obtained from different sources. The major input parameters for the calculation tool thus are the Bin numbers on the outer hemisphere, representing the incidence angle of the solar beam, and the amount of the solar radiation for a given day time. The solar radiation on the one hand can be obtained from weather datasets, while the Bin numbers on the other hand are calculated with the developed calculation tool by determining the latitude and longitude of the building as well as the examined day of the year. With these input parameters the solar incidence angle with the corresponding Bin on the outer hemisphere can be calculated for every orientation of the building facades and any daytime, as shown in figure 48.

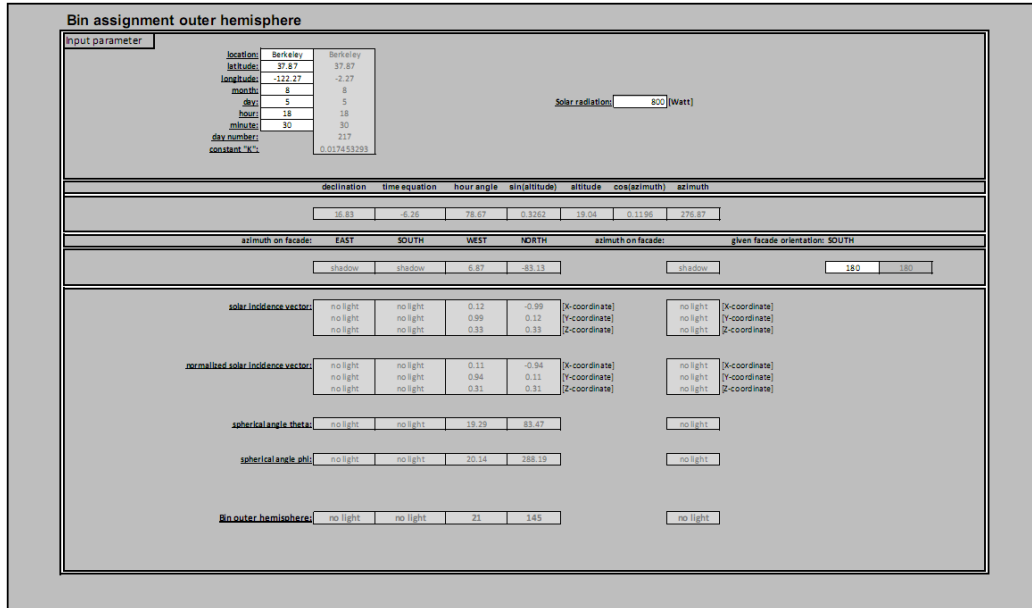


Figure 48: Bin calculation for the Helios building using the developed calculation tool.

In order of this examination, a design day will be used instead of a regular day out of the weather dataset. As the south façade will be examined, the simulation will be executed for the day time with solar radiation for clear sky conditions on this façade from 9 AM till 6 PM in hourly steps. Additionally the effects of a cloudy day with only diffuse radiation will be simulated. Hence the solar radiation conditions are chosen as shown in table 5.

Table 5: Hourly direct and diffuse solar radiation for a design day, used for the examination of the Helios shading device.

daytime	clear sky conditions		cloudy sky conditions
	direct solar radiation [W/m ²]	diffuse solar radiation [W/m ²]	diffuse solar radiation [W/m ²]
9:00	257	141	138
10:00	597	146	189
11:00	766	155	271
12:00	827	158	319
13:00	850	166	386
14:00	855	175	427
15:00	850	166	386
16:00	827	158	319
17:00	766	155	271
18:00	597	146	189

The simulation of the design day will be executed for the fenestration device including, as well as excluding the influence of the shading device, and additional for a simple clearglass window. The fenestration device thus consists of a double layer glass façade with a solar coating on the inner surface of the outer glass layer and a 12 mm air gap between the two layers. This construction has a solar transmittance of 26%, while the additional examined two layered clearglass façade has a solar transmittance of 61%. The three different BSDF matrices thus will be obtained by Window6 as described in previous chapters.

Considering to the simulated daytime, the shaded area of the glazing façade will be calculated and the appropriate part of the fenestration area from the simulation with included sunshade combined with the remaining area from the simulation without sunshade. If, for example, the upper 40 cm of the façade at a given daytime are lying in shadow, the values from these upper 40 cm for the solar load with included sunshade will be combined with the values of the remaining 2.3 m for the solar load without sunshade. This combination allows a most precise solar load calculation for any fenestration construction. However, the examination of the slat shading showed, that the transparent glass area lies over the whole simulation time in shadow, so that in this case no combination of shadowed, and not shadowed façade parts was necessary.

As described before, the main question here was, if the shading device has an effect in general on the solar load off occupants. Hence the first examination was to compare the solar load results for the façade with shading and without. In addition the simulation results for a simple clearglass façade are included to compare the effects of the building façade in general. The results are shown in figure 49.

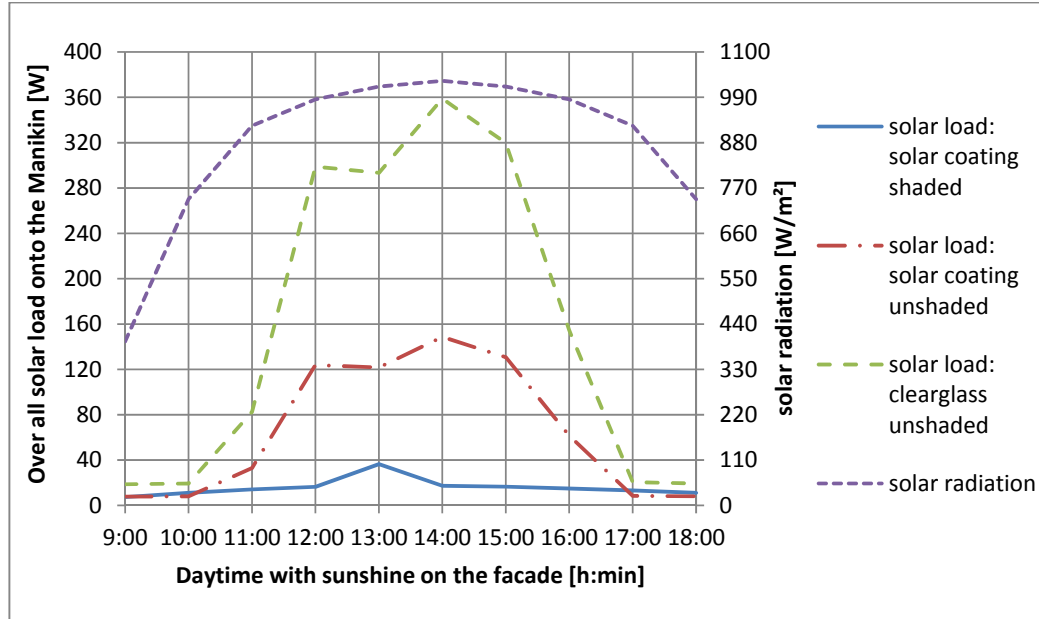


Figure 49: Comparison of the solar load onto the Manikin for clear sky conditions, south-façade Helios building, Berkeley.

This figure shows that the installed slat shading has indeed an effect on the solar load. The glass façade without shading has a curve, quiet similar to the one with a clearglass façade. The lower amplitude is caused by the lower solar transmittance of the constructed glass façade with the solar coating. The solar load with included slat-shading however shows a different curve. The effects of the solar radiation over the day are quiet less than without shading. Only within the two hours from 12 PM to 2 PM the solar load rises, what is caused on the one hand by the bigger amount of solar radiation during that time, and on the other hand by the higher tilt of the incidence angle of the solar beam. The lower the tilt of the incidence angle, the higher is the solar absorbance of the glass material.

As figure 49 shows the combination of the direct and diffuse solar radiation, so consider figure 50 and 51 both separately. Hence it is to see, that the part of direct radiation has the main effect on the manikin. The influence of the diffuse radiation, especially during the midday hours, is rather less important, but becomes bigger for the hours in the early morning and late afternoon, where the direct solar radiation on the manikin is very low. Furthermore the response of the Manikins solar load to the diffuse solar radiation is more consistent than to the direct radiation.

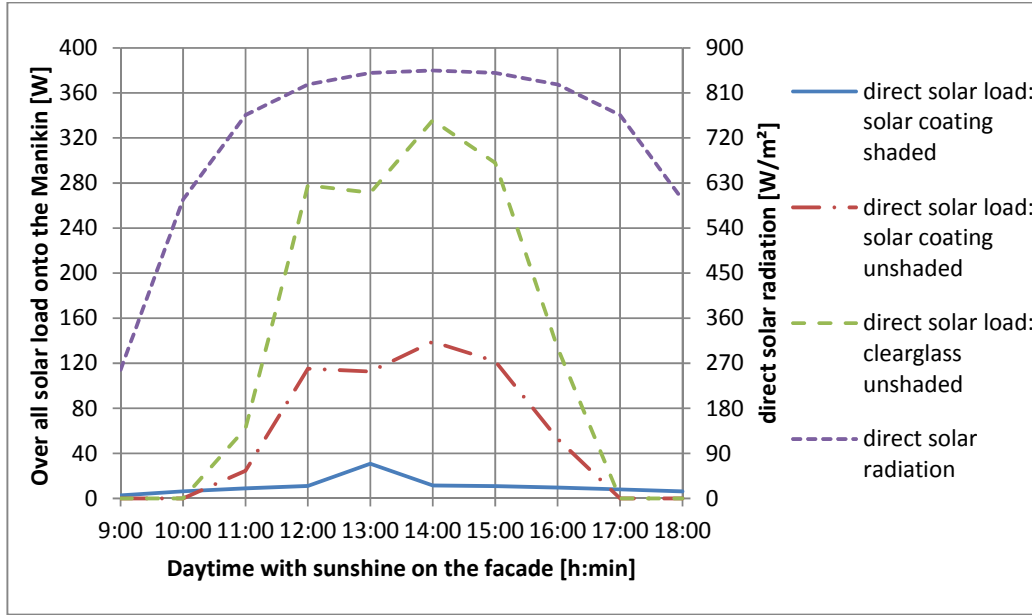


Figure 50: Comparison of the direct solar load onto the Manikin for clear sky conditions, south-façade Helios building, Berkeley.

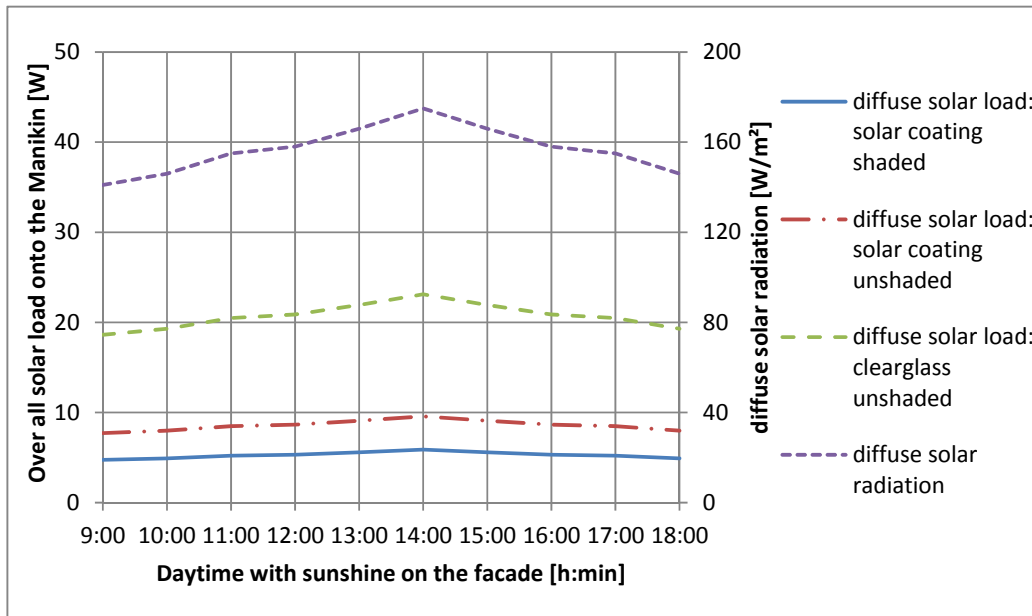


Figure 51: Comparison of the diffuse solar load onto the Manikin for clear sky conditions, south-façade Helios building, Berkeley.

As these graphs represent the effects of the different facades for the solar radiation under clear sky conditions, figure 52 shows the effects under cloudy sky conditions, where the direct solar radiation is zero and there is only diffuse radiation.

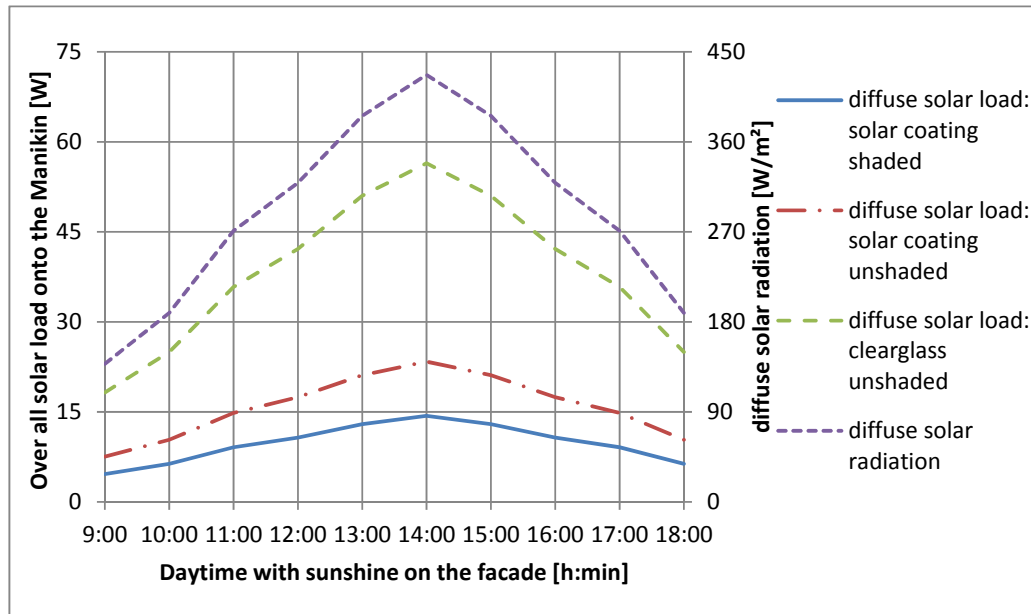


Figure 52: Comparison of the diffuse solar load onto the Manikin for cloudy sky conditions, south-façade Helios building, Berkeley.

Comparable to the effects of the solar load for clear sky condition in figure 51, the response of the solar load for the diffuse radiation is more similar than in figure 50 for the direct solar radiation. Only the amplitude of the solar load is bigger, which is caused by the higher diffuse radiation on a cloudy day. The origin for this different reaction is to be found in the incidence of the solar radiation onto the outer hemisphere. As the direct solar radiation for a given day time matches only one Bin on the outer hemisphere and is transmitted appropriate to the BSDF into the room, the diffuse radiation matches all Bins of the outer hemisphere. Hence the transmittance into the room and onto the Manikin is distributed more equally.

So this examination shows that the installed shading device on the south-façade of the Helios building has indeed an effect on the solar load onto occupants. Especially for a clear day with a high direct solar radiation, the

slat shading reduces the solar load of the Manikin significant. Also important is the reducing of peaks in the solar load, as shown in figure 49. The solar load for the shaded façade is much more equal over the day, independent of direct, diffuse or combined solar radiation. As the solar load onto the Manikin is a main parameter for the comfort feeling, peaks may result quickly in loss of thermal comfort.

Hence the final result of this examination is that the shading device represents indeed an improvement for the façade construction. It is an effective way to realize the benefits of a complete glass façade, as for example bright office rooms and usage of daylight instead of artificial light, without the disadvantages, as for instance high solar load into the building and onto the occupants, what results probably in a higher energy consumption for air conditioning, or a rising thermal discomfort of occupants.

4.2. Case study for the simulation of a Hospital in Denver, Colorado

As the Hospital in Denver is an ongoing project, the description of the building is reduced on the simulation parameter like fenestration and shading properties and solar radiation values. Depended on the geometry of the building, or the Hospital rooms, the virtual testing room has the dimensions of 1.5 m width, 3.0 m depth and 2.7 m height, with a horizontal bladed sunshade of 61 cm length and a solar transmission of zero, as shown in figure 53.

The façade itself thus is divided into an opaque part for the lower 80 cm, and a transparent part for the remaining 190 cm as shown in figure 54. For the south façade, the virtual manikin is, similar to the Helios simulation, positioned facing to west in the middle of the testing room with a distance of 90 cm from the manikin axis towards the fenestration façade. For the west façade, the manikin is rotated 180 degree, so that it is facing to south, which represents the more critical case for solar load onto the occupant. As the solar radiation here affects the north side of the room more than the south side, the solar load onto the manikin is higher for this position.

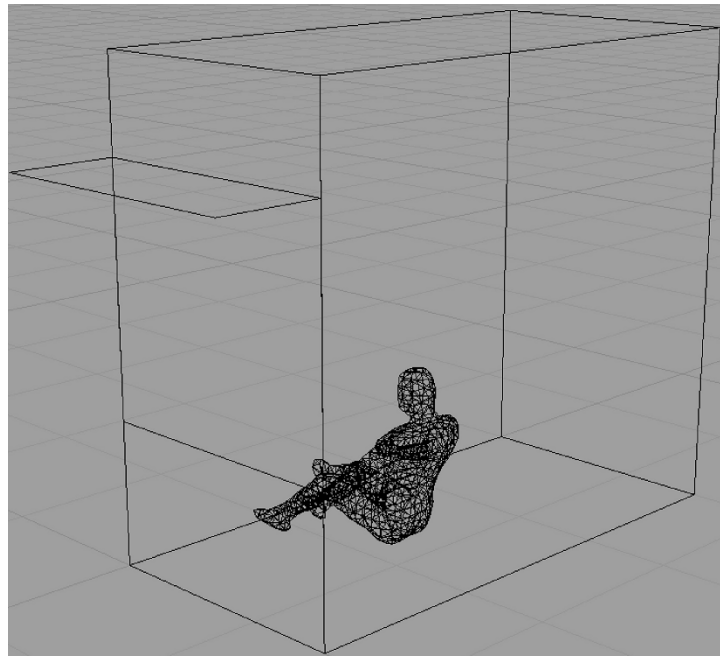


Figure 53: Rhinoceros presentation of the virtual testing room for the Hospital in Denver

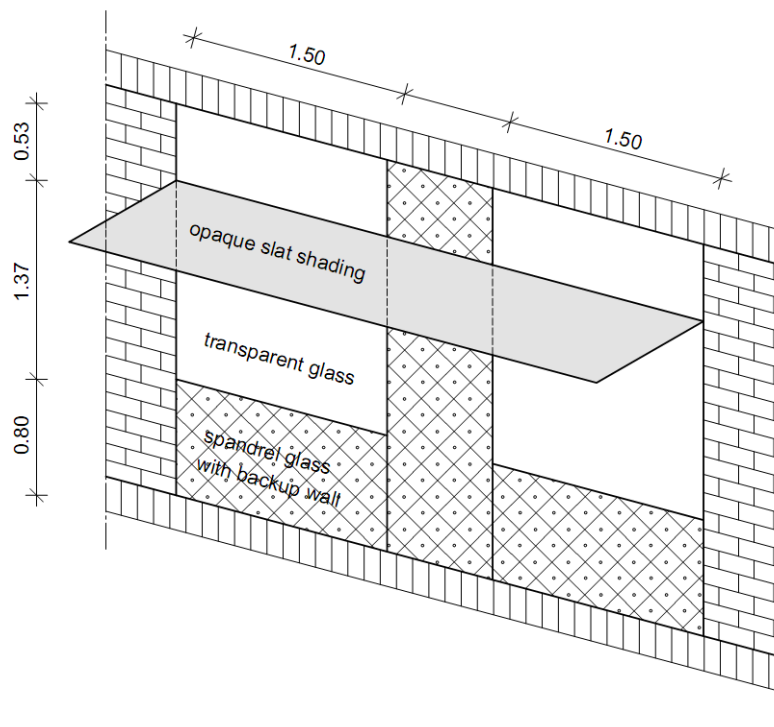


Figure 54: Structure of the façade of the Hospital in Denver with division into opaque and transparent (vision) glass areas

This test room will be examined for the south façade as well as the west façade. This results in a simulation for almost a whole day. So the south façade has to be examined from 9:30 AM till 6:30PM and the west façade from 2:30PM till 7:30 PM. Similar to the Helios simulation a design day is chosen for the weather conditions. Hence the solar radiation is chosen as shown in table 6 and 7. As for the previous simulation, the solar radiation is divided into direct and diffuse radiation, to simulate and analyze the influence of direct and diffuse radiation on the occupant for clear sky and cloudy sky conditions.

Table 6: Hourly direct and diffuse solar radiation for a design day, used for the examination of the south façade of the Hospital in Denver.

daytime	clear sky conditions		cloudy sky conditions
	direct solar radiation [W/m ²]	diffuse solar radiation [W/m ²]	diffuse solar radiation [W/m ²]
9:30	577	121	138
10:30	861	126	189
11:30	985	135	271
12:30	984	138	319
13:30	976	146	386
14:30	958	155	427
15:30	926	146	386
16:30	789	138	319
17:30	773	135	271
18:30	556	126	189

Table 7: Hourly direct and diffuse solar radiation for a design day, used for the examination of the west façade of the Hospital in Denver.

daytime	clear sky conditions		cloudy sky conditions
	direct solar radiation [W/m ²]	diffuse solar radiation [W/m ²]	diffuse solar radiation [W/m ²]
14:30	976	155	427
15:30	958	146	386
16:30	926	138	319
17:30	789	135	271
18:30	773	126	189
19:30	556	121	138

As for the Helios examination, the Hospital will be simulated for a shaded and unshaded window with a solar coating, and a simple clearglass façade. The fenestration device thus consists of a double layer glass façade with a solar coating on the inner surface of the outer glass layer, and a 13 mm air gap between both layers. The calculation of this fenestration device with Window6 results in a solar transmittance of 28%. The clearglass façade is chosen similar to the Helios examination with a solar transmittance of 61%. The three different BSDF matrices thereby will be obtained by Window6 as described in previous chapters.

As described in the previous chapter, the solar load for the shaded façade is a combination of the window area that lies in shadow, and the remaining area that does not lie in shadow. The shading device on the south façade thus puts almost the whole window area into shadow, which is caused by the higher altitude of the sun during that time of the day. Unlike for the south façade, the shading device on the west façade has a minor effect, especially during the hours in the late afternoon. This is caused by the lower altitude of the sun towards the evening. The determination of the solar load of the shaded area is shown in figure 55 for the south façade at 2:30 PM, and in figure 56 for the west façade at 5:30 PM.

height/bodypart	head	chest	back	pelvis	leftupperarm	rightupperarm	leftlowerarm	rightlowerarm	lefthand	righthand	lefthigh	righthigh	leftleg	rightleg	leftfoot	rightfoot
260 - 270 [cm]	0.0	0.0	0.0	0.0	0.0	0.0	0.0	0.0	0.0	0.0	0.0	0.0	0.0	0.0	0.0	0.0
250 - 260 [cm]	0.0	0.0	0.0	0.0	0.0	0.0	0.0	0.0	0.0	0.0	0.0	0.0	0.0	0.0	0.0	0.0
240 - 250 [cm]	0.0	0.0	0.0	0.0	0.0	0.0	0.0	0.0	0.0	0.0	0.0	0.0	0.0	0.0	0.0	0.0
230 - 240 [cm]	0.0	0.0	0.0	0.0	0.0	0.0	0.0	0.0	0.0	0.0	0.0	0.0	0.0	0.0	0.0	0.0
220 - 230 [cm]	0.0	0.0	0.0	0.0	0.0	0.0	0.0	0.0	0.0	0.0	0.0	0.0	0.0	0.0	0.0	0.0
210 - 220 [cm]	0.0	0.0	0.0	0.0	0.0	0.0	0.0	0.0	0.0	0.0	0.0	0.0	0.0	0.0	0.0	0.0
200 - 210 [cm]	0.1	0.0	0.0	0.0	0.0	0.0	0.0	0.0	0.0	0.0	0.0	0.0	0.0	0.0	0.0	0.0
190 - 200 [cm]	0.4	0.0	0.0	0.0	0.0	0.0	0.0	0.0	0.0	0.0	0.0	0.0	0.0	0.0	0.0	0.0
180 - 190 [cm]	0.7	0.0	0.0	0.0	0.0	0.0	0.0	0.0	0.0	0.0	0.0	0.0	0.0	0.0	0.0	0.0
170 - 180 [cm]	1.0	0.1	0.0	0.0	0.0	0.1	0.0	0.0	0.1	0.0	0.0	0.0	0.0	0.0	0.0	0.0
160 - 170 [cm]	0.8	0.4	0.1	0.0	0.0	0.2	0.0	0.3	0.0	0.1	0.0	0.0	0.0	0.0	0.0	0.0
150 - 160 [cm]	0.3	0.8	0.2	0.0	0.1	0.2	0.0	0.4	0.0	0.2	0.0	0.0	0.0	0.0	0.0	0.0
140 - 150 [cm]	0.1	0.9	0.2	0.1	0.4	0.1	0.0	0.4	0.0	0.2	0.0	0.2	0.0	0.0	0.0	0.0
130 - 140 [cm]	0.0	0.5	0.3	0.2	0.7	0.0	0.0	0.2	0.0	0.1	0.0	0.7	0.0	0.3	0.0	0.0
120 - 130 [cm]	0.0	0.2	0.3	0.3	0.6	0.0	0.3	0.0	0.1	0.0	0.1	1.0	0.0	0.6	0.0	0.0
110 - 120 [cm]	0.0	0.0	0.1	0.7	0.4	0.0	0.6	0.0	0.3	0.0	0.5	0.8	0.1	0.8	0.0	0.0
100 - 110 [cm]	0.0	0.0	0.0	1.2	0.0	0.0	0.3	0.0	0.2	0.0	1.2	0.1	0.6	0.6	0.0	0.1
90 - 100 [cm]	0.0	0.0	0.0	0.9	0.0	0.0	0.0	0.0	0.0	0.0	0.9	0.0	0.9	0.3	0.0	0.1
80 - 90 [cm]	0.1	0.0	0.0	0.4	0.0	0.0	0.0	0.0	0.0	0.0	0.3	0.0	0.8	0.0	0.1	0.1

Figure 55: Determination of the solar load for the shaded area of the window, south-façade at 2:30 PM.

height/bodypart	head	chest	back	pelvis	leftupperarm	rightupperarm	leftlowerarm	rightlowerarm	lefthand	righthand	lefthigh	rightthigh	leftleg	rightleg	leftfoot	rightfoot
260 - 270 [cm]	0.0	0.0	0.0	0.0	0.0	0.0	0.0	0.0	0.0	0.0	0.0	0.0	0.0	0.0	0.0	0.0
250 - 260 [cm]	0.0	0.0	0.0	0.0	0.0	0.0	0.0	0.0	0.0	0.0	0.0	0.0	0.0	0.0	0.0	0.0
240 - 250 [cm]	0.0	0.0	0.0	0.0	0.0	0.0	0.0	0.0	0.0	0.0	0.0	0.0	0.0	0.0	0.0	0.0
230 - 240 [cm]	0.0	0.0	0.0	0.0	0.0	0.0	0.0	0.0	0.0	0.0	0.0	0.0	0.0	0.0	0.0	0.0
220 - 230 [cm]	0.0	0.0	0.0	0.0	0.0	0.0	0.0	0.0	0.0	0.0	0.0	0.0	0.0	0.0	0.0	0.0
210 - 220 [cm]	0.0	0.0	0.0	0.0	0.0	0.0	0.0	0.0	0.0	0.0	0.0	0.0	0.0	0.0	0.0	0.0
200 - 210 [cm]	0.0	0.0	0.0	0.0	0.0	0.0	0.0	0.0	0.0	0.0	0.0	0.0	0.0	0.0	0.0	0.0
190 - 200 [cm]	0.0	0.0	0.0	0.0	0.0	0.0	0.0	0.0	0.0	0.0	0.0	0.0	0.0	0.0	0.0	0.0
180 - 190 [cm]	0.0	0.0	0.0	0.0	0.0	0.0	0.0	0.0	0.0	0.0	0.0	0.0	0.0	0.0	0.0	0.0
170 - 180 [cm]	0.0	0.0	0.0	0.0	0.0	0.0	0.0	0.0	0.0	0.0	0.0	0.0	0.0	0.0	0.0	0.0
160 - 170 [cm]	0.7	0.0	0.0	0.0	0.0	0.0	0.0	0.0	0.0	0.0	0.0	0.0	0.0	0.0	0.0	0.0
150 - 160 [cm]	1.6	0.0	0.0	0.0	0.0	0.0	0.0	0.0	0.0	0.0	0.0	0.0	0.0	0.0	0.0	0.0
140 - 150 [cm]	2.0	0.2	0.0	0.0	0.1	0.0	0.0	0.0	0.0	0.0	0.0	0.0	0.0	0.0	0.0	0.0
130 - 140 [cm]	1.1	1.3	0.2	0.0	0.4	0.0	0.5	0.0	0.2	0.0	0.0	0.0	0.0	0.0	0.0	0.0
120 - 130 [cm]	0.1	2.1	0.3	0.0	0.4	0.5	0.9	0.0	0.5	0.0	0.0	0.0	0.0	0.0	0.0	0.0
110 - 120 [cm]	0.0	1.1	0.4	0.1	0.1	1.6	0.7	0.0	0.4	0.0	0.1	0.0	0.0	0.0	0.0	0.0
100 - 110 [cm]	0.0	0.4	0.4	0.3	0.0	1.5	0.0	0.2	0.1	0.0	1.4	0.0	0.4	0.0	0.0	0.0
90 - 100 [cm]	0.0	0.2	0.2	1.1	0.0	0.5	0.0	1.5	0.0	0.7	1.3	0.6	1.2	0.2	0.0	0.0
80 - 90 [cm]	0.0	0.0	0.0	2.2	0.0	0.0	0.0	0.4	0.0	0.4	0.1	2.9	1.8	0.8	0.1	0.0

Figure 56: Determination of the solar load for the shaded area of the window, west-façade at 5:30 PM.

The shaded window area on the west façade for example goes from 190 cm to 270 cm height, which is marked here through the frame. Hence, the framed solar load values are combined with the remaining values of the not shaded window from 80 cm to 190 cm height to obtain the solar load onto the Manikin for the whole window.

The results of the examination of the different façades are shown in the following. Similar to the examination of the Helios building, the effects of the shading device are the most interesting point. Figure 57 and 58 show the comparison of the three different facades for the south and the west façade for clear sky conditions.

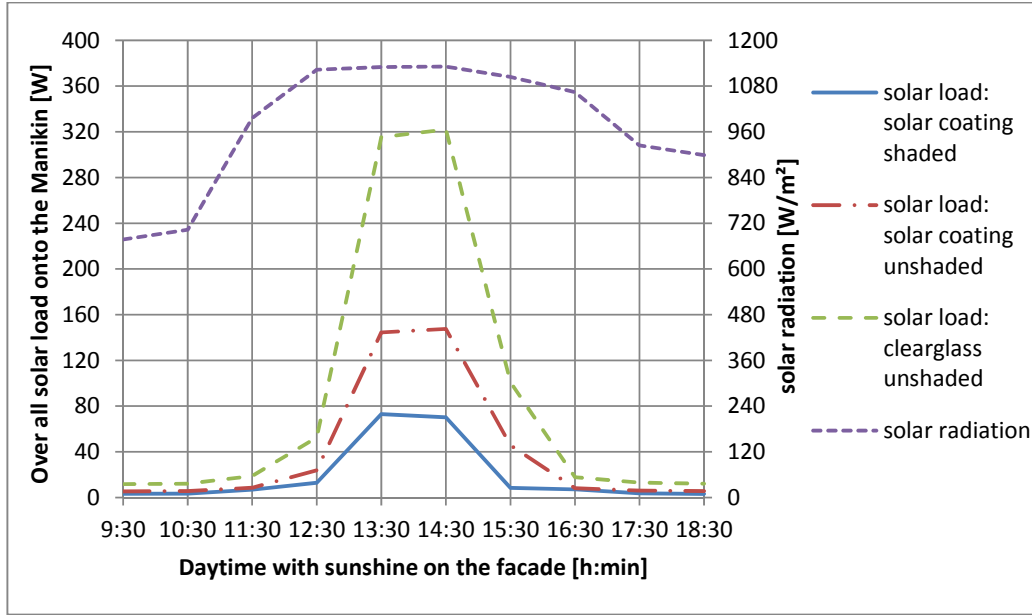


Figure 57: Comparison of the solar load onto the Manikin for clear sky conditions, south-façade Hospital, Denver.

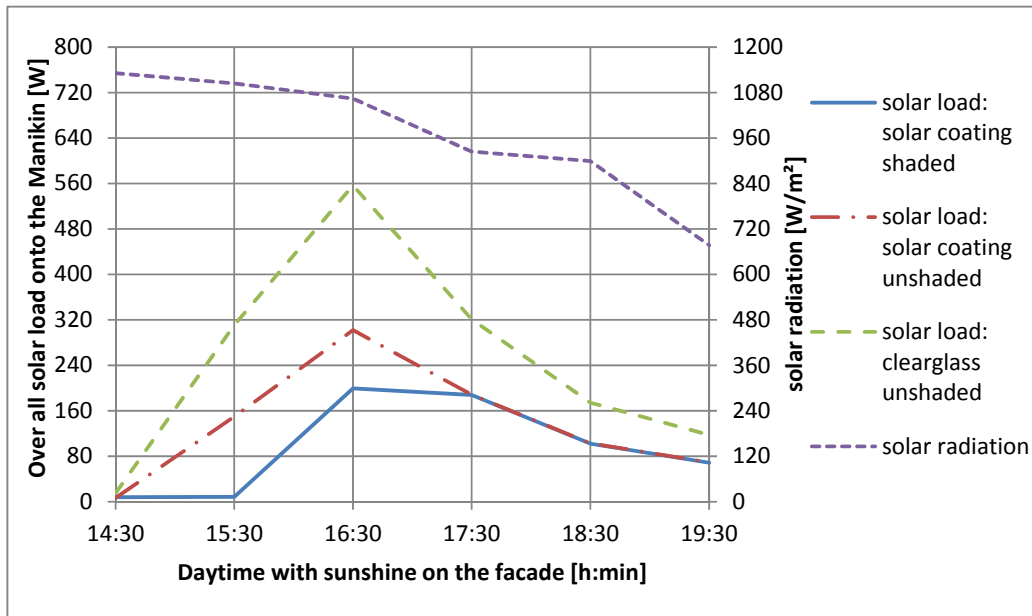


Figure 58: Comparison of the solar load onto the Manikin for clear sky conditions, west-façade Hospital, Denver.

As seen in these two figures, the solar load onto the Manikin is indeed affected by the shading device. However, the same shading construction on the two façades has different effects. Figure 57 shows a quite similar course for the three different façades. Only the amplitude of the curves gets less compared to the clearglass façade. This is caused again by the lower solar transmittance of the window, and additionally through the shaded part of the façade with slat shading.

Unlike for the south façade, figure 58 shows a different effect. From 2:30 to 5:30 the solar load is affected the same way as on the south façade. The course of the curves are quite similar, with the exception of the falling amplitude. After 5:30 Pm, the solar load for the simulation of the shaded and unshaded window with solar coating become almost equal. This effect is to be found in the low altitude of the sun around this time. This low altitude results in a less tilted incidence angle of the solar beam, which has the effect of a small shadow, produced by the slat shading. So the shading still throws a shadow on the façade, but it affects only the very upper area of the window, which does not match the manikin for a low tilted incidence angle. Separating the solar load into the direct and diffuse part describe this effect in more detail.

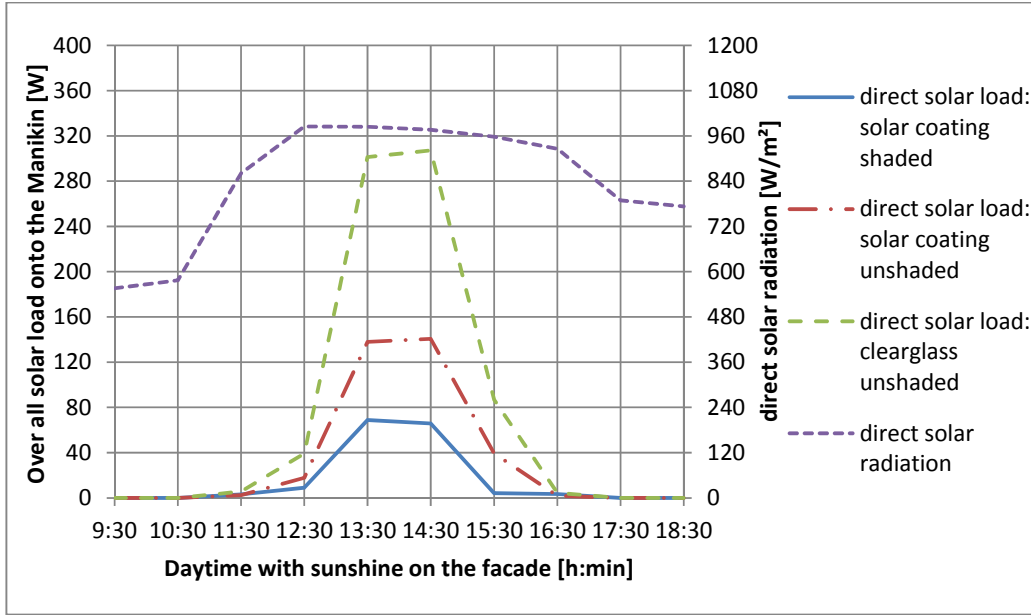


Figure 59: Comparison of the direct solar load onto the Manikin for clear sky conditions, south-façade Hospital, Denver.

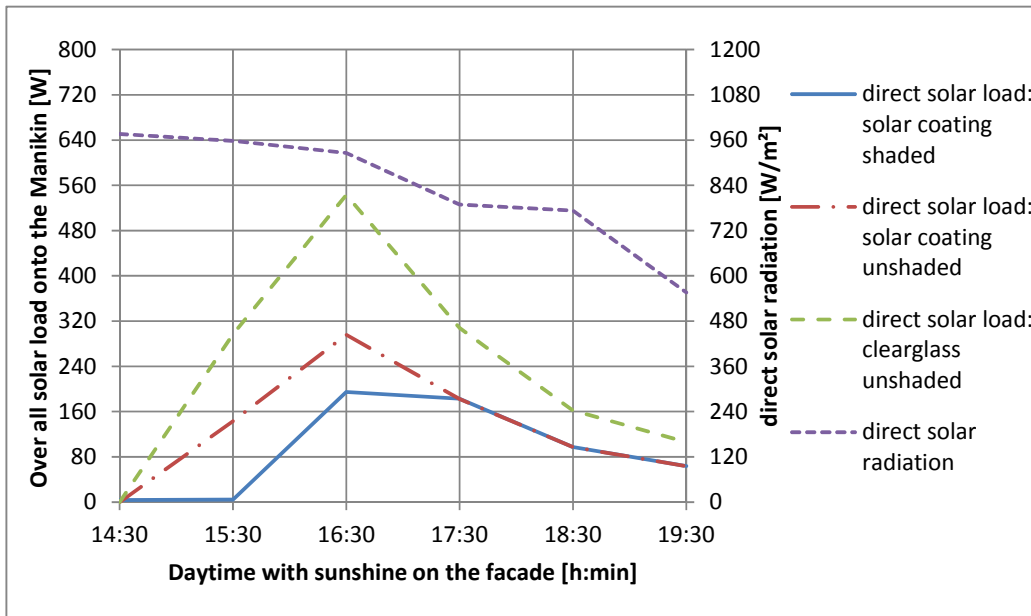


Figure 60: Comparison of the direct solar load onto the Manikin for clear sky conditions, west-façade Hospital, Denver.

The direct radiation in figure 59 and 60 represents, similar to the Helios examination, the main amount of the solar radiation. Hence the graphs for the south and west façade have principally the same course as for the combined solar radiation, and were described before. The diffuse part of the solar radiation however shows a different effect on the solar load.

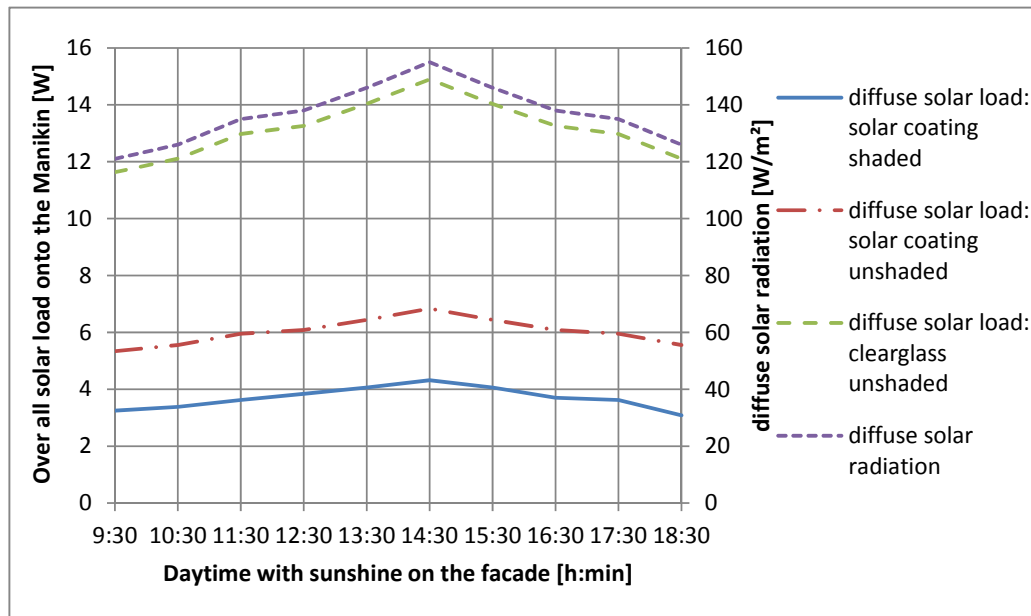


Figure 61: Comparison of the diffuse solar load onto the Manikin for clear sky conditions, south-façade Hospital, Denver.

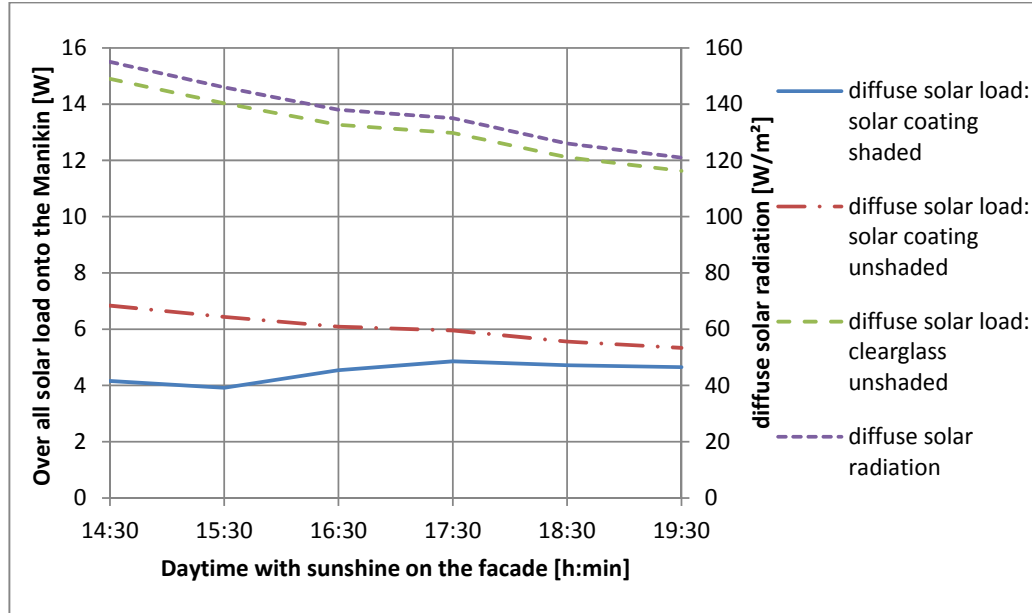


Figure 62: Comparison of the diffuse solar load onto the Manikin for clear sky conditions, west-façade Hospital, Denver.

The graphs of the solar load in figure 61 for the south façade are quiet symmetric, with the peak at 2:30 PM, which is caused by a combination of the highest solar radiation and the highest incidence angle of the solar beam. However, unlike the solar load for the south façade, figure 62 shows some differences. The solar load for the shaded façade falls within the time from 2:30 PM to 3:30 PM, which is a quiet similar behavior compared to the south façade. After 3:30 PM the solar load starts rising till 5:30 PM, while the two other solar loads continue falling.

This behavior is to be found again by the effect of the slat shading. As described before, the altitude of the sun and therefore the incidence angle of the solar beam become minor for the afternoon and evening. This results in a minor shaded area of the window. So the combination of shaded and unshaded areas of the window is more and more influenced by the solar load of the unshaded façade, whose values of the solar load are notable greater than for the shaded facade. As the result, the solar load starts rising slightly for a minor shadowed area. After 5:30 PM the values of the shaded part become so small, that the run of the curve approaches the one of the unshaded façade, only with slightly lower values. This effect becomes even clearer for the examination for cloudy sky conditions.

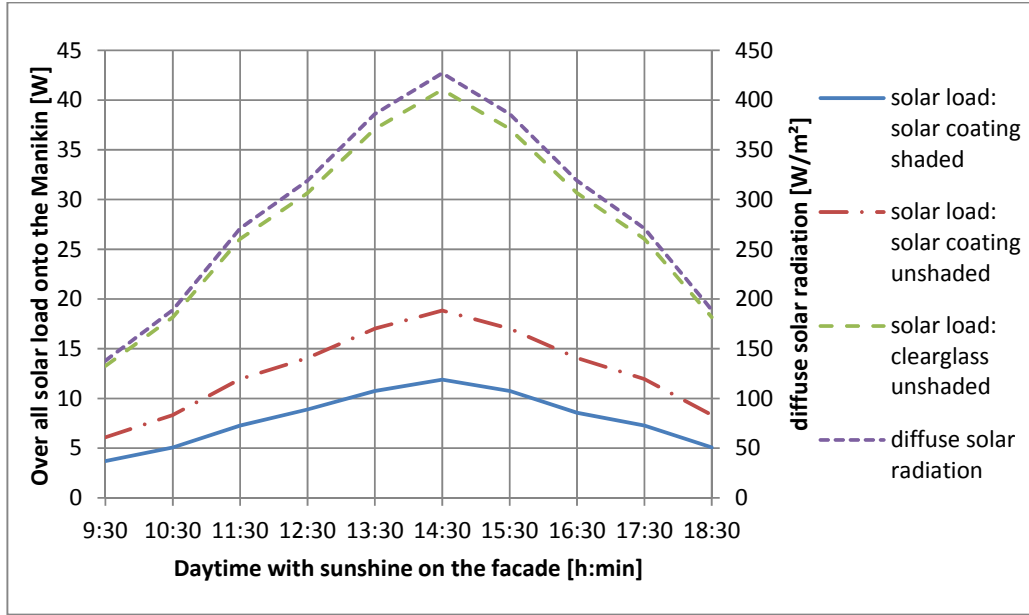


Figure 63: Comparison of the diffuse solar load onto the Manikin for cloudy sky conditions, south-façade Hospital, Denver.

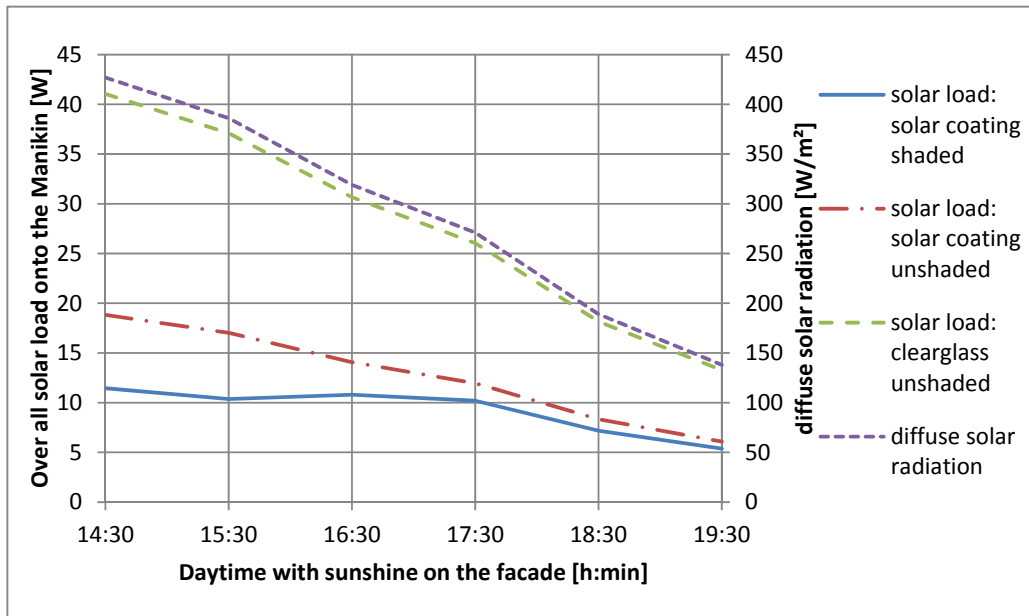


Figure 64: Comparison of the diffuse solar load onto the Manikin for cloudy sky conditions, west-façade Hospital, Denver.

The solar load for the south façade here is quite similar to the one in figure 61, with the exception of the amplitude of the curves. This is caused, comparable to the Helios examination, through the higher amount of diffuse radiation. The solar load on the west façade behaves similar as shown in figure 62, but the effect of the process, described for figure 62 becomes more detailed here. The solar load of the shaded façade falls within the time of 2:30 PM and 3:30 PM and rise then again until the influence of the shaded part becomes that minor, that the curve approaches the course of the unshaded façade.

This examination shows that the shading devices have different effects on the solar load for the two facades. The protection for the south façade on the one hand is quite effective over the day, while the protection for the west façade gets minor for the afternoon and evening. As this effect is caused by the course of the sun, it can only be avoided through improvements to the shading device on the west façade, as for instance a more protruding slat shade. Anyway, this examination provides clarity about the effect of the projected shading device, and allows whether to accept the effects of the actual shading device, or to improve it for a greater protection.

5. Conclusion

The purpose of this research is to develop a tool that provides the opportunity of calculating the solar load onto occupants in a room. The tool uses the bidirectional scattering distribution function for windows and the view factor calculation for the geometric conditions. This allows application to any possible combination of boundary conditions. This includes for example different kinds of facades with varying structures and properties, as well as different geometries of the environment and varying positions of occupants within.

The development for the very coarse discretized environment and the occupant showed that this theoretical approach of the combination of BSDF's and view factors results in reasonable solar load values for the body segments of the manikin. Further examinations were focused on the effects of varying level of discretization. The point of interest was, if and how coarse or detailed discretizations affect the simulation results, and if there were changes in preciseness of the solar load values for varying discretizations.

This validation study was developed very precisely, as numerical calculations are seen to be quite sensitive to the level of discretization. The structure of the numerical grid itself was examined as well as the level of discretization. This proved that a different structure of the grid does indeed have an effect on the simulation results, but that it is minor compared to changes in discretization detail. In particular, a too-coarse discretization results in large deviations from the predicted solar load values. However, the examination also showed that improvements to the calculation results become minor at some level of detail. Hence it has to be evaluated if the benefits of a minor improvement of the results prevail over the disadvantages of extended calculation time and hardware recourses, or if the deviation is still acceptable.

With the awareness of the effects of variation in the numerical grid and the discretization, an application of the tool to two different buildings in the United States presents its practical benefits. These are on the one hand the Helios Building in Berkeley, California, and on the other hand a Hospital in Denver, Colorado. The question for both buildings was whether the installed shading devices affect the solar load onto occupants and how.

The results of a simulated design day showed that the shading devices indeed reduced the solar load. The Helios building shades reduced the solar load for the max value about 70%, compared to an unshaded façade with the same window properties, and about 90%, compared to an unshaded clearglass façade. The effect of the shading device at the Hospital in Denver differed, depending on the observed façade, as the south and west façade were examined. While the shading device affected the solar load for the south façade with a maximal reduction of about 50%, compared to the unshaded façade with the same properties, and about 80%, compared to a unshaded clearglass façade, so were the reductions on the west façade about 30% or 60%, respectively. Here, especial for the late afternoon, the effect of the shading device became almost zero, caused by the low altitude of the sun in the west.

These examinations show that the developed solar load calculation represents indeed a useful tool for the design process of buildings. It is now possible to obtain precise information about the solar load onto occupants for any possible façade properties, any shading and room geometries, and any location of the simulated environment. Especial combinations of complex fenestration systems, which are divided into several areas, each with different properties can be simulated now very precisely.

Furthermore, caused by the numerical approach of the calculation process, the simulation results should become over time even more precise. This will be possible through the still ongoing development and improvement of computer hardware. With these increased hardware recourses, the tool will be able to simulate with a much higher level of discretization detail. So the limiting hardware resources of today might do not represent a problem in the future.

Also, as described already within the introduction, the rise of a practical application of thermal comfort calculation like the Berkeley Human Thermal Comfort Model will benefit from this tool. As the exact influence of the solar radiation into a building represents there still a problem, so will this tool be able to add a useful source of input parameter, to predict the thermal response of occupants to the designed environment. This is further not only limited to the design of buildings, as the car industry is using detailed thermal comfort calculations as well.

However, especially for the design process of buildings, this tool provides another benefit. Although the development of this tool was focused on the calculation of the solar load onto occupants within the environment, it has also great potential to calculate the overall solar load into a building or room, respectively. To achieve this kind of application, there has to be found a solution to handle the geometrical and numerical instabilities, described during the validation study in chapter 3.7.2. However, even this particular part will become a very important parameter during summer periods, to predict necessary cooling loads of air conditioning. As low energy consumption for buildings becomes more and more desirable, so will this increase the quality and vary of choices for the building configuration during the design process. Hence and hopefully, with the final result of buildings, which provide a high level of comfort in combination with a minimum of energy consumption.

So as the final statement for this research, it can be said, that it achieved the benefits it hypothesized. However, the still-quite complex calculation process has to be improved and simplified to provide the opportunity of a truly widespread application, and realization of the tool's advantages.

References

ANSI/ASHRAE Standard 55 (2010). *Thermal Environmental Conditions for Human Occupancy*. Atlanta, GA: American Society of Heating, Refrigerating and Air-Conditioning Engineers.

Carli (2006). *Calculation of optical properties for a venetian blind type of shading device*. Document revision 38. Amherst, MA: Carli Inc.

DIN EN 410 (1998). *Glas im Bauwesen, Bestimmung der lichttechnischen und strahlungsphysikalischen Kenngrößen von Verglasungen*. Berlin: Beuth Verlag GmbH.

DIN EN 13363-2 (2005). *Sonnenschutzeinrichtungen in Kombination mit Verglasung*. Berlin: Beuth Verlag GmbH.

Duffie, J.A., Beckman, W.A. (1991). *Solar engineering of thermal process*. 2nd ed. New York, NY: J. Wiley & Sons.

Fermi, E. (1956). *Thermodynamics*. New York, NY: Dover Publications.

Fiala, D., Lomas, K.J., Stohrer, M. (1999). A computer model of human thermoregulation for a wide range of environmental conditions: the passive system. *Journal of Applied Physiology* 87:1957-1972, 1999.

Fiala, D., Lomas, K.J., Stohrer, M. (2001). Computer prediction of human thermoregulatory and temperature responses to a wide range of environmental conditions. *International Journal of Biometeorology* 45(2), 143-159.

Fiala, D., Lomas, K.J., Stohrer, M. (2001). *A computer model of human thermoregulation for a wide range of environmental conditions: the passive system*. Leicester, UK: De Montfort University Leicester.

Freire, R.Z., Oliviera, G.H.C., Mendes, N. (2008). Predictive Controllers for Thermal Comfort Optimization and Energy Savings. *ABCM Symposium Series in Mechatronics – Vol. – 3 pp. 839-848.*

Gao, C., Kuklane, K., Holmér, I. (2005). *Using 3D whole body scanning to determine clothing area factor.* Lund: Lund University.

Herwig, H., Moschallski, A. (2006). *Wärmeübertragung.* Hamburg: Vieweg+Teubner.

Huizenga, C., Zhang, H., Arens, E. (2001). A model of human physiology and comfort for assessing complex thermal environments. *Building and Environment* 36 (2001), 691-699.

ISO 7730 (2005). *Ergonomics of the thermal environment – Analytical determination and interpretation of thermal comfort using calculation of the PMV and PPD indices and local thermal comfort criteria.* 3rd ed. Geneva: ISO copyright office.

ISO 9050 (2003). *Glass in building-Determination of light transmittance, solar direct transmittance, total solar energy transmittance, ultraviolet transmittance and related glazing factors.* 2nd ed. Geneva: ISO copyright office.

ISO 11664-2 (2011). *Colorimetry – Part2: CIE standard illuminants.* Wien: Austrian Standards Institute.

ISO 15099 (2002). *Thermal Performance of Windows, Doors and Shading Devices-Detailed Calculations.* Geneva: ISO Central Secretariat.

Jonsson, J.C., Lee, E.S., RuBin, M. (2008). *Light scattering properties of a woven shade-screen material used for day lighting and solar heat-gain control.* Berkeley, CA: Lawrence Berkeley National Laboratory.

Jonsson, J.C., Branden, H., (2006). *Obtaining the Bidirectional Transfer Distribution Function of Isotropically Scattering Materials Using an Integrating Sphere*. Berkeley, CA: Lawrence Berkeley National Laboratory.

Klems, J.H., Warner, J.L., Kelley, G.O. (1995). A new method for predicting the solar heat gain of complex fenestration systems. *ASHRAE Solar Heat Gain Project 548-RP Final Report*. 1-35.

Kost, A. (1994). *Numerische Methoden in der Berechnung elektromagnetischer Felder*. Berlin: Springer Verlag.

Mitchell, R., et al. (2008). *Window6.2/Therm6.2 Research Version User Manual*. Berkeley, CA: Lawrence Berkeley National Laboratory.

Mitchell, R., et al. (2011). *Therm6.3/Window6.3 NFRC Simulation Manual*. Berkeley, CA: Lawrence Berkeley National Laboratory.

Newton, C.C. (2007). *A concentrated solar thermal energy system*. Thesis (M.Sc.). The Florida state University.

NFRC 100 (2010), *Procedure for Determining Fenestration Product U-factors*. Greenbelt, MD: National Fenestration Rating Council.

NFRC 300 (2002). *Standard test method for determining the solar optical properties of glazing materials and systems*. 2nd ed. Silver Spring, MD: National Fenestration Rating Council.

Siegel, R., Howel, J.R. (1972). *Thermal Radiation Heat Transfer*. New York, NY: McGraw-Hill Book Company.

Stolwijk, J.A.J. (1971). *A mathematical model of physiological temperature regulation in man*. New Haven, CT: Yale University School of Medicine.

University of California, Berkeley (2009). *University of California Berkeley Helios Energy Research Facility*.

Walton, G.N. (2002). *Calculation of obstructed view factors by adaptive integration*. NISTIR 6925. Gaithersburg, MD: National Institute of Standards and Technology.

Ward, G., et al. (2011). *Simulating the Daylight Performance of Complex Fenestration Systems Using Bidirectional Scattering Distribution Functions within Radiance*. Berkeley, CA: Lawrence Berkeley National Laboratory.

Watson, R.D., Chapman, K.S. (2002). *Radiant Heating and Cooling Handbook*. New York, NY: McGraw-Hill Companies.

Annex

Annex 1: Prediction or calculation of Thermal Comfort with different models

Annex 2: Discretization of the inner hemisphere (Full Size)

Annex 3: Discretization of the outer hemisphere (Full Size)

Annex 4: Angles of the inner hemisphere (Full Size) with related Bin-numbers

Annex 5: Angles of the outer hemisphere (Full Size) with related Bin-numbers

Annex 6: Solid angle calculation

Annex 7: Picture documentation Helios building Berkeley, California

Annex 1. Prediction or calculation of Thermal Comfort with different models

Today, the development of new buildings has two important factors of immediate concern to the occupants. The first is energy saving, given the rising cost of energy and the growing awareness of the need for energy efficiency as a contributor to eco-friendly living. The other factor is the well being and comfort of the occupants in their environment, which is becoming more and more important in the initial design of buildings.

This whole matter of feeling comfortable is now generally referred to as Thermal Comfort. Occupants want to feel neither too warm nor too cold in their buildings – which mean that for an optimal feeling of comfort the energy transfer between occupants and the environment should be balanced. However, the thermal balance of human beings depends on many different factors, like the physical activity or clothing of occupants, as well as air temperature, air velocity, humidity, and mean radiant temperature of the environment. In predicting the thermal comfort of occupants, there are several ways to calculate, such as simplified models, adapting models, and multi-segment models – each described in the following parts of this chapter.

Today, the most common simplified model for calculating thermal comfort is the ISO (International Organization for Standardization) 7730. As described before, the thermal sensation of human beings is quite complex, because it depends on several different factors, such as the clothing and activity level of occupants, as well as air temperature, air velocity, humidity and radiant temperature of the environment.

All these factors are included in the calculation of the PMV (predicted mean vote), which is the main calculation result used in this simplified model. A further result is the PPD (predicted percentage dissatisfied), which is obtained from the PMV. Thermal discomfort could also occur as a result of local cooling or heating effects, such as radiant temperature asymmetries, as in the form of warm or cold walls and floors, through drafts, and differences in the vertical air temperature. However, calculating thermal comfort with a simplified model depends on several conditions.

For example, calculating the PMV is mainly based on steady-state conditions, which means that the boundary conditions of occupant and environment are fixed. The ISO 7730 certainly allows a few little variations of the boundary conditions. Within these ranges, the validity of the calculation equations is granted, but exceeding them will result in variations that are too wide.

The PMV is an index, a predicted mean value of votes of a large group of humans for a given environment. This vote for thermal sensation ranges on a 7-point scale from -3 for a sensation of cold, to +3 for a sensation of heat, as shown in Table A.1.

Table A.1: 7-point thermal sensation scale,
(according to ISO 7730 (2005, p. 2))

+3	Hot
+2	Warm
+1	Slightly warm
0	Neutral
-1	Slightly cool
-2	Cool
-3	Cold

This table is based on the heat balance of a human body. Such a thermal balance results if the amount of internal heat production is equal to the loss of heat to the environment. Under moderate environmental conditions, the human body maintains thermal balance through variation of skin temperature and sweat secretion.

Calculating the PMV after ISO 7730 (2005, p. 3) requires the use of four different equations.

$$\begin{aligned}
 PMV = & [0.303 \cdot \exp(-0.036 \cdot M) + 0.028] \cdot \\
 & \left\{ \begin{array}{l} (M - W) - 3.05 \cdot 10^{-3} \cdot [5733 - 6.99 \cdot (M - W) - p_a] \\ -0.42 \cdot [(M - W) - 58.15] - 1.7 \cdot 10^{-5} \cdot M \cdot (5867 - p_a) \\ -0.0014 \cdot M \cdot (34 - t_a) - 3.96 \cdot 10^{-8} \cdot f_{cl} \\ \cdot [(t_{cl} + 273)^4 - (t_r + 273)^4] - f_{cl} \cdot h_c \cdot (t_{cl} - t_a) \end{array} \right\} \quad (1)
 \end{aligned}$$

$$t_{cl} = 35.7 - 0.028 \cdot (M - W) - I_{cl} \cdot \left\{ \frac{3.96 \cdot 10^{-8} \cdot f_{cl} \cdot [(t_{cl} + 273)^4 - (t_r + 273)^4]}{+ f_{cl} \cdot h_c \cdot (t_{cl} - t_a)} \right\} \quad (2)$$

$$h_c = \begin{cases} 2.38 \cdot |t_{cl} - t_a|^{0.25} & \text{for } 2.38 \cdot |t_{cl} - t_a|^{0.25} > 12.1 \cdot \sqrt{v_{ar}} \\ 12.1 \cdot \sqrt{v_{ar}} & \text{for } 2.38 \cdot |t_{cl} - t_a|^{0.25} < 12.1 \cdot \sqrt{v_{ar}} \end{cases} \quad (3)$$

$$f_{cl} = \begin{cases} 1.00 + 1.290 \cdot l_{cl} & \text{for } l_{cl} \leq 0.078 m^2 \cdot K/W \\ 1.05 + 1.645 \cdot l_{cl} & \text{for } l_{cl} > 0.078 m^2 \cdot K/W \end{cases} \quad (4)$$

However, as these equations show, there are several parameters that must be known before these equations can be solved, such as the metabolic heat rate M , which is given in watts per square meter and stands for the amount of energy converted by the human body through the transformation of chemical energy into heat and mechanical work by aerobic and anaerobic activities (Freire et al., 2008, p. 2). However, this index is never the same value. It depends on the activity level of the individual involved. A person sitting still has a much lower metabolic rate, than does someone who is running, or doing physically heavy work. Hence the metabolic rate is described also as the metabolic unit. According to ISO 7730 (2005, p. 3) one metabolic unit = 1 met, which stands for a metabolic rate of 58.2 W/m².

Subtracted from the metabolic heat is the index W , which stands for the effective mechanical power and is given also in watts per square meter. W is thus the amount of the aforementioned transformation of chemical energy into mechanical work. The insulation provided by clothing, I_{cl} , is also an important part of the equation and is given in square meters Kelvin per watt. This factor varies greatly according to the respective season. After ISO 7730 (2005, p. 3) one clothing unit = 1 clo, which stands for an insulation of 0.155 (m² · C°/W).

Additional parameters within the equation are the clothing surface area factor f_{cl} , defined (Gao et al., 2005, p. 1) as $f_{cl} = A_{cl}/A_D$, the air temperature t_a within the environment (Freire et al. 2008, p. 2) for the dry-bulb temperature or just indoor temperature, the mean radiant temperature t_r , the relative air velocity v_{ar} , the water vapor pressure p_a , as well as convective heat transfer coefficient h_c and surface temperature t_{cl} of the occupants' clothing. More precisely definitions of the parameters can be found in the literature cited.

As described before, the PMV index is developed for steady-state conditions. However, after ISO 7730 (2005, p. 3f) the PMV may also be applied with good approximations during minor variation of one or more variables. The requirement for this step is that the time-weighted averages of these variables during the previous one hour period be applied. Furthermore this index, after ISO 7730 (2005, p. 3f), should be used only for values of the PMV between -2 and +2, and when the six main parameters lie between the following intervals.

- M 46 W/m² to 232 W/m² (0.8 met to 4 met)
- I_{cl} 0 m²K/W to 0.310 m²K/W (0 clo to 2 clo)
- t_a 10 °C to 30 °C
- t_r 10 °C to 40 °C
- v_{ar} 0 m/s to 1 m/s
- p_a 0 Pa to 2700 Pa

The index PPD stands for the predicted percentage dissatisfied. As described before, the PMV predicts the mean value, the situation when a large group of people in the same environment would vote for thermal comfort. However, some individuals' response will differ from this mean vote. So the PPD was developed to provide a means to predict how many people would feel uncomfortably hot or cold. The remaining people would feel neutral or just slightly too warm or slightly cold. So the PPD allows a quantitative prediction of the percentage number of people who are likely feel too warm or too cold in the examined environment.

Since it depends directly on the PMV, the PPD may only be calculated after the PMV is known. For calculating the PPD after ISO 7730 (2005, p. 4) the following equation should be used:

$$PPD = 100 - 95 \cdot \exp(-0.03353 \cdot PMV^4 - 0.2179 \cdot PMV^2) \quad (5)$$

Using this equation shows the percentage of people dissatisfied for a defined PMV. Looking at the PMV range from -2 to +2, the graph of the PPD shows a kind of distribution function as shown in figure A.1. The graph in this figure shows that the percentage of unsatisfied people rises as the PMV gets farther away from the neutral zero vote.

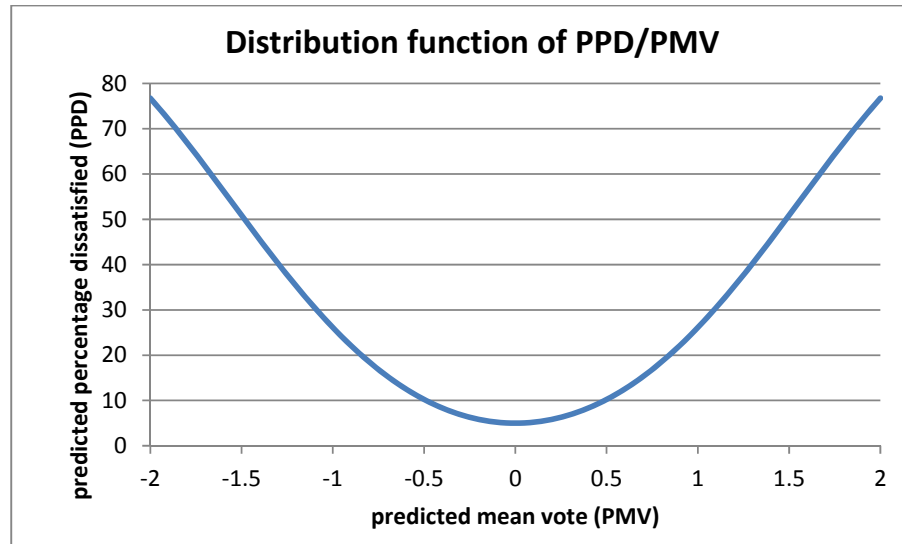


Figure A.1: PPD/PMV distribution function, according to ISO 7730 (2005, p. 5)

Both the PMV and the PPD describe the thermal feeling of the occupant's body as a whole, but thermal dissatisfaction could also occur if only single body parts become too hot or too cold. After ISO 7730 (2005, p. 6) this is known as local discomfort, which has several different causes.

The most common cause is draughts, which often come about through open windows or doors, but also through temperature differences. Also unusually high vertical temperature differences between the head and the ankles could be a cause for local thermal discomfort. Further reasons could be floors being too warm or too cold, and also radiant temperature asymmetries that are too high.

However, not all people are similarly sensitive to local thermal variations. People with high levels of activity are not as sensitive to thermal sensation caused by the higher metabolic rate they produce. Their PMV is not in the range around the zero votes, so mostly they were already feeling uncomfortable for their bodies as a whole, which results in a lower level of discomfort in individual body parts. On the other hand, people with low levels of activity, for example those performing light sedentary activities such as work on a PC, have a relatively neutral PMV around zero for their whole bodies, what makes them more sensible for thermal discomfort in individual body parts.

The simplified model described in the last pages is defined only for steady-state conditions of an environment. But usually there are non-steady-state conditions in given environments. So it is important to know if, and under which circumstances the steady-state method of the ISO 7730 could apply.

The parameters changing under non-steady-state conditions are temperature cycle, temperature drifts, or ramps and transients. After ISO 7730 (2005, p. 11) there are defined ranges of non-steady-state conditions for which the calculation after steady-state conditions may be used. So after ISO 7730 (2005, p. 11), peak to peak variations of less than 1K have no effect on the comfort and the steady-state model may apply. Steady-state calculations also work for a rate of temperature changes less than 2.0 K/h for drifts and ramps.

Regarding the transients, there are three statements that are described in the ISO 7730. The first is that a step change of the operative temperature is felt instantaneously. The second is that after an up-step of the operative temperature, the sensation immediately expires for the new steady-state thermal sensation. The last one is that after a down-step of the operative temperature, the thermal sensation falls in a first step down near the range of the one predicted by the PMV, and then rises after nearly 30 minutes under the new steady-state conditions to the actual level of thermal sensation.

As described before, a calculation using a simplified model like FANGER is used for predicting human thermal comfort for occupants in an enclosed environment. So the parameters with influence on thermal comfort are only internal ones. These are, for example, the mean radiant temperature, the air temperature or the operative temperature, as along with air velocity, air humidity, and thermal stratification. Any values outside the closed environment have no influence on the thermal comfort.

So calculating thermal comfort after a simplified model works for environments with automatically or mechanically controlled conditions, like HVAC systems for example, but not for naturally controlled environments, in which occupants vary the conditions by opening and closing windows. Environments with automatically controlled conditions establish a predefined environmental condition by the heating or cooling of the environment. Hence fluctuations of outdoor conditions like sunshine, or air temperature have

minor influence on the thermal comfort of occupants because they are automatically balanced.

Environments with naturally controlled conditions, however, are different. Here, the occupant himself has the opportunity to control the environmental condition by opening and closing the windows. To predict the thermal comfort for such environments, an adaptive model, like that applied in the American ANSI/ASHRAE Standard 55 (2010) was developed.

The adaptive model after ANSI/ASHRAE Standard 55 (2010, p. 3) relates designed indoor temperatures, respectively temperature ranges, which are acceptable for occupants, to meteorological or climatological outdoor conditions. Field experiments after ANSI/ASHRAE Standard 55 (2010, p. 11) have shown, that the thermal response of occupants in such environments deviate from those in automatically controlled environments, like those described above with HVAC systems. This may be caused through several reasons, like a different thermal experience, the changing of clothes, or the availability of control. Occupants of the environment might choose to change their clothes, or open or close a window when they feel uncomfortable.

As the calculation of thermal comfort using the simple model does not factor in the parameter of outdoor conditions, the adaptive model was developed to calculate thermal comfort for exactly such environments. However, the application of the adaptive model requires several given boundary conditions.

In order to apply the thermal comfort calculation after the adaptive model, the environment has to be equipped with operable windows to the outdoor environment, which can be opened or adjusted by the occupants, as this is the primarily regulation method for the thermal comfort. Furthermore, no mechanical cooling system, like refrigerated air conditioning, is permitted in the environment. This requirement may not apply to mechanical ventilation systems, as long as the opening and closing of windows remains the main means of regulating the temperature for thermal comfort. A heating system generally is allowed to be installed in the environment, but it has to be turned off if the adaptive model is to be applied.

Furthermore, an application of the adaptive model after ANSI/ASHRAE Standard 55 (2010, p. 11) is possible only for occupants performing near sedentary physical activities, like deskwork, with a metabolic rate between 1.0 and 1.3. The metabolic rate is the same as described earlier in this chapter. An estimation of the metabolic rate of the occupants can be made, for example after the Normative Appendix A of the ANSI/ASHRAE Standard 55 (2010).

If the conditions of an environment meet these criteria, the indoor operative temperature, as described earlier in this chapter, can be determined after figure A.2.

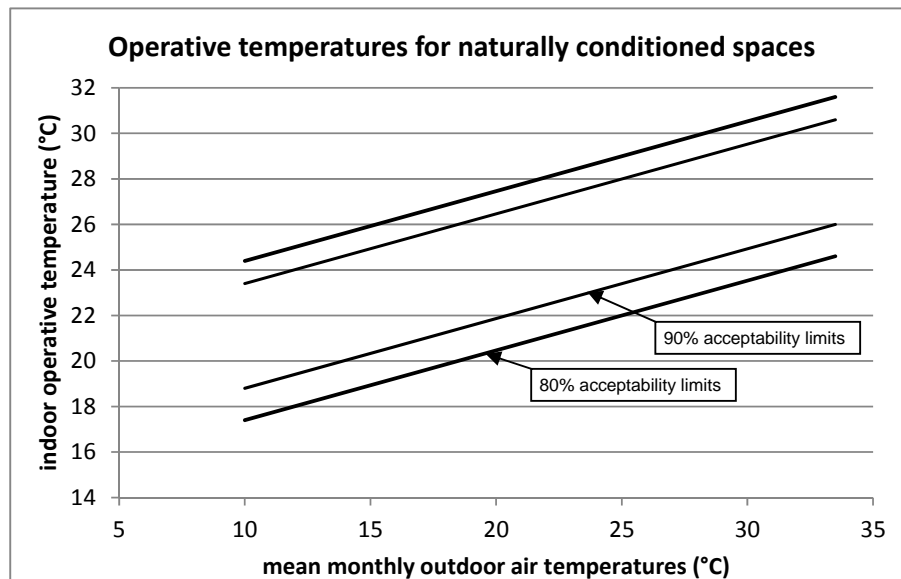


Figure A.2: Acceptable operative indoor temperatures after the adaptive model, according to ANSI/ASHRAE Standard 55 (2010, p. 12)

After ANSI/ASHRAE Standard 55 (2010, p. 12), this figure is based on a global database of 21,000 measurements, which were measured primarily in office buildings. As shown here, the indoor operative temperature is dependent on the mean monthly outdoor air temperature. This mean monthly outdoor air temperature is defined after ANSI/ASHRAE Standard 55 (2010, p. 3) as the arithmetic average of the mean daily minimum, as well as the mean daily maximum of the dry-bulb outdoor air temperature for the examined month. Figure A.2 therefore shows two different ranges for the indoor

operative temperature, one for 90% acceptability and the other one for 80% acceptability. The range between the two 80% limit lines stands for regular application and should be used in most cases. The 80% figure thus means that 10% of all occupants feel uncomfortable for the whole body, and another 10% feel uncomfortable for an individual body part. The 90% acceptability is used only under special circumstances, where a higher level of thermal comfort is desired.

Figure A.2 also shows the minimum and maximum of the mean monthly outdoor air temperature, for which the ranges of the indoor operative temperature are shown. After ANSI/ASHRAE Standard 55 (2010, p. 12) the allowable operative temperatures should not be extrapolated to mean monthly outdoor air temperatures above or below the given boundaries. These both boundaries are for the lower one 10°C, or 50°F, and for the upper one 33.5°C, or 92.3°F. The adaptive model can be applied only within these outdoor conditions for naturally conditioned environments.

When using the adaptive model by application of figure A.2, it is not necessary to determine the parameter for local thermal comfort, because figure A.2 already takes these into. Also it is not necessary to estimate the clothing factor for this application, because figure A.2 takes into account the occupants' clothing adaptation in such naturally conditioned environments by setting the range of acceptable indoor temperature in relationship to the outdoor climate.

So calculating the thermal comfort after the adaptive model will follow equation 6 for occupants in near sedentary activities, with no direct sunlight and not exposed to an air velocity over 0.20 m/s, or 40 fpm.

$$t_o = (t_a + t_r)/2 \quad (6)$$

Where the indices stands for:

t_o = the operative temperature,

t_a = the air temperature,

t_r = the mean radiant temperature.

Beyond the two different calculation methods there exists another model, one that provides more detailed calculation results. This is the multi-segment model. One of these multi-segment models was developed by Stolwijk during 1966. Based on his model of thermoregulation reported in Stolwijk (1971), other, more advanced model were developed. One of these is the Berkeley Human Thermal Comfort Model.

In general, a multi-segment model uses, as the name already describes, multiple body segments for the calculation of thermal comfort, instead of the whole body as in the other two models. This means in detail, that the thermal comfort will be calculated for each determined body segment. The number of observed body segments used in the calculation may vary. Stolwijk's model (1971, p. 3) uses six different body segments: head, torso, arms, hands, legs and feet. On the other hand, the Berkeley Human Thermal Comfort Model can calculate, after Huizenga et al. (2001, p. 691 f), general thermal comfort for an arbitrary number of segments, but usually uses sixteen body segments, as shown in figure A.3.

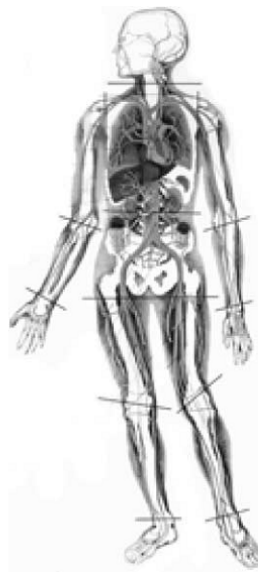


Figure A.3: Typical segmentation of the human body used in the Berkeley Comfort Model, Huizenga et al. (2001, p. 692)

Such a possibility to divide the human body into arbitrary segments takes effect especially in non-uniform environments with large local variations in temperature and heat flux. Each of the segments consists of four body layers, which represents the human physiology. These four body layers are the core, muscle, fat, and skin tissues. Advanced models like the Berkeley Human Thermal Comfort Model add a fifth layer for clothing.

For the calculation of thermal comfort, the multi-segment model uses several heat transfer parameters, like heat transfer through radiation, convection, conduction, and sweating, along with resulting evaporation. However, to simulate realistic human behavior, thermal processes inside the human body have to be included in the thermal comfort calculation. Again, Stolwijk developed after Huizenga et al. (2001, p. 692) a blood flow model, which calculates the effects of heat loss to environments with different temperatures. In this blood flow model, arteries and veins permit the flow of blood from the inner core through the body and back to the core, as the arteries pump the blood from the core through the body, and the veins carry it back again.

Stolwijk's original blood flow model thus assumes, after Huizenga et al. (2001, p. 692), that the arterial blood temperature does not change during its path through the body. So the heat exchange between local tissues and the blood is simplified to this steady blood temperature. For large arteries deep inside the human body, this assumption is so far correct, because of the insulation through the body fat and the short heat exchange between blood and surrounding tissues. Smaller arteries, such as those in the arms or hands, are not so isolated, and the heat exchange with the surrounding tissues is higher, which makes the assumption of Stolwijk unrealistic.

Measurements of blood temperature in arms provided, after Huizenga et al. (2001, p. 692), a drop in blood temperature of as much as 2°C in cool environments. Advanced models have modified Stolwijk's blood flow model by factoring in, after Huizenga et al. (2001, p. 692) a central artery-vein countercurrent heat exchange as well as an improved blood perfusion model to estimate the blood flow to local tissues. Figure A.4 shows such a blood flow model for an extremity.

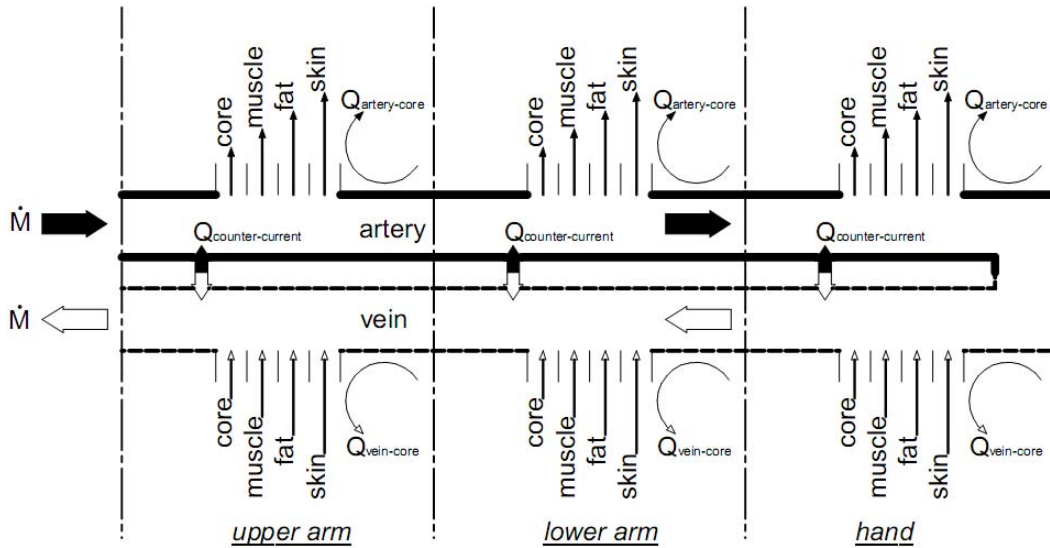


Figure A.4: Blood flow model of the Berkeley Human Thermal Comfort Model, according to Huizenga et al. (2001, p. 693)

The above mentioned clothing layer is a non-mass layer in Stolwijk's work. He developed a simplified node model including the four body layers with the additional clothing layer as shown in figure A.5, while advanced calculation methods modeled a node structure with an additional clothing layer that influences heat loss through isolation and evaporation, as shown below in figure A.6.

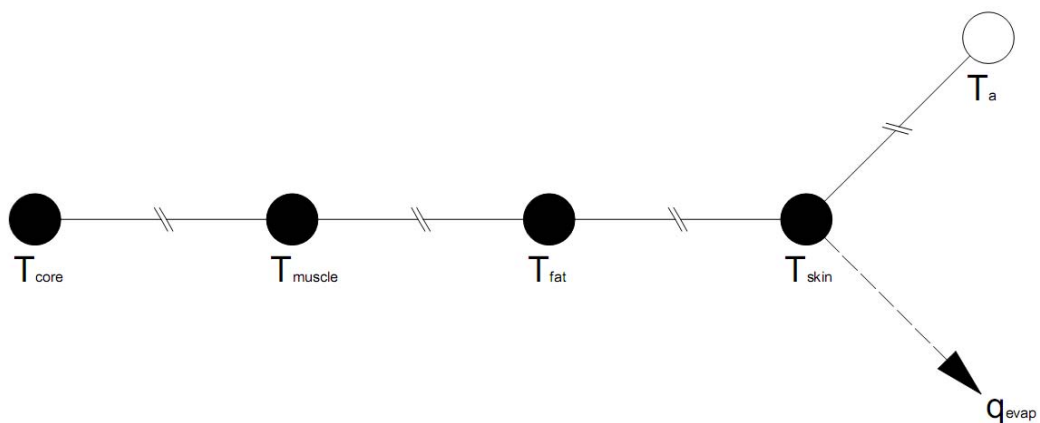


Figure A.5: Simplified node model of Stolwijk, according to Huizenga et al. (2001, p. 693)

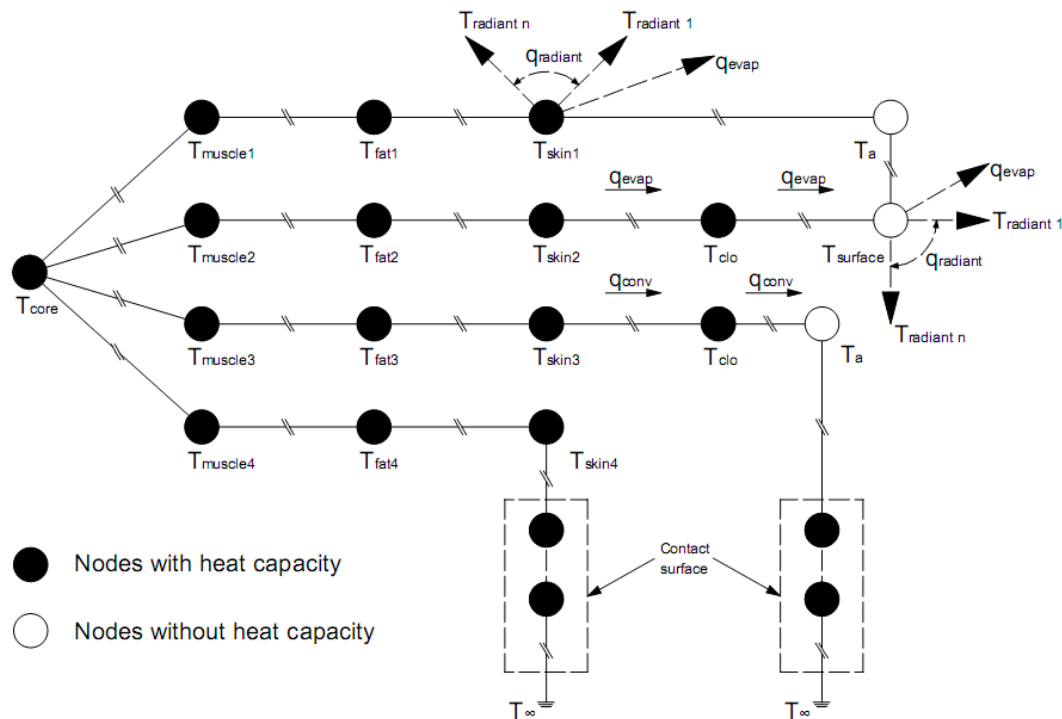


Figure A.6: Advanced node model of the Berkeley Comfort Model showing four parallel heat paths, according to Huizenga et al. (2001, p. 694)

As seen in figure A.6, the advanced node structure provides several opportunities of heat transfer from the core to the environment. Thus, for example, the first path assumes an exposed skin, with radiant and convective heat loss. The second path assumes a clothed skin, again with radiant and convective heat loss. The third path stands for a clothed skin with direct contact to a surface, like a chair for example, and only conductive heat loss, and the fourth path describes exposed skin with direct contact to a surface, again with only conductive heat loss.

Furthermore, multi-segment models like the Berkeley Human Thermal Comfort Model can change the conditions of the environment and the human physiology in so called phases. These phases represent segments of time, in which the environmental conditions are constant, or steady, or varying linearly with time. As the number and length of these phases are not limited, it is possible to create non steady state conditions by generating several short phases. Each phase thus consists, following Huizenga et al. (2001, p. 694), of several input parameters like duration, velocity, metabolic rate,

clothing, air temperature, relative humidity, mean radiant temperature, physiological constants, and contact surface thermal properties.

This allows the investigator not only to change the simulation conditions in the environment, but also to simulate the variation between different environments, like for example a man working in an air-conditioned office, who then goes outside on his walk home, and later sits in his warm living room.

Beside the multi-segment model developed at the University of California at Berkeley, there is another common multi-segment model developed by Dr. Dusan Fiala, which calculates thermal sensation. Fiala's model divides the human system into two parts, a passive and an active one. While the passive system consists of the heat transfer within the body as well as the heat exchange between the body and surrounding surfaces, the active system consists of thermoregulatory responses like shivering, sweating and vasomotion.

To calculate body reactions for certain environmental conditions the human body has previously to be discretized into a physiological model, which consists, after Fiala et al. (1999, p. 2), of 15 spherical or cylindrical body elements: head, face, neck, shoulders, arms, hands, thorax, abdomen, legs, and feet as shown in figure A.7. Furthermore the virtual body was designed to represent an average human. Hence the human properties were defined according to table A.2.

Table A.2: Overall data of the human body for the passive system, according to Fiala et al. (1999, p. 2)

Body weight [kg]	Body fat [%]	A_{sk} [m ²]	$w_{t_{sk}}$ [%]	CO [l/min]	$M_{bas,0}$ [W]
73.5	14.0	1.86	6.0	4.9	87.1

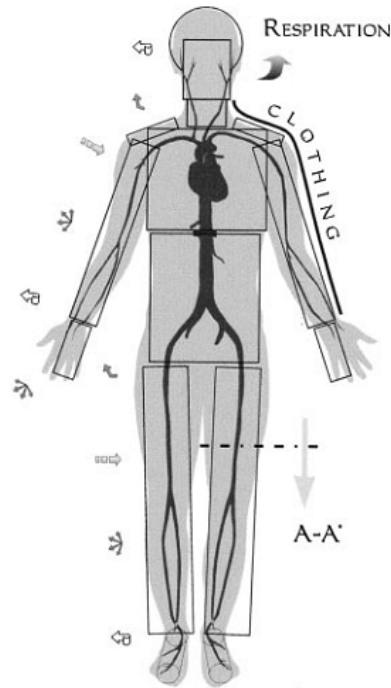


Figure A.7: Schematic presentation of the subdivided average human body, Fiala et al. (1999, p. 2)

The different body segments are further divided into several layers, representing the different body tissues and their varying properties. Overall, Fiala uses seven different tissues such as brain, lung, bone, muscle, viscera, fat, and skin which are arranged as in reality. In addition, Fiala divides the skin into an inner as well as an outer layer, where the inner layer is defined as a 1mm thick region where metabolic heat is generated and blood is perfused while the outer layer with the same thickness has no heat source or thermally significant blood vessels. Each of these tissue layers is furthermore subdivided into one or more tissue nodes. This will be explained more precisely in figure A.8, which corresponds to the section marked A-A in figure A.7.

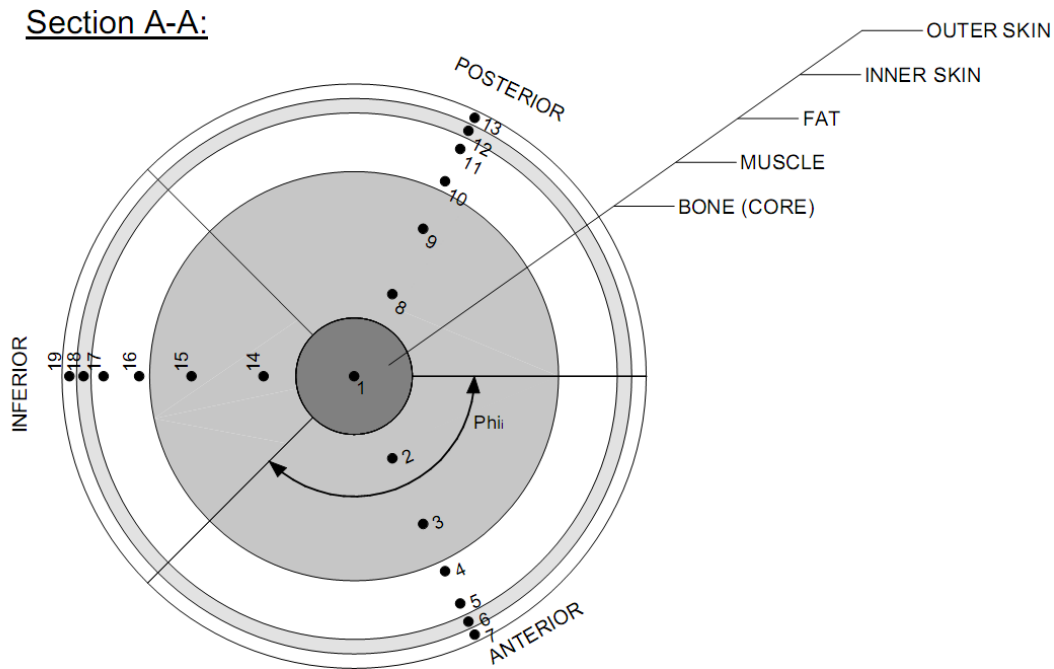


Figure A.8: Schematic presentation of the multi-node structure of a body part, according to Fiala et al. (1999, p. 2)

As figure A.8 shows, the body segments themselves are furthermore divided into different sectors named anterior, posterior and inferior. This division, after Fiala et al. (1999, p. 2), is applied to all body segments except the face and shoulders and takes into account the asymmetric removal of body heat. The anterior and posterior regions thus involve environmental asymmetries, while the inferior region considers body parts that are hidden by other body segments.

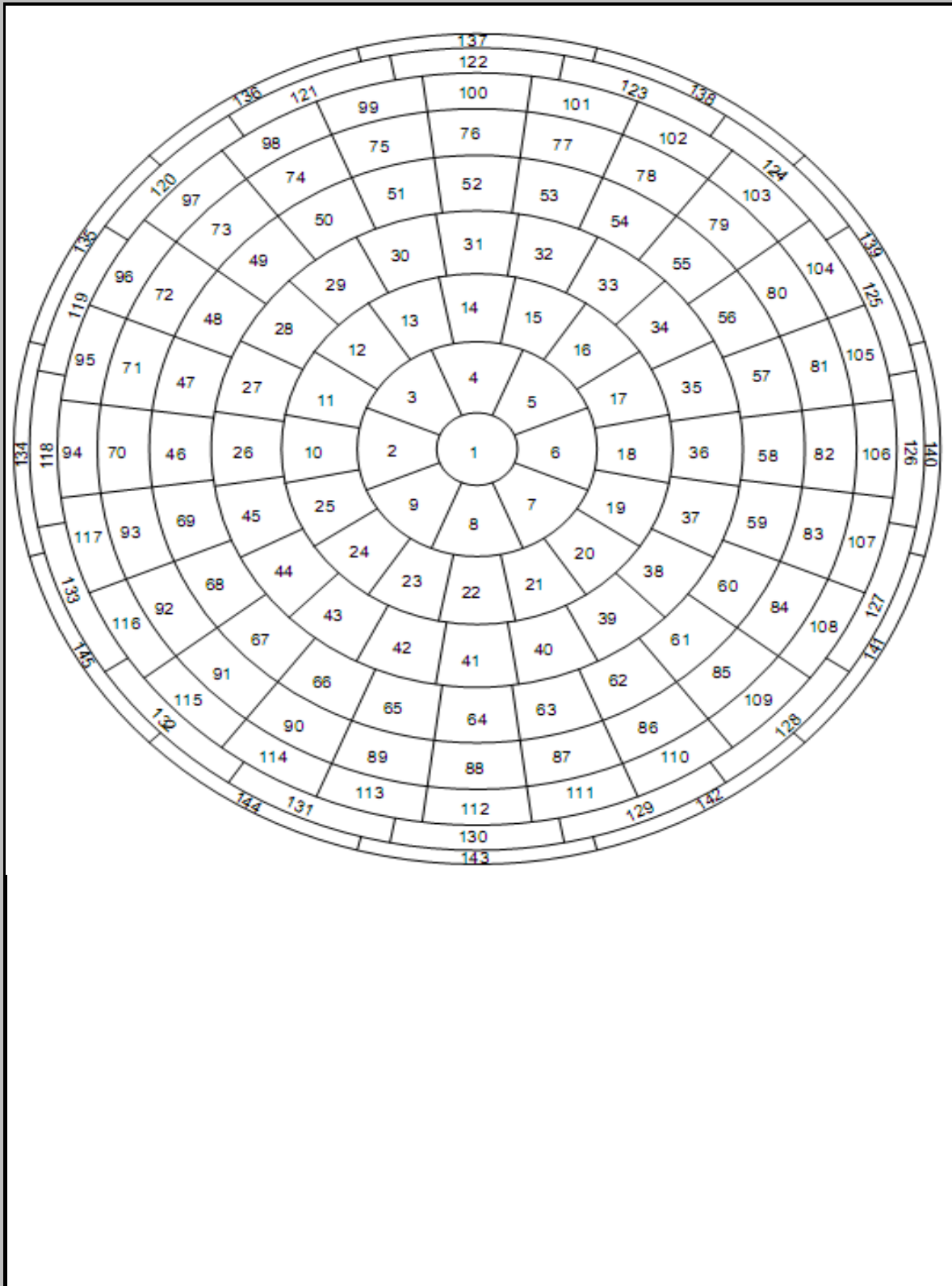
Once the physiological body has been so defined, both the heat transfer mechanism of the passive system inside the body and the heat exchange with the environment can also be described. The heat transfer mechanism inside the body is made up of conduction, metabolism, and blood circulation. After Fiala et al. (1999, p. 5), heat conduction involves temperature variations in a radial direction, while the angular heat flow is ignored. Metabolism or the metabolic heat rate consists of the sum of the metabolic heat rate and an additional heat part, which may be produced, for example, through physical work. Fiala's blood circulation model consists of three main components: the blood pool, the countercurrent heat exchange (CCX), and pathways to individual tissue nodes. The blood flows through arteries from the core

throughout the body. On its way the blood temperature falls as a result of heat exchange via conduction between the blood and the surrounding tissue, and as the blood flows back to the core it warms up, again through the heat conducted from the adjacent arteries. Thus, by the end of the flow circle, the returned blood produces a new blood pool temperature.

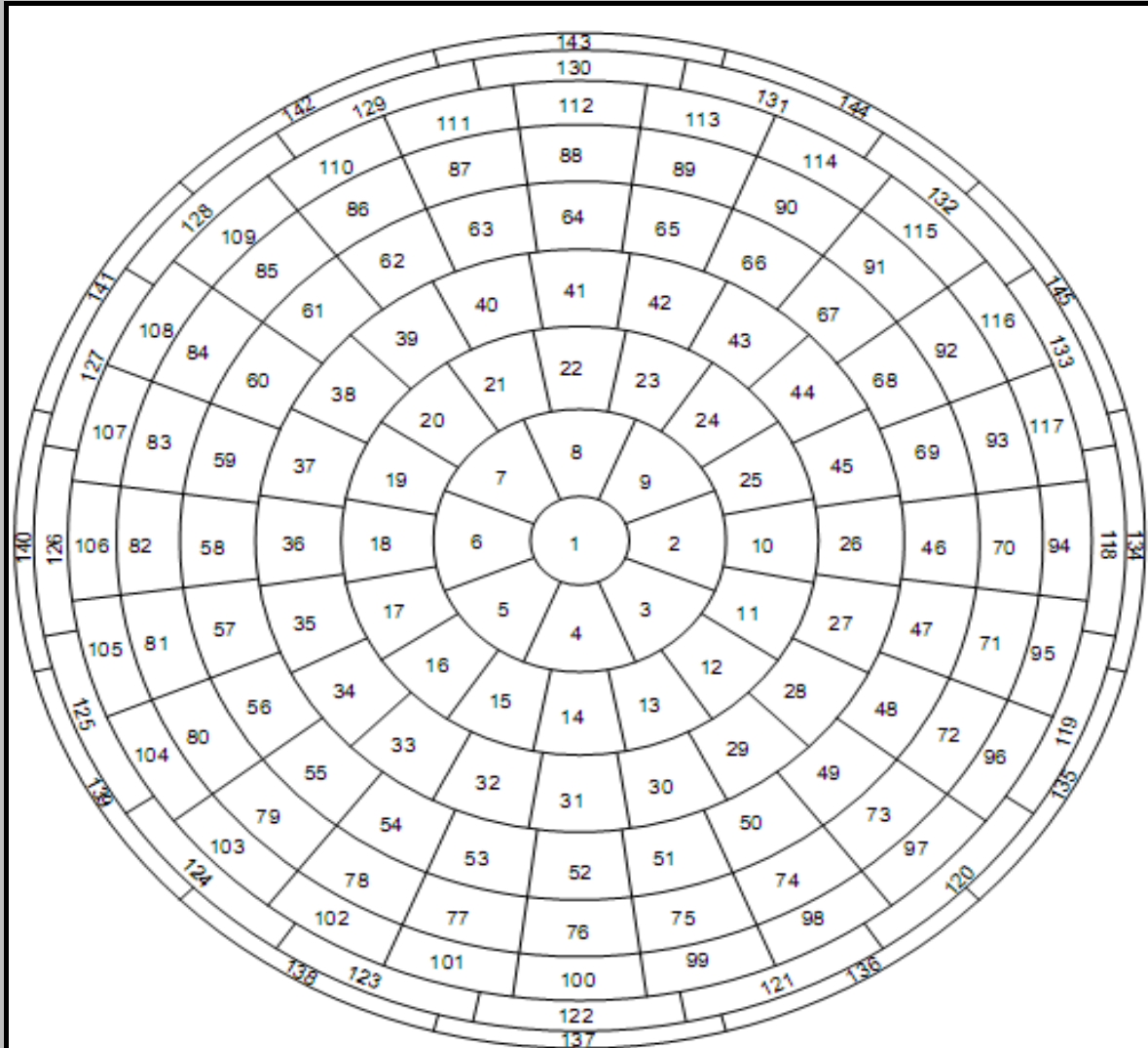
The heat exchange with the environment consists of four mechanisms: convection, radiation, evaporation and respiratory heat loss (Fiala et al., 1999, p. 7). The convection in this exchange is influenced by differences between surface and air temperature, as well as air velocity, while evaporation mainly depends on the water vapor pressure on the skin surface and the air. The radiation is typically the long wave radiation heat exchange between the body and surrounding surfaces under use of view factors. Also included is the irradiation, typical of heat exchange through short wave radiation emitted from high temperature sources like the sun. The heat loss through respiration is, after Fiala et al. (1999, p. 10), less important, since most heat loss happens through the operation of the first three mechanisms, but it is still included for a fully described heat exchange mechanism.

The active system on the other hand considers active control mechanism of the body as a reaction to environmental conditions. The active system therein consists of the mechanism shivering, vasoconstriction, sweating and vasodilatation. The equations of these control mechanism were formulated after Fiala et al. (2001, p. 145) through regression results of existing experiments combined with supra-experimental analyses. The developed equations of the active system can be found in Fiala et al. (2001, p. 146ff).

Discretization of the inner hemisphere (Full Size), 145 Bins



Discretization of the outer hemisphere (Full Size), 145 Bins



Angles of the inner hemisphere (Full Size) with related Bin-numbers

	1.ring	2.ring	3.ring	4.ring	5.ring	6.ring	7.ring	8.ring	9.ring
"Θ" Theta	0° - 5°	5° - 15°	15° - 25°	25° - 35°	35° - 45°	45° - 55°	55° - 65°	65° - 75°	75° - 90°
"Φ" Phi	0° - 360°	67.5° - 112.5°	78.75° - 101.25°	81° - 99°	82.5° - 97.5°	82.5° - 97.5°	82.5° - 97.5°	78.75° - 101.25°	75° - 105°
		22.5° - 67.5°	56.25° - 78.75°	63° - 81°	67.5° - 82.5°	67.5° - 82.5°	67.5° - 82.5°	56.25° - 78.75°	45° - 75°
		337.5° - 337.5°	33.75° - 33.75°	45° - 45°	52.5° - 52.5°	52.5° - 52.5°	52.5° - 52.5°	33.75° - 33.75°	15° - 15°
		22.5° - 22.5°	56.25° - 56.25°	63° - 63°	67.5° - 67.5°	67.5° - 67.5°	67.5° - 67.5°	56.25° - 56.25°	45° - 45°
		292.5° - 337.5°	11.25° - 33.75°	27° - 45°	37.5° - 52.5°	37.5° - 52.5°	37.5° - 52.5°	11.25° - 33.75°	345° - 15°
		247.5° - 292.5°	348.75° - 11.25°	9° - 27°	22.5° - 37.5°	22.5° - 37.5°	22.5° - 37.5°	348.75° - 11.25°	315° - 345°
		202.5° - 247.5°	326.25° - 348.75°	351° - 9°	7.5° - 22.5°	7.5° - 22.5°	7.5° - 22.5°	326.25° - 348.75°	285° - 315°
		157.5° - 202.5°	303.75° - 326.25°	333° - 351°	352.5° - 7.5°	352.5° - 7.5°	352.5° - 7.5°	303.75° - 326.25°	255° - 285°
		112.5° - 157.5°	281.25° - 303.75°	315° - 333°	337.5° - 352.5°	337.5° - 352.5°	337.5° - 352.5°	281.25° - 303.75°	225° - 255°
		157.5° - 112.5°	303.75° - 281.25°	333° - 315°	352.5° - 337.5°	352.5° - 337.5°	352.5° - 337.5°	303.75° - 281.25°	255° - 225°
			258.75° - 281.25°	297° - 315°	322.5° - 337.5°	322.5° - 337.5°	322.5° - 337.5°	258.75° - 281.25°	195° - 225°
			236.25° - 258.75°	279° - 297°	307.5° - 322.5°	307.5° - 322.5°	307.5° - 322.5°	236.25° - 258.75°	165° - 195°
			213.75° - 236.25°	261° - 279°	292.5° - 307.5°	292.5° - 307.5°	292.5° - 307.5°	213.75° - 236.25°	135° - 165°
			191.25° - 213.75°	243° - 261°	277.5° - 292.5°	277.5° - 292.5°	277.5° - 292.5°	191.25° - 213.75°	105° - 135°
			168.75° - 191.25°	225° - 243°	262.5° - 277.5°	262.5° - 277.5°	262.5° - 277.5°	168.75° - 191.25°	
			146.25° - 168.75°	207° - 225°	247.5° - 262.5°	247.5° - 262.5°	247.5° - 262.5°	146.25° - 168.75°	
			123.75° - 146.25°	189° - 207°	232.5° - 247.5°	232.5° - 247.5°	232.5° - 247.5°	123.75° - 146.25°	
			101.25° - 123.75°	171° - 189°	217.5° - 232.5°	217.5° - 232.5°	217.5° - 232.5°	101.25° - 123.75°	
			123.75° - 101.25°	189° - 171°	232.5° - 217.5°	232.5° - 217.5°	232.5° - 217.5°	123.75° - 101.25°	
				153° - 171°	202.5° - 217.5°	202.5° - 217.5°	202.5° - 217.5°		
				135° - 153°	187.5° - 202.5°	187.5° - 202.5°	187.5° - 202.5°		
				117° - 135°	172.5° - 187.5°	172.5° - 187.5°	172.5° - 187.5°		
				99° - 117°	157.5° - 172.5°	157.5° - 172.5°	157.5° - 172.5°		
				117° - 99°	172.5° - 157.5°	172.5° - 157.5°	172.5° - 157.5°		
					142.5° - 157.5°	142.5° - 157.5°	142.5° - 157.5°		
					127.5° - 142.5°	127.5° - 142.5°	127.5° - 142.5°		
					112.5° - 127.5°	112.5° - 127.5°	112.5° - 127.5°		
					97.5° - 112.5°	97.5° - 112.5°	97.5° - 112.5°		
					112.5° - 97.5°	112.5° - 97.5°	112.5° - 97.5°		

Angles of the outer hemisphere (Full Size) with related Bin-numbers

	1.ring	2.ring	3.ring	4.ring	5.ring	6.ring	7.ring	8.ring	9.ring
"Θ" Theta	0° - 5°	5° - 15°	15° - 25°	25° - 35°	35° - 45°	45° - 55°	55° - 65°	65° - 75°	75° - 90°
"Φ" Phi	0° - 360°	247.5° - 292.5°	258.75° - 281.25°	261° - 279°	262.5° - 277.5°	262.5° - 277.5°	262.5° - 277.5°	258.75° - 281.25°	255° - 285°
		202.5° - 247.5°	236.25° - 258.75°	243° - 261°	247.5° - 262.5°	247.5° - 262.5°	247.5° - 262.5°	236.25° - 258.75°	225° - 255°
		157.5° - 202.5°	213.75° - 236.25°	225° - 243°	232.5° - 247.5°	232.5° - 247.5°	232.5° - 247.5°	213.75° - 236.25°	195° - 225°
		112.5° - 157.5°	191.25° - 213.75°	207° - 225°	217.5° - 232.5°	217.5° - 232.5°	217.5° - 232.5°	191.25° - 213.75°	165° - 195°
		67.5° - 112.5°	168.75° - 191.25°	189° - 207°	202.5° - 217.5°	202.5° - 217.5°	202.5° - 217.5°	168.75° - 191.25°	135° - 165°
		22.5° - 67.5°	146.25° - 168.75°	171° - 189°	187.5° - 202.5°	187.5° - 202.5°	187.5° - 202.5°	146.25° - 168.75°	105° - 135°
		337.5° - 292.5°	123.75° - 146.25°	153° - 171°	172.5° - 187.5°	172.5° - 187.5°	172.5° - 187.5°	123.75° - 146.25°	75° - 105°
		292.5° - 337.5°	101.25° - 123.75°	135° - 153°	157.5° - 172.5°	157.5° - 172.5°	157.5° - 172.5°	101.25° - 123.75°	45° - 75°
			78.75° - 101.25°	117° - 135°	142.5° - 157.5°	142.5° - 157.5°	142.5° - 157.5°	78.75° - 101.25°	15° - 45°
			56.25° - 78.75°	99° - 117°	127.5° - 142.5°	127.5° - 142.5°	127.5° - 142.5°	56.25° - 78.75°	345° - 15°
			33.75° - 56.25°	81° - 99°	112.5° - 127.5°	112.5° - 127.5°	112.5° - 127.5°	33.75° - 56.25°	315° - 345°
			11.25° - 33.75°	63° - 81°	97.5° - 112.5°	97.5° - 112.5°	97.5° - 112.5°	11.25° - 33.75°	285° - 315°
			348.75° - 326.25°	45° - 27°	82.5° - 67.5°	82.5° - 67.5°	82.5° - 67.5°	348.75° - 326.25°	
			326.25° - 348.75°	27° - 45°	67.5° - 82.5°	67.5° - 82.5°	67.5° - 82.5°	326.25° - 348.75°	
			303.75° - 326.25°	9° - 27°	52.5° - 67.5°	52.5° - 67.5°	52.5° - 67.5°	303.75° - 326.25°	
			281.25° - 303.75°	351° - 9°	37.5° - 52.5°	37.5° - 52.5°	37.5° - 52.5°	281.25° - 303.75°	
			333° - 297°	22.5° - 352.5°	22.5° - 352.5°	22.5° - 352.5°	22.5° - 352.5°		
			351° - 333°	37.5° - 22.5°	37.5° - 22.5°	37.5° - 22.5°	37.5° - 22.5°		
			315° - 351°	7.5° - 37.5°	7.5° - 37.5°	7.5° - 37.5°	7.5° - 37.5°		
			333° - 315°	22.5° - 7.5°	22.5° - 7.5°	22.5° - 7.5°	22.5° - 7.5°		
			297° - 333°	352.5° - 22.5°	352.5° - 22.5°	352.5° - 22.5°	352.5° - 22.5°		
			315° - 297°	7.5° - 352.5°	7.5° - 352.5°	7.5° - 352.5°	7.5° - 352.5°		
			279° - 315°	337.5° - 7.5°	337.5° - 7.5°	337.5° - 7.5°	337.5° - 7.5°		
			297° - 279°	352.5° - 337.5°	352.5° - 337.5°	352.5° - 337.5°	352.5° - 337.5°		
				322.5° - 352.5°	322.5° - 352.5°	322.5° - 352.5°	322.5° - 352.5°		
				337.5° - 322.5°	337.5° - 322.5°	337.5° - 322.5°	337.5° - 322.5°		
				307.5° - 337.5°	307.5° - 337.5°	307.5° - 337.5°	307.5° - 337.5°		
				322.5° - 307.5°	322.5° - 307.5°	322.5° - 307.5°	322.5° - 307.5°		
				292.5° - 322.5°	292.5° - 322.5°	292.5° - 322.5°	292.5° - 322.5°		
				307.5° - 292.5°	307.5° - 292.5°	307.5° - 292.5°	307.5° - 292.5°		
				277.5° - 307.5°	277.5° - 307.5°	277.5° - 307.5°	277.5° - 307.5°		
				292.5° - 277.5°	292.5° - 277.5°	292.5° - 277.5°	292.5° - 277.5°		

Solid angle calculation with a fenestration of 16 polygons

centroid manikin polygon	
O_i	
1.556	
1.014	
0.888	

vertices Fenestration polygon	
O_j	O_l
1.5	0.75
0	0
0	0.75

distance vectors		
ij	ik	il
-0.056	-0.056	-0.806
-1.014	-1.014	-1.014
-0.888	0.612	-0.138

normalized distance vectors		
ijn	ikn	iln
-0.042	-0.047	-0.619
-0.752	-0.855	-0.778
-0.658	0.516	-0.106

cross product	
$ikn \times iln$	
0.492	
-0.324	
-0.492	

solid angle

$\omega_i = \mathbf{0.3950}$

Solid angle calculation with a fenestration of 64 polygons

centroid manikin polygon	
O_i	
1.556	
1.014	
0.888	

vertices Fenestration polygon	
O_j	O_l
1.5	1.3125
0	0
1.5	1.3125

distance vectors		
ij	ik	il
-0.056	-0.056	-0.2435
-1.014	-1.014	-1.014
0.612	0.237	0.4245

normalized distance vectors		
ijn	ikn	iln
-0.047	-0.054	-0.216
-0.855	-0.972	-0.901
0.516	0.227	0.377

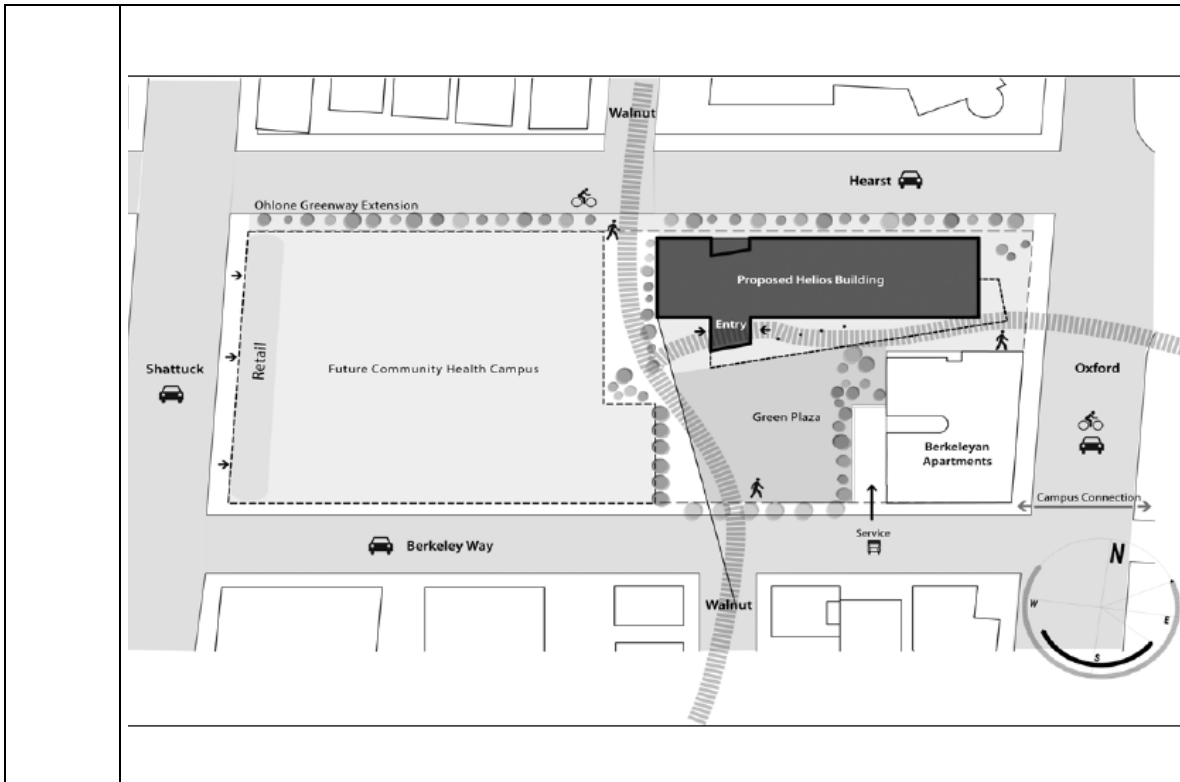
cross product	
$ikn \times iln$	
-0.162	
-0.029	
-0.162	

solid angle

$\omega_i = \mathbf{0.0262}$

Equation after EULER-ERIKSON for solid angle:

$$\tan(\omega/2) = \frac{|\vec{j} \cdot (\vec{k} \times \vec{l})|}{1 + \vec{j} \cdot \vec{k} + \vec{k} \cdot \vec{l} + \vec{l} \cdot \vec{j}}$$



Picture 1 Location of the Helios building at Hearst and Oxford in Berkeley, California.



Picture 2 North facade of the Helios building with location of several laboratories.



Picture 3 East facade of the Helios building with the beginning glazing façade.



Picture 4 The façade consist of a change between transparent and opaque glazing areas.



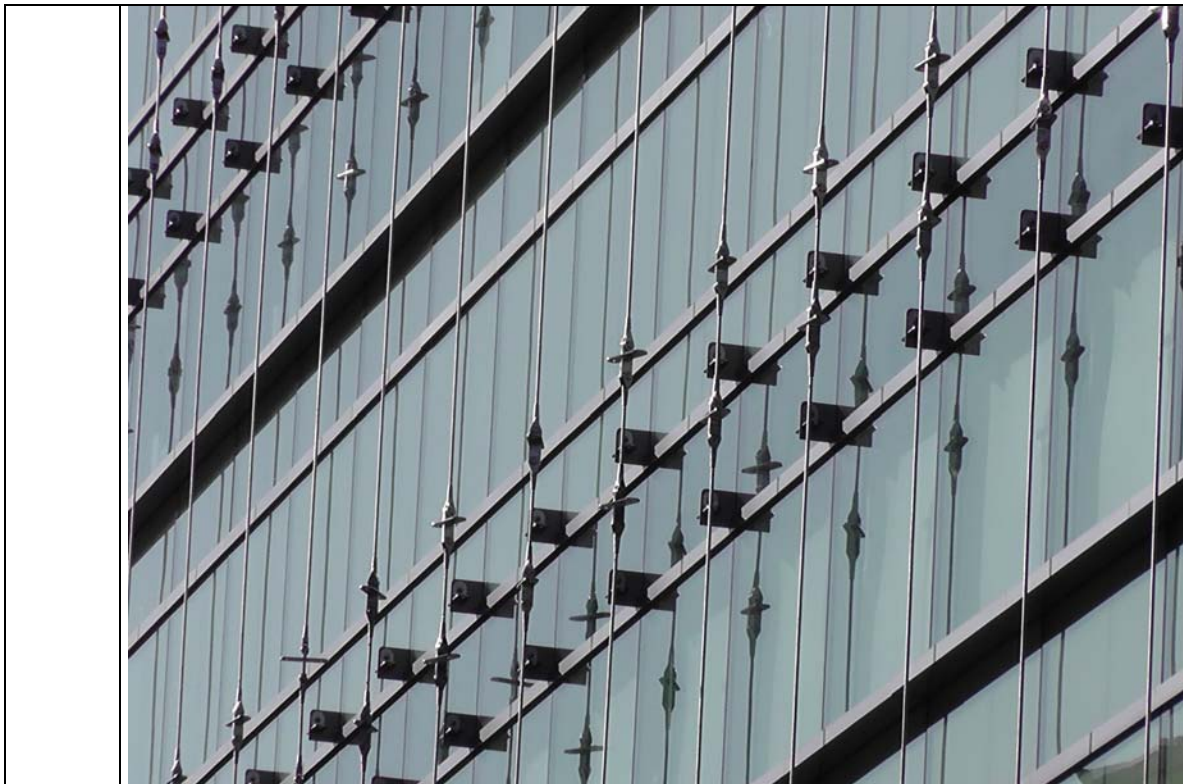
Picture 5
(top)

South facade of the Helios building with location of several offices. Caused by the construction process still without sunshades, but already with a clear division between transparent and opaque glazing areas for every floor.

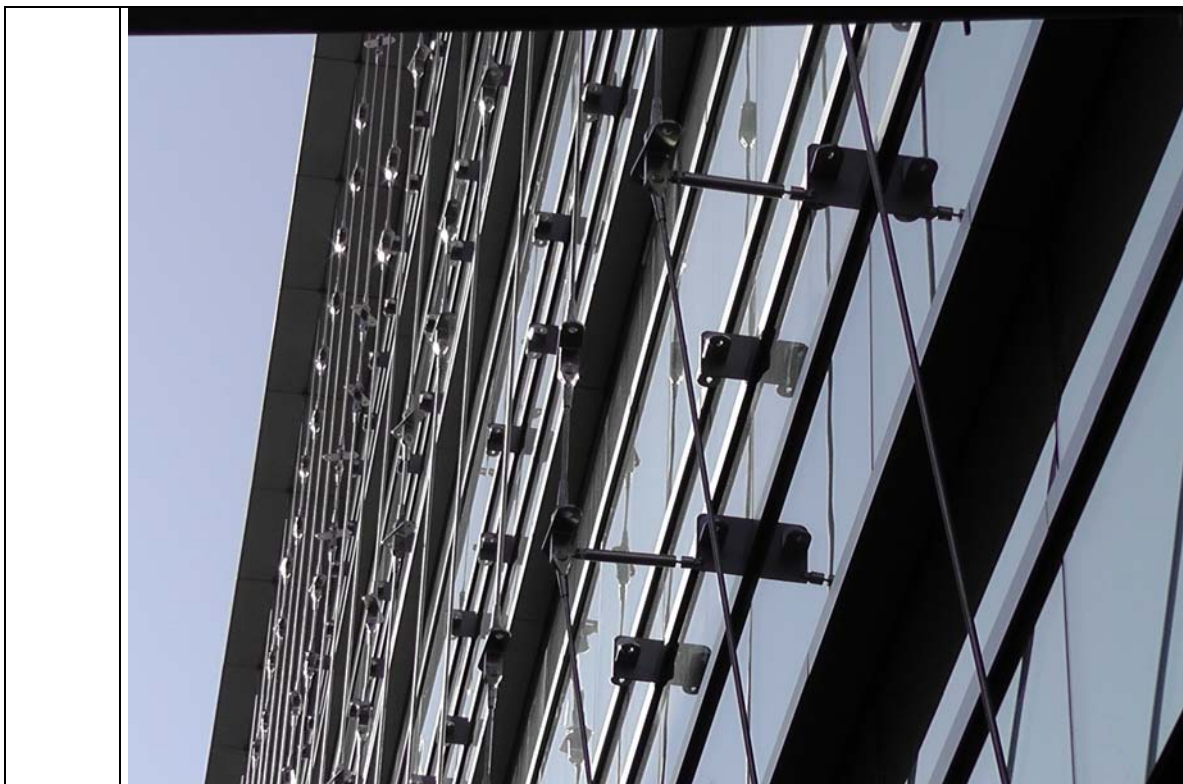
Picture 6
(right)

South façade with already installed cable construction for the following sunshades.





Picture 7 The installed cable construction should hold the sunshades to minimize the heat flow through thermal separation of the shades and the façade.



Picture 8 The cable construction allows the construction of the sunshades with minimal contact area of the shades with the façade.